Additive manufacturing of thermoplastic matrix composites

João Alberto Pereira dos Santos

Masters Dissertation

Supervisor: Prof. Jorge Lino

Advisor: Eng. Isaac Ferreira

U. PORTO
FEUP FACULDADE DE ENGENHARIA
UNIVERSIDADE DO PORTO

Integrated Masters in Mechanical Engineering

September of 2017

To my Famíly,

Resumo

Nesta tese, uma impressora Mark One imprimiu vários tipos de provetes de nylon reforçados com anéis de fibra contínua de Kevlar concentricos. Os tipos eram: nylon puro (com zero reforço) e provetes reforçados com 2, 4 ou 5 anéis concêntricos de Kevlar. Cada tipo de provete tinha diferentes volumes de fibra para estudar, de forma quantitativa, o impacto do reforço de fibra nas propriedades mecânicas do material. Os provetes impressos foram testados experimentalmente (à tracção) e mostraram um grande aumento no módulo de elasticidade e tensão de rotura, com a adição de fibra contínua.

Os provetes impressos reforçados com fibra foram pesados antes da realização de qualquer teste experimental a fim de obter as suas propriedades mecânicas especificas. Os resultados mostraram que, mesmo com falha prematura do provete, estes compósitos apresentam valores de módulo de elasticidade e tensão de rutura especificos semelhantes aos encontrados em alguns metais e ligas metálicas.

Em paralelo, foi desenvolvido um modelo analítico (Volume Average Stiffness model) que prevê as propriedades mecânicas (mais especificamente o módulo de elasticidade) de compósitos impressos em 3D (por FDM). Os resultados da previsão do modelo mostram uma boa concordância com os resultados experimentais. De fato, os resultados do modelo analítico, quando comparados aos resultados dos testes experimentais, apresentaram erros de, no pior dos casos, 4,61%, para a geometria com menos reforço de fibra (2 anéis concêntricos). Para os provetes reforçados com 4 e 5 anéis de fibra, esta diferença foi inferior a 1%.

Além disso, desenvolveu-se uma nova geometria de provete, para ensaios de tração, especifica para este tipo de materiais produzidos por FDM (altamente anisotrópicos), de forma a evitar concentração de tensões que causam rotura na região em que há alteração de secção transversal da amostra, comprometendo os resultados de tensão de rotura.

Additive manufacturing of thermoplastic matrix composites

Abstract

In this dissertation, a Mark One Printer was used to print various types of Nylon specimens reinforced with concentrically deposited "Kevlar" continuous fiber rings. The types were: pure nylon (with zero reinforcement) and fiber reinforced test pieces with 2, 4 or 5 concentric rings of reinforcement. Each type of specimen had different volumes of fiber to study its impact on the mechanical properties of the material. The printed test specimens were tested experimentally and showed an increase in the elastic modulus and ultimate tensile strength with the addition of fiber reinforcement.

The fiber reinforced printed specimens were weighted before any experimental tests took place in order to obtain their specific mechanical properties (specific elastic modulus and specific tensile strength). The results showed that, even with premature failure, these composites exhibited similar values of specific elastic modulus and specific tensile strength of those found in some metals and metal alloys.

In parallel, an analytical model (Volume Average Stiffness model) was developed that predicts mechanical properties of 3D printed (by FDM) composites (more specifically the modulus of elasticity). The model prediction results show a good concordance with the experimental results. In fact, the analytical model results, when compared to the results of the experimental tests had errors of, in the worst case, 4.61%, for the geometry with less fiber reinforcement (2 concentric rings). For the reinforced specimens with 4 and 5 fiber rings, this difference was less than 1%.

In addition, a new geometry of this type of composite test specimen for tensile tests has been developed in order to avoid failure in the shoulder region of the specimen, a common occurrence that causes premature failure of high anisotropic materials like the 3D-printed composite specimens in this work.

Acknowledgments

First of all, I would like to thank the real people responsible for this moment, my family, in particular, my parents. Thank you for the sacrifices you made, and for making me appreciate my origins. For always being able to advise me in the best way. And for the confidence you have in the decisions I make. For everything. All that I do and am is thanks to you. One day I hope to have the opportunity to give back.

Afterwards, I would like to thank Engineer Isaac Ferreira for his availability and total professionalism. For fostering my interest in this fascinating area that is Additive Manufacturing. For helping me decide which direction to take.

To Professor Jorge Lino, for his great patience, flexibility, guidance and professionalism.

To all the staff of INEGI with whom I came across during this project, for the good spirit they showed and for their constant help.

I would like to express my gratitude, also, to all my teachers.

And because not everything you learn, is in college, I would like to thank all my friends, both from continental Portugal, and from the islands, for sharing this adventure with me and for giving me so many unforgettable moments.

A special thanks to my friends of always and to the ones made at the university residence Jayme Rios de Souza that made me feel at home in a place completely unknown to me. They are also responsible for completing this phase, due to the great concern, expressed daily, by the state of this dissertation.

Author gratefully acknowledge the funding of Project NORTE-01-0145-FEDER-000022 - SciTech - Science and Technology for Competitive and Sustainable Industries, cofinanced by Programa Operacional Regional do Norte (NORTE2020), through Fundo Europeu de Desenvolvimento Regional (FEDER).

NORTE2020
PROGRAMA OPERACIONAL REGIONAL DO NORTE

PORTUGAL 2020

UNIÃO EUROPEIA
Fundo Europeu
de Desenvolvimento Regional

Index

Nomenclature

0R	Nylon only configuration
2R	2 ringed reinforcement configuration of specimen
4R	4 ringed reinforcement configuration of specimen
5R	5 ringed reinforcement configuration of specimen
3D	Three dimensional
ABS	Acrylonitrile Butadiene Styrene
AM	Additive manufacturing
ASTM	American Society for Testing and Materials
CAD	Computer Aided Design
CF	Carbon fiber
DEGI	Department of Engineering and Industrial Management
DEMec	Department of Mechanical Engineering
E	Elastic modulus
FDM	Fused deposition modeling
FEUP	Faculty of Engineering of the University of Porto
FLD	Fiber length distribution
FOD	Fiber orientation distribution
G	Shear modulus
INEGI	Institute of Science and Innovation in Mechanical Engineering and Industrial Engineering
LFRT	Long Fiber Reinforced Thermoplastic
LN	Length of the narrow section of specimen
MFP	MarkForged Print (type of file)
$N_{ceiling}$	Number of ceiling layers
$N_{concentric}$	Number of fiber concentric rings
N_{fiber}	Number of reinforced layers
N_{floor}	Number of floor layers
N_{infill}	Number of infill layers
N_{solid}	Number of solid layers
OMMT	Organic modified montmorillonite
PLA	Polylactic acid
PP	Polypropylene
PPS	Polyphenylenesulfide
RP	Rapid prototyping
RTM	Resin transfer molding

SEM	Scanning Electron Microscopy
SFRT	Short Fiber Reinforced Thermoplastic
SRIM	Structural reaction injection molding
STL	Stereolithography (type of file)
T	Thickness of the narrow section of specimen
T_{layer}	Layer thickness
TLCP	Thermotropic liquid crystalline polymer
TPC	Thermoplastic composite
UV	Ultra violet
VAS	Volume Average Stiffness
W	Width of the narrow section of specimen
W_{fiber}	Width of each reinforcement fiber
W_{shell}	Width of each shell
υ	Poisson’s ratio

I. Figure Index

II. Table Index

1 Introduction

1.1 Introduction and motivation

Laminated parts made with the FDM (Fused Deposition Modeling) process are becoming increasingly popular in the last years. This growth in popularity can be explained due to their ability to assume any kind of geometry. However, these parts normally made of thermoplastic polymers lack adequate values of stiffness and strength for usage in high performance applications.

In fact, in the case of an FDM printed part, the composition of each layer should be considered in a different way than other layered composites. In typical composites, parts are formed by two constituents: matrix and reinforcement. The matrix is a topologically connected constituent, while inclusions are distributed in it. However, frequently in FDM technology, the thin thermoplastic rasters are analyzed as “reinforcement” of a “matrix” of void space, with the voids being the empty spaces between rasters and also between layers [1]. The existence of void space is the main responsible for degrading the mechanical properties of FDM printed parts.

This limitation confines the applicability of these products to relatively low-loaded products and to those whose failures do not lead to severe consequences. A way of increasing the mechanical properties of these parts, and consequently, their span of applicability to high performance grounds, is to use the capability of the FDM process to develop new composite parts, through the reinforcement of thermoplastic polymer matrix with continuous fibers. Transforming the thermoplastic parts with relatively low mechanical properties, in high strength and durability lightweight composite structures that can meet special requirements, like the ones existing in aeronautics application domain, is a new development direction with strong demand.

However, in order to fabricate composite parts by FDM with specific load bearing capabilities, it is essential to have models for the FDM material mechanical properties (for example stiffness and strength) as a function of microstructural parameters. In fact, prediction of their behavior to different load cases is one of the main goals in the field of micromechanics science. It must be estimated taking into account each component’s relevant properties and also the phase arrangement, i.e., the geometry and the way in which each of the constituents of the composite part are interrelated.

In pursuing a general approach to model mechanical behaviors of FDM parts, this work aims at the predictive power of models for applications in designing parts for specific mechanical requirements. It is also important to determine the effective stiffness, which is an average measure of the stiffness of the composite material, taking into account the properties of all phases of the heterogeneous media and their interaction. The effective stiffness properties can be used in the analysis of a loaded body composed of the composite material. This effective stiffness is predicted in this work for printed composites with different volumes of fiber reinforcement, using the Volume Average Stiffness model. Experimental results are carried to validate the predictions of the model.

1.2 Presentation of the Host Institution

This dissertation was held at the Institute of Science and Innovation in Mechanical Engineering and Industrial Engineering (INEGI), in partnership with the Department of Mechanical Engineering (DEMec) of the Faculty of Engineering of the University of Porto (FEUP).

INEGI is an Institute of new technologies, located in the University - Industry interface and directed to the realization of research activity and technology - based innovation and transfer of technology oriented to the industrial fabric. It was born in 1986 in what are today the Department of Mechanical Engineering (DEMec) and Department of Engineering and Industrial Management (DEGI) of the Faculty of Engineering of the University of Porto (FEUP).

1.3 Objectives of this work

The aim of this dissertation is founded on the work developed by Melenka et. al [2]. In fact, the aim of this dissertation is to replicate the experiments and predictions made in [2], to validate the developed model (Volume Average Stiffness model) so in the future, specimens with different geometries or different manufacturing parameters can be used to test its fidelity and flexibility as an effective tool of predicting mechanical properties (in this dissertation, elastic modulus is highlighted) of printed parts.

A secondary objective of this dissertation is the development of a new geometry to test additive manufactured fiber reinforced thermoplastics (tensile test), as this is an area in need of development.

1.4 Methodology carried in the dissertation

The methodology followed during the accomplishment of this dissertation consisted of a set of tasks that can be summarized as follows:

- **Literature review** – In this initial phase a review of the state of the art regarding additive manufacturing (using Fused Deposition Modeling technique) of fiber reinforced composites with thermoplastic matrix was conducted. The potential and the need for development of predictive models was also identified and researched

- **Planning and design of test specimens** – In this part, the specimens were designed with Computer Aided Design (CAD) software and printed according to the work of [2].

- **Dimensional control and weighting of test specimens** – After obtaining the specimens, a dimensional control was necessary in order to check the differences between the nominal and measured dimensions and to calculate the stress present in the narrow cross section of all printed specimens. Additionally, the specimens were weighed to evaluate their specific properties, namely, the specific elastic modulus and the specific tensile strength.

- **Realization of mechanical (tensile) tests and processing of test data** – Tensile tests were carried to all the types of printed specimens. Their mechanical properties (elastic modulus, ultimate tensile strength and elongation at break) were obtained using the procedure described in ASTM D638-14. It is important to notice that all fiber reinforced specimens failed in the shoulder region.

- **Development of the Volume Average Stiffness model –** Using the steps described in [2], a model was developed in Excel to predict, essentially, the elastic modulus of printed parts in a fast and easy way, having in consideration the printing parameters and the mechanical properties of each constituent of the 3D-printed fiber reinforced specimen. Once the large differences of analytically and experimentally determined values for the elastic modulus were observed, an alteration of the fiber width parameter of the model was carried. This alteration led to more accurate predictions.

- **Development of new specimen geometry for tensile testing of 3D-printed composites** – A new geometry was created following some guidelines that reduce/avoid stress concentration in the specimens. This geometry aims to avoid premature failure experienced in the tensile tests of the 3D-printed fiber reinforced specimens.

1.5 Structure of the dissertation

The structure of this dissertation is divided in 6 chapters according to the following structure:

- **Chapter 1 (Introduction)** - a brief description of the framework, presentation of the host institution, objectives and methodology followed during this project is carried out;

- **Chapter 2 (Layered Manufacturing of Fiber Reinforced Thermoplastics) –** In this chapter, current conventional and additive methods for the manufacture of fiber reinforced composites are presented. In the additive manufacturing methods, FDM is highlighted and some improvements needed to take the technology to another level (in terms of mechanical resistance) are described, including the addition of fiber reinforcement, and in particular, continuous fiber reinforcement. Mark One is presented and a brief summary of carried experiments with parts printed with this machine can be found. Finally, the work and results of Melenka et al [2] (in which the Volume Average Stiffness method is applied) are introduced.

- **Chapter 3 (Materials and Methods)** – In this section, Mark One Printer particularities and limitations are detailed to better understand the work done. The procedure for obtaining the test specimens, their manufacture parameters and the mechanical properties of the constituents of the 3D-printed fiber reinforced specimens are explained in detail. The Volume Average Stiffness model is also introduced and described.

- **Chapter 4 (Results) –** Both the experimental results (stress-strain graphs of the performed tensile test) and the analytical model results are exposed. The experimental tests allowed to see that the 3D-printed fiber reinforced specimens failed at the shoulder region. In the analytical model part, great detail is used for describing the procedure to obtain the Volume Average Stiffness results.

- **Chapter 5 (Discussion and analysis) –** In this section, possible explanations for the premature failure of specimens in the shoulder region are discussed and a specimen geometry design is proposed to solve the problems experienced in the experimental tests. Also a quantitative comparison between experimentally determined and predicted values of the elastic modulus of the printed parts is done.

- **Chapter 6 (Concluding Remarks) –** In this final chapter, the conclusions of this work are presented as well as suggestions for future work.

2 Layered Manufacturing of Fiber Reinforced Thermoplastics

In general, composites can be defined as a selected combination of dissimilar materials with a specific internal structure and external shape. The unique combination of two material components leads to singular mechanical performance characteristics, impossible to achieve with any of the components alone. The properties of any composite depend mainly on the properties of its constituents, their internal structure and their volume percentages. In Figure 1, the different types of matrixes and reinforcements of a composite material are shown.

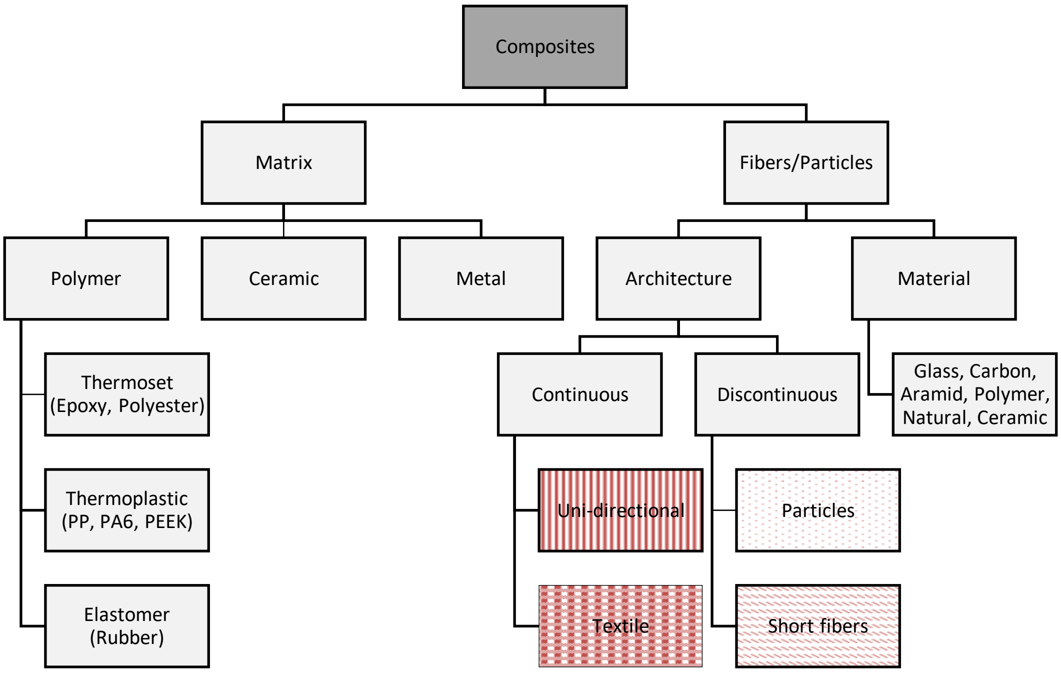

Figure 1 - Composition of composite materials [3].

Generally, the strength and stiffness of a composite are very dependent of the reinforcing material. However, the mechanical behavior of the composite, is not exclusively ruled by the reinforcement alone, but by a partnership between the reinforcement and the matrix [4]. There must exist a cooperation between the reinforcement and the matrix for a composite to be an effective load bearing system. This cooperation between the fibers and the matrix can’t exist without the interface. The interface acts as a binder and transfers load from the matrix to the reinforcing fibers, and vice-versa [5]. Its characteristics determine some of the properties of a composite. Namely, resistance to creep, fatigue and environmental degradation are all properties influenced by a good interface. For example, considering a composite made with the same constituent materials, a weak interface leads to low stiffness and strength, but it improves the resistance to fracture. On the other hand, a strong interface creates composite materials with high stiffness and strength, but in most cases, it causes a brittle behavior [6].

Strong interfacial bonding can be achieved in many ways. One of them is good impregnation of the fibers/particles by the matrix as well as the development of a chemical bond between the reinforcement surface and the matrix [5]. The matrix performs a number of vital functions. Specifically, stabilization of the fiber in compression (by providing lateral support), minimization of impact damage by demonstrating plastic deformation and provision of out-of-plane properties to the laminate are some of them [6]. Usually, polymeric matrices are ductile materials, and have a significant contribution on the effective toughness of a composite, making them ideal matrixes [4], [5]. However, the ductile nature of these materials are not the only reasons for their wide use as matrixes. For example, the melting point of most polymers is lower than the degradation temperature of most fibers, making their fabrication easier.

Inside the polymeric matrix composites, thermoplastic composites (TPCs) offer some substantial advantages over thermoset ones. Welding and recycling are only some of the attractive opportunities they offer [7]. Moreover, due to the higher toughness of the matrix, they provide a higher impact resistance. Additionally, the manufacturing cycle times for these materials are considerably shorter than for their thermoset counterparts, since melting, shaping and consolidation by cooling of the matrix, generally take less time than the needed curing step of thermoset materials.

Fiber reinforcement in thermoplastics has three basic forms: short fiber reinforcement, long fiber reinforcement and continuous fiber reinforcement. The criteria used for differentiating them is based on the length of the reinforcement fibers. Long fiber reinforced thermoplastics (LFRT) possess starting fiber lengths of 1– 25mm in contrast to short fiber reinforced thermoplastics (SFRT) compounds that own 0.5mm fiber length or less. Continuous fiber reinforcement is frequently used in high performance composites and its length can extend to the full size of the component itself. It has been demonstrated that mechanical properties such as strength, modulus and toughness generally increase with increasing fiber length [8], [9] but in some cases the use of long fibers has proven to increase the elastic modulus and the tensile strength of the material as close as to 90% of that obtained when using continuous fiber [10]. Some studies on failure mechanisms [11], [12] showed that under tensile loading, the cracks start at the fiber ends and proliferate along the fiber–matrix interface or through the matrix until failure. Fiber ends have been revealed as sources of stress concentration in the neighboring matrix. The effects of these stress concentrations can be relieved only by either matrix flow, interface debonding or matrix fracture [13]. Therefore, most high performance composites are usually reinforced with much longer fibers, that are normally bundled into continuous yarns.

If a composite is to take full advantage from the reinforcing material, the reinforcement has to be able to receive loads that stress it to its breaking point. Otherwise (and if the interfacial bonding is weak) the composite will fail at an inferior load than what the fibers could theoretically sustain. When this happens, the fibers basically pull out of the matrix, without breaking, as the composite collapses [3].

Since load is transferred from the matrix to the reinforcing fibers by shear forces acting on their surface, it is desirable that their surface area outsize their cross-sectional area. That is to say, an effective reinforcing element is much longer in one dimension than in the other two. The critical aspect ratio, or the ratio of length to diameter at which the fiber is capable of sustaining enough stress to break it, is generally near 100:1. The specific number varies from case to case and depends on factors such as the strength of the fiber, the characteristics of the matrix and the extent of connection between them [14]. Long fibers therefore reinforce a composite more efficiently than short fibers or particles do, since they have a larger aspect ratio.

There is a second reason continuous fibers have become the prevailing form of reinforcement in high-performance composites: their orientation can be controlled precisely. In other words, the internal structure of the composite can be designed to anticipate the stresses it will face in use, making it more efficient.

The internal geometry of conventional high-performance composites resembles that of plywood. They are built up of thin layers, each layer reinforced by continuous fibers running in a single defined direction (Figure 2). Construction of such laminated structures is carried through pre-impregnation of tapes or sheets, followed by their assembly by hand lay-up for instance. This way, successive layers can be oriented in different directions to provide the final product with stiffness and strength along several axes.

However, such composites are crippled by the fact that neither do the reinforcing fibers run from layer to layer nor transversely within each layer. Therefore, and in severe circumstances, delamination of the composite isn’t uncommon. Additionally, separation of parallel fibers in the same individual plies is a problematic occurrence. Moreover, the unidirectional nature of these laminates lead to low impact resistance. In a thermoplastic matrix composite the matrix alone may be quite ductile and tough but with the presence of a strongly bonded, dense array of fibers, an embrittlement of the composite occurs by limiting its ability to dissipate the energy of an impact through plastic deformation of the matrix. To dissipate this energy, cracks are formed. These cracks can easily propagate and proliferate between the layers of fibers and consequently, an impact that would only have dented a polymer might produce severe damage in a composite in which the same polymer functions as the matrix [3].

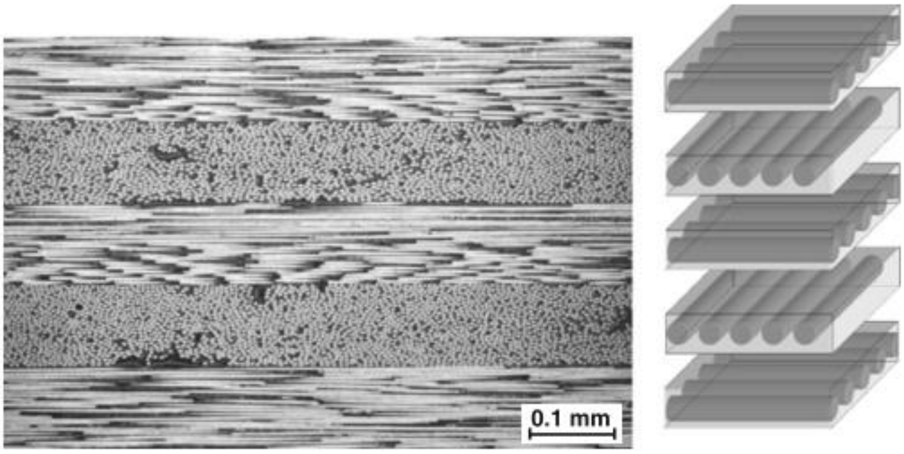

Figure 2 – Multi-directional composite laminate [0/90/0/90/0] [3].

At present, synthetic fibers, such as glass, carbon and aramid, reinforce the majority of polymer composite materials produced [5]. However, due to growing environmental awareness and new emerging regulations, industries are being forced to seek more ecologically friendly solutions for their products. Thus, natural fibers are gaining a more important role in the industry. In addition, natural fibers have many advantages compared to synthetic fibers like lower weight and recyclability. They also have relatively high strength and stiffness and cause no skin irritations [15]. On the other hand, some drawbacks exist as high moisture uptake and quality variations as well as low thermal stability.

Many investigations have been made on the potential of the natural fibers as reinforcements for composites and in several cases the results have shown that the natural fiber composites own good stiffness but the composites do not reach the same level of strength as glass fiber composites [15]. The success of natural fiber reinforced polymeric composites will be dependent upon appropriate processing techniques, modification of fibers to improve the adhesion between fiber and the biopolymer, matrix modification and after treatment to improve performance as well as long-term durability and fire retardancy [16].

In structural composite applications, textiles are commonly applied as reinforcement because of the high fiber volume fractions that can be obtained and because of the possibility to tailor the load bearing capacity through the fiber lay-up [7]. By changing the orientation or placement of the fibers, the material can be designed to exhibit properties that are isotropic or highly anisotropic, depending on the desired end result [17]. The complexity inherent in conceiving components and their materials at the same time suggests engineering design will grow increasingly dependent on computers and multidisciplinary teams. Such an approach will harness the full potential of composites for the technologies of the future [3].

A major drawback of this customization is the economic costs that may be associated with this processing method. While customizing individual parts may be appropriate when working with low production level parts, when the idea is extrapolated to higher production parts, the customizing process becomes highly cost prohibitive. For higher production parts the use of thermoplastic sheets that have a pre-existing fiber orientation is a cost effective choice [17]. There has been extensive work throughout industry with forming and shaping oriented glass and carbon fiber reinforced thermoplastics. Common difficulties experienced show that the forming of straight, continuous fiber or woven fiber composite sheets typically results in wrinkling of the fibers and distortions. Randomly oriented fibers have provided good formability, but without the advantages of the highly directional properties often desired in composite parts [17].

Composite materials, in most cases fiber reinforced polymers, are used in many applications in which light weight and high specific modulus and strength are critical issues. The majority of components made of polymer composites go into the field of transportation (including aerospace, automotive, railway, marine), followed by applications in civil engineering (construction), sporting goods, electrical engineering, and other industrial sectors. For instance, the market share for thermoplastic composites in automotive applications has been having a respectable growth in the last years. Economical production technologies, low material cost and recyclability have contributed to this development.

Typical applications are presented in Figure 3 below, in which high performance applications for advanced long fiber reinforced thermoplastics are marked with underlined letters. Usually, cost-effective material compositions, in which polypropylene is used as matrix material and long glass fibers as reinforcement are used to meet the manufacturers specifications. There are current or potential applications for short carbon fiber/polypropylene composites in body structures for ‘passenger cars’ (e.g., car bonnet/hood [18]), fuel cells, fuel tanks and several other niche uses. Combination of characteristics such as low density, corrosion resistance, low to moderate cost, thermal stability and easy processability, make them attractive for many applications in automotive industry.

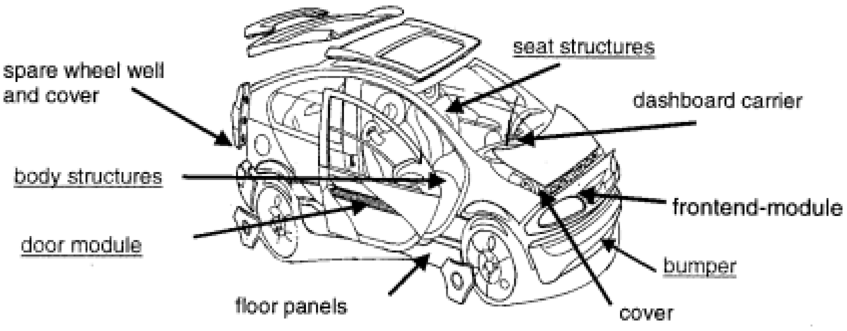

Figure 3 - Applications of long fiber reinforced thermoplastics in the automotive industry [28].

It is estimated that 75% of fuel consumption directly relates to vehicle weight [19]. Lightweight composite materials, also commonly referred to as fiber reinforced plastics (FRP), provide opportunities for reducing vehicle weight by increasing fuel efficiency and reducing emission of harmful pollutants. The effect of making automobiles lighter is captivating. With everything else remaining the same, and considering mass compounding, 6–8% increase in fuel economy can be realized for every 10% reduction in weight [20]. This is much easier to achieve than to offset the increased weight and cost per unit of power of alternative power trains, such as hybrids and/or fuel cells, with respect to conventional power trains. By reducing weight, several advantages can be gained:

- Increased performance;
- Increased “customer value” while staying within certain limits;
- Decreased threat from high prices of fuel;
- Decreased dependency on hybrids and hydrogen- fueled vehicles.

With 75% of vehicle gas (energy) consumption directly related to factors associated with vehicle weight, the potential benefits of weight reduction enable smaller power plant (engine, turbine, fuel cells, etc.) and lighter energy storage (battery, flywheel, etc.) systems. With continued advances in performance, reduced cost, increased safety and weight savings offered by composite materials, their use in the automotive and transportation industry is projected to grow in the coming years [20]–[22].

The overall advantages of composites compared to steels for automotive and transportation in general are:

- Weight reduction of 20–40%;
- 40%–60% reduced tooling cost [3];
- Reduced assembly cost and time in part consolidation;
- Resistance to corrosion, scratches, dents and higher damping;
- Materials and process innovations capable of adding value while providing cost savings;
- Higher specific energy absorption, leading to more secure structures.

The aircraft construction sector has also been experiencing an increase in the use of fiber reinforced thermoplastic composites and this growth is predicted to continue in the future. Weight savings of about 40% can be achieved by using composites instead of light metal alloys in secondary structures of aircrafts. While for primary structures, like wings and fuselages, 20% is a more honest assessment [6].

For higher strength and stiffness applications, carbon fibers, which are expected to replace the glass fibers in long fiber reinforced thermoplastics, are the most preferred reinforcement material. A fact that supports this, is the innovative carbon fiber reinforced composite fuselage that has been widely applied in Airbus A350 aircraft. In fact, about 53% of the constituents of the A350 airframe are made from composites [23], [24].

To have a better idea of the values of the mechanical performance of composites, a list of mechanical properties for some materials is shown below, in Table 1. Here, not only the properties of the final composite are shown, but also the properties of the constituents alone.

To meet the high demand of these materials, it becomes essential to accomplish lower production costs and reduction of cycle times. This can be achieved by the improvement of some production processes currently available and with the creation of innovative new ones. In the next chapter, both conventional and additive manufacturing processes will be introduced and explored.

Table 1 – Comparison of the mechanical properties of some materials.

Material	Density ρ [kg/m^3]	Tensile Modulus E [GPa]	Specific Tensile Modulus [MN.m/kg]	Ultimate Tensile Strength [GPa]	Failure strain ε [%]
Kevlar KM 2 [25]	1400	84.62	60.4	3.88	4.52
Carbon fiber T1000GB [26]	2000	291	145.5	5.69	1
E-Glass	2600	73	28.1	1,9-2,6	3,2
Flax [27]	1500	60-80	40-53	0.8-1.5	1-2
Polypropylene	903	1.30	1.4	0.032	>50
8% volume Glass Fiber + Polypropylene SFRT [13]	-	5.6	-	0.048	1.9
8% volume Carbon Fiber + Polypropylene SFRT [13]	-	10.7	-	0.057	0.8
E-glass/PP LFRT (25.4mm long 40%wt) [28]	1210	7.90	6.5	0.100	2
Kevlar® CFF (Continuous Filament Fabrication) [29]	1250	27	21.6	0.610	5.5
Carbon Fiber CFF (Continuous Filament Fabrication) [29]	1400	54	38.6	0.700	1.5
Fiberglass CFF (Continuous Filament Fabrication) [29]	1600	21	13.1	0.590	5.5
Nylon FFF (Fused Filament Fabrication) [29]	1100	0.94	0.85	0.054	>50

2.1 Manufacturing Techniques: Conventional and Additive

In this section, the most currently used manufacturing processes for fiber reinforced thermoplastic composites, conventional and additive, are presented. The variety of composite manufacturing processes reflects the variety and complexity of these materials. The composite field is continuously changing - new combinations of materials are frequently created whilst new variations and modifications to existing manufacturing methods are introduced.

When it comes to fabricating advanced composite structures, there is an array of fabrication processes available. However, when part complexity increases, performance is demanding and higher volume production rates are required, the field begins to narrow.

2.1.1 Conventional Techniques

One such method that meets the criteria mentioned above, is compression molding with long chopped fiber thermoplastics. Compression molding (Fig. 4) is the process by which a charge of fiber reinforced prepreg bulk molding compound (BMC) is molded under heat and high pressure to form complex shaped parts [30]. Extrusion compounding and injection molding (Fig. 5) processes are frequently employed to make short fiber reinforced polymeric composites. The use of these conventional fabrication techniques to produce large-scale short fiber reinforced composite parts makes the manufacturing of these composites efficient and inexpensive compared with manufacturing of continuous-fiber composites, which are produced by time-consuming processes, rendering them unsuitable for high volume production [9]. In fact, for years, several fabrication methods for continuous fiber reinforced thermoplastic matrix composites have been developed, such as vacuum forming, filament winding, pultrusion, bladder-assisted molding and compression. Nevertheless, the limitations of these processes lie in the high cost of molds, the manufacturing boundedness of the parts with complex constructions and the inability of special fiber alignment, leading to the bottlenecks for the wide applications of continuous fiber reinforced thermoplastic matrix composites in industrial production and people’s daily life [31]–[33]

When compared to long and continuous fiber reinforcements, short fibers composites are the easiest and cheapest to manufacture, but offer the smallest increase in mechanical properties. Injection molding and extrusion compounding, tend to degrade the fibers during processing. It has been shown that fiber breakage in processing of reinforced thermoplastics results from fiber-polymer interaction, fiber-fiber interaction, and fiber contact with surfaces of processing equipment [34]. In addition to this fact, a fiber length distribution (FLD) as well as a fiber orientation distribution (FOD) takes place in parts produced by injection molding. FLD and FOD depend on factors like fiber length, fiber content, mold geometry and processing conditions[35]. On the other hand, they hold a major role in the strength [36], stiffness and fracture toughness [37], [38] of the composite.

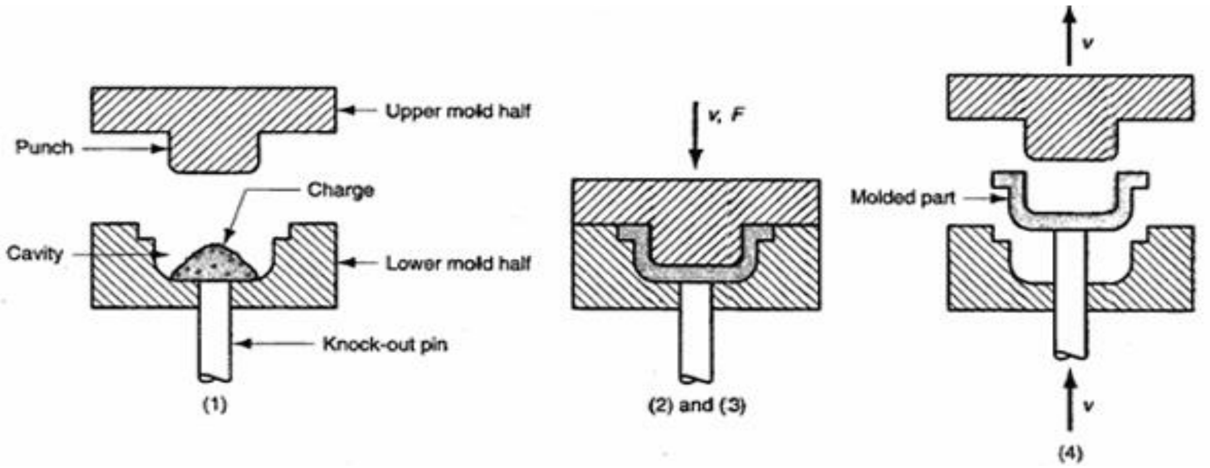

Figure 4 - Compression molding for thermoplastics : in (1), “charge” is loaded; (2) and (3) the “charge” is compressed and heated; (4) there is an opening of the mold halves and the part is removed from the cavity [135].

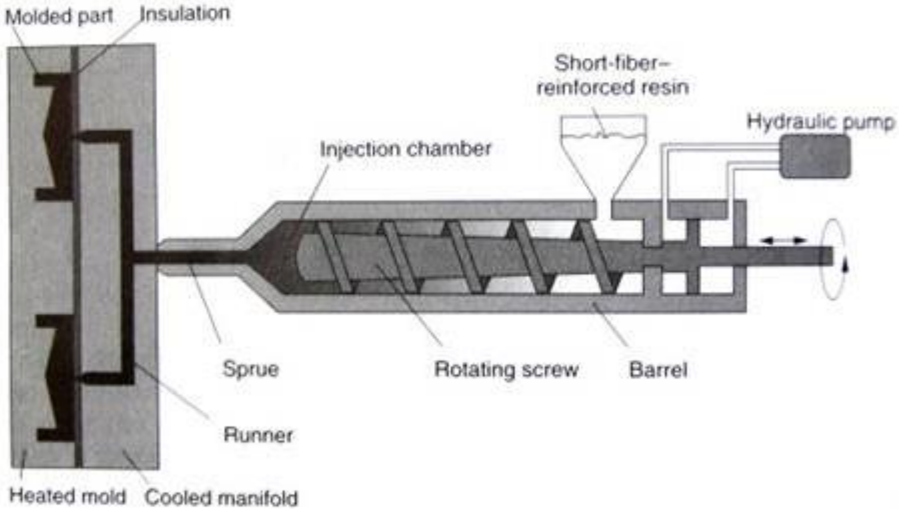

Figure 5 - Injection molding of short fiber reinforced composites. The short fiber reinforced resin/pellets are fed in the injection chamber. After the material is forced to enter and fill the heated mold, the part then solidifies and is ready to be demolded [136].

Traditionally, textile fiber-reinforced thermoplastic matrix composites are melt processed by stacking alternating layers of fiber textiles and polymer sheets in a hot-press. After heating the package above the polymer melting point, the press is closed to obtain the required product shape. In a subsequent cooling step, the product solidification takes place followed by demolding [7].

The main disadvantage of thermoplastic matrix composites is the need for high processing temperatures and pressures, caused by the high melt viscosity of the matrix. In addition, proper impregnation of the fiber at a micro level might prove difficult and often results in products with a locally high void content [7]. The additional remark has to be made that although most plastics can be remolded numerous times without losing properties, some high-performance plastics slightly degrade during processing due to their high melting points: cross-linking occurs for instance in molten PPS (polyphenylenesulfide). Any intermediate processing step that requires melting therefore increases the number of crosslinks, hence resulting in a more brittle matrix [7].

An alternative solution to melt processing is reactive processing of thermoplastic matrix composites: after impregnation of the fibers with a low viscosity mono- or oligomeric precursor, polymerization of the thermoplastic matrix is conducted *in situ* [7]. Polymerization can be initiated by heat or UV radiation and might require the addition of a catalyst system, which can be added to the precursor prior to impregnation. Thanks to the low molecular weight they present, precursors have exceptionally low melt viscosities and proper fiber impregnation without the need for high processing pressures is easily accomplished. Moreover, through reactive processing, textile fiber-reinforced thermoplastic matrix composites can be even manufactured through low-pressure infusion processes such as resin transfer molding (RTM) [39], structural reaction injection molding (SRIM) [39] and vacuum infusion [40]. These are all classic manufacturing processes for manufacturing of thermoset composites. In these processes, a dry fiber pre-form is placed into a closed mold after which the precursor is infused by applying vacuum or pressure, typically less than 10 bar. Following polymerization, the composite product is demolded [7].

With reactive processes, thicker and more integrated products than what is currently achievable with melt processing can be created. Also, considering that polymerization takes place in the fibers neighborhood, a thermoplastic composite with a chemical fiber-to-matrix bond can be manufactured [7].

Trying to develop the through-the-thickness strength properties and impact resistance, the composites industry has moved away from brittle resins and gradually improved. From the development of thermoplastic resins, to Z-fiber reinforcement (carbon, steel or titanium pins driven through the thickness direction to improve the properties in this direction) and development of stitched pre-forms. These days the objective is to achieve lower fabrication prices. In fact, nowadays there is a constant drive to make products with quality in the cheapest way possible. Therefore, the current stage focus is being directed towards cheap processing methods. That is to say non-autoclave processing, non-thermal electron beam curing by radiation and, of course, low cost fabrication are possible [6]. To reduce production costs, it is essential to make an effort to stay away from prepreg material technology, which presently results in an expensive manufacturing solution. Therefore, until the arrival of a new revolutionary manufacturing process, autoclaved continuous fiber composites are expected to overlook everything else for the manufacture of products with the highest levels of mechanical efficiency and requirements [6].

Even though, lately, advanced composites were greatly benefited by conventional textile preforming technologies, some fundamental technological limitations still exist such as, for instance, the lack of precise control of preform structural parameters. Therefore, the micro- and even the macro-structure of a manufactured preform may deviate from those of the intended/optimized model [41]. This is unacceptable, as any preform structural variation will compromise the intended mechanical (and physical) properties of the reinforced composites. Obstructing correct property prediction and design. Furthermore, the cost of conventional fabrication of multi-directional preforms, especially 3D preforms, remains high due to the low level of automation of the process [41].

2.1.2 Additive Manufacturing Techniques

Additive manufacturing (AM) is a result of the evolution of rapid prototyping (RP) processes. Coined in the mid-1980s, rapid prototyping was used to describe a range of technologies that literally made prototypes of products in the early stages of development in a quick and automated manner. However, there is nothing in the term "rapid prototyping" that alludes to the generic "layer-based" approach of its methods. Furthermore, current application of the technology goes far beyond merely prototyping. For these motives a transition from RP to AM took place.

This transition is a culmination of a number of evolutionary developments in materials and processes combined with the reduction in costs of the technology that has served to open it up to a wider user base. However, there has also been a change in the mindset of users that has opened their eyes to new applications or even as a more effective replacement for existing applications.

AM is defined as a process of depositing and/or joining material to make objects from 3D (digital) model data, usually layer upon layer (Fig. 6). AM procedures make it possible to produce relatively complicated parts based on computer 3D geometries. In conventional processes, limited by tooling accessibility to corners and internal surfaces, a complex part is often built by assembling separate simple parts, which often leads to premature structural failure at material joints. In additive manufacturing, however, regardless of their degree of complexity, objects are fabricated following the same procedure: slicing the designed model into a certain number of layers with a predetermined thickness and printing the sliced sections layer upon layer successively from bottom to top. This capability empowers very large geometric design freedom [41] without the need of expensive molds.

Distinguishing features of AM technologies are often presented in the context of a comparison with conventional manufacturing processes. The term “additive manufacturing’’ was ultimately chosen by the ASTM F42 committee [42] as it clearly distinguishes the processes from subtractive manufacturing techniques (Fig. 7) wherein material is removed from a work piece (e.g., cutting, milling, grinding) [43].

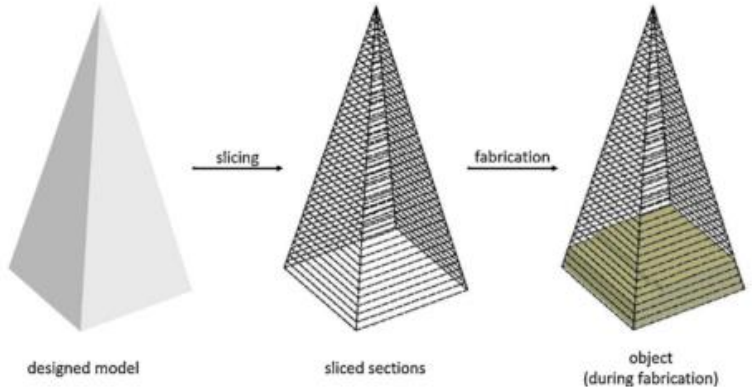

Figure 6 – Schematic of the philosophy of additive manufacturing [41].

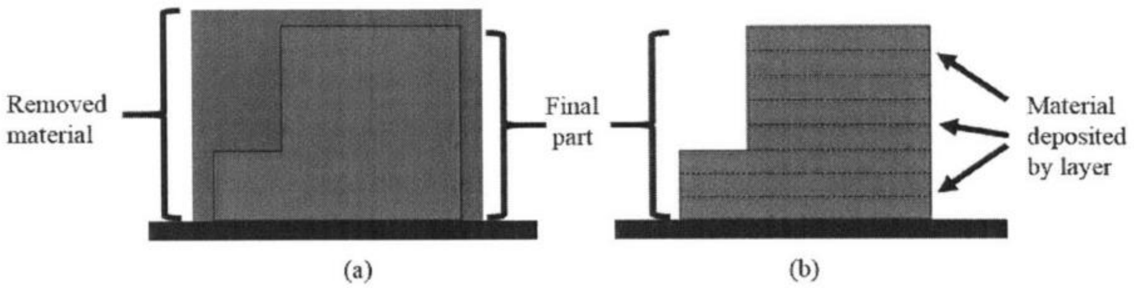

Figure 7 - Subtractive manufacturing (SM) technologies carve a final part from a stock geometry of material (a) while additive manufacturing (AM) technologies deposit material in prescribed locations to build the final part (b) [63].

One of the unique aspects of additive manufacturing is their layer-wise fabrication approach, which enables the creation of almost any complex geometric shape. This is in contrast to subtractive processes, which constrain design freedom due to the need for fixtures, diverse tooling, and the possibility of collisions and difficulty of the cutter in reaching deeper and invisible zones when fabricating complex geometries. Fundamentally, AM technologies offer a designer the ability to selectively place (multi-)material precisely where it is needed to achieve the designed functionality. This capability, coupled with the digital line of production, enables the realization of structures that have been topologically optimized (or feature cellular mesostructure) to reduce material use and decrease mass. In fact, the volume of wasted material when fabricating components via AM is minor with the exception of sheet lamination, which perhaps is the reason why this technology is not receiving as much attention as other AM technologies [44]. In additive manufacturing, the primary responsible for the material wastage, is generally the support structures required to build some parts.

Additive manufacturing processes enable the production of geometric shapes that would otherwise require assembly of multiple parts if produced conventionally. It is possible to use AM to produce “single-part assemblies” products that feature integrated mechanisms. The parts and joints are printed in place and are suspended by support material that must be removed in post-processing. If the support material is water-soluble, it can be washed away by a lye bath with gentle scrubbing. Non-soluble support materials require breaking and peeling away from the model using pliers or conventional cutting tools [45].

Additionally, the ability to produce complex geometric shape parts, comes at no additional cost, as opposed to conventional processes, because there is no need for additional tooling, increased operator expertise, or even fabrication time. For example, in processes such as injection molding, there is a direct relation between geometric complexity and the mold cost. And even tough injection molding’s high time and cost efficiency for mass production (regardless of high start-up cost), additive manufacturing significantly slower processes (better suited for low part quantities), can lower inventory costs and potentially reduce costs associated with supply chain and delivery.

In addition to automation of the manufacturing process and elimination of manufacturing steps (in the case of composites, lay-up, infusion and curing), additive manufacturing facilitates the introduction of functional features [46]–[48], which are generally accompanied by structural complexity [49]. By changing material composition and location within a part at the processing stage [50], multi-material additive manufacturing makes it possible to create the features of multi-functionality and gradient functionality [41].

Another advantage of AM is the potential use of local resources as printer material. Researchers have demonstrated the feasibility of 3D printing habitat parts from simulated lunar soil with a laser 3D printer [51] and the European Space Agency (ESA) is investigating the possibility of 3D printing a Moon base with lunar soil [52]. Perhaps astronauts on a future space outpost will 3D print habitat structures from asteroid material and lunar and Martian soil.

Additive manufacturing (AM) is poised to bring about a revolution in the way products are designed, manufactured, and distributed to end users. This technology has gained significant academic as well as industry interest due to its ability to create complex geometries with customizable material properties. AM is now used in many diverse fields, including the aerospace industry, architecture, nanosystems, fashion, and biomedical research. Nowadays, design templates can be downloaded from the Internet and objects printed at home, whereas medical researchers are using additive manufacturing to create functional organs or bones [53]–[58]. With further development of AM technology, its application is expected to be even more extensive. The market has grown in the past years and the worldwide sales of additive manufacturing is expected to reach $12.5 billion in 2018 [59].

There is a wide array of different AM technologies that can make a part layer-by-layer. Distinguishing between different AM processes is not easy mainly because of the fact that many companies create unique process names in order to differentiate themselves from competitors. There have been many attempts to establish a categorization of AM processes throughout the years. In 1991, Kruth [60] classified various additive manufacturing processes from three perspectives: liquid-based, powder-based and solid-based systems according to different material manufacture. Since then, some classifications [61] have been created until most recently, ASTM International Committee F42 on AM has categorized the different AM technologies into seven groups differentiated essentially by the means of material deposition including material extrusion, powder bed fusion, binder jetting, material jetting, vat photo-polymerization, directed energy deposition, and sheet lamination [62]. In Table 2 there is an overview of these additive manufacturing technologies.

Each AM technology has its own processing capabilities, advantages and limitations including materials, build volume, processing speed, part quality (mechanical performance, dimensional accuracy and surface finish), and the amount of post-processing required to improve the part quality (i.e., support removal or surface finishing) [63]. The assessment of all these aspects are mandatory in view of a proper choice of manufacturing technology for the desired part. Additional information on AM processes can be found in the literature [45], [64], [65].

It is also vital to remember that due to the rapid proliferation of a wide variety of technologies associated with AM, there is a lack of a comprehensive set of design principles, manufacturing guidelines, and standardizationn of best practices. These challenges are compounded by the fact that advancements in multiple technologies (for example materials processing, topology optimization) generate a “positive feedback loop” effect in advancing AM [45].

Table 2 - Overview of Additive Manufacturing Technologies [45].

Categories	Technologies	Printed Material	Power source	Strengths/Downsides
Material Extrusion	Fused Deposition Modeling	Thermoplastics, Ceramic slurries, Metal pastes	Thermal Energy	• Inexpensive extrusion machine • Multi-material printing • Limited part resolution • Poor surface finish
	Contour Crafting			
Powder Bed Fusion	Selective Laser Sintering (SLS)	Polyamides/Polymer	High-Powered Laser Beam	• High Accuracy and Details • Fully Dense Parts • High Specific Strength & Stiffness • Powder Handling & Recycling • Support and anchor structure • Fully dense parts
	Direct Metal Laser Sintering (DMLS)	Atomized metal powder, Ceramic Powder		
	Selective Laser Melting (SLM)			
	Electron Beam Melting (EBM)		Electron Beam	
Vat Photopolymerization	Stereolithography (SLA)	Photopolymer, Ceramics (alumina, zirconia)	Ultraviolet Laser	• High building speed • Good part resolution • High cost for supplies and materials
Material jetting	Polyjet/Inkjet printing	Photopolymer, Wax	Thermal Energy / Photocuring	• Multi-material printing • High surface finish • Low-strength material
Binder jetting	Indirect Inkjet Printing (Binder 3DP)	Polymer Powder (Plaster, Resin), Ceramic Powder, Metal Powder	Thermal Energy	• Full-color objects printing • Require infiltration during post-processing • Wide material selection • High porosities on finished parts
Sheet lamination	Laminated Object Manufacturing (LOM)	Plastic Film, Metallic Sheet, Ceramic Tape	Laser Beam	• High surface finish • Low material, machine, process cost • Decubing issues
Directed energy deposition	Laser Engineered Net Shaping (LENS), Electronic Beam Welding (EBW)	Molten metal powder	Laser Beam	• Repair of damaged/worn parts • Functionally graded material printing • Require post-processing machine

Currently, AM Technology mainly manufactures parts using a single material, but AM technology can also progress to composite materials. With the improvement of the performance requirements of parts, the parts made by composite material or graded materials become urgently needed. To realize the full potential of additive manufacturing as an effective, versatile fabrication method of multi-directional preforms for composites in load-bearing structural components, imbedding reinforcements such as continuous or short fibers, particles, and nanomaterials into the preform may be necessary. Recently, some promising results in additive manufacturing of composites reinforced by fibrous/high-aspect-ratio fillers have been demonstrated (Table 3).

Table 3 - Summary of additive manufacturing of fibrous/high-aspect-ratio fillers reinforced composites [41].

Process	Specific approach	Filler form	Fiber alignment	Alignment mechanism
Material Extrusion	[66]–[70]	Short fiber	Along printing direction	Shear stress (during preparation of feedstock spool)
	[71]	Continuous filament	Along printing direction	Mechanical pulling and laying
	[72]	Short fiber, whisker	Along printing direction	Shear stress (near nozzle)
Powder bed fusion	[73]	Single layer graphene oxide	Perpendicular to cross-section	Evaporation of dispersing agent
	[74]	Nanofiber	Random orientation	-
Vat photopolymerization	[75]	Micro-particle	Along electric-field direction	Polarization effect
Binder jetting	[76]	Short fiber	Along printing direction	-

In the last few years there has been an explosion of relatively inexpensive AM devices based principally on Fused Deposition Modeling (FDM) technology. Pioneered by Fab@Home [77] developed at Cornell University and the RepRap project [78] developed at the University of Bath, almost anything goes so long as it can be made to flow through a nozzle and harden. The relevant designs are generally available and the process is the easiest to synthesize, since the FDM technology does not require laser in forming process. An advantage of this system is that it may be viewed as a desktop prototyping facility in a design office since the materials it uses are cheap, non-toxic, non-smelly and environmentally safe [79]. The wide range of printable materials, the simplicity of the device structure and relatively low cost (average cost of a FDM 3D printer is between $500−2000 USD) when compared to other AM technologies [58] are the main reasons for the wide application and acceptance of this method. Making, at present, FDM equipment the most-used AM equipment.

In the near future, new and continued incremental advances by major AM machine developers and materials providers. In fact, the markets for AM have grown to a stage now that the technology is getting the attention of major feedstock developers and suppliers. It is anticipated that once these major producers are convinced that the time is right, one would expect to see new materials with improved manufacturability and service properties to enter the market. Increased competition will drive down costs as well which will be welcomed by the service bureaus and parts providers as well as consumers. One would hope that medium cost AM equipment will be developed in the next ten years as the primary patents expire, and that these devices, made available to the public on at least a neighborhood or city-wide basis, would foster increased feedstock demand which in turn would accelerate entry of major suppliers into the marketplace with their new and improved materials [44].

2.2 Fused Deposition Modeling: Processing options and considerations

The technology was invented by Scott Crump (founder of Stratasys) which led to the formation of Stratasys in 1989 and the attribution of FDM patents to Stratasys in 1992 (some of the FDM patent schematics can be seen in Figure 8) [80]. However, only until the 2000s, mainly due to the expiration of its seminal patents, has FDM gained popularity, giving rise to Makerbot Inc. [81], the RepRap Project, Fab@Home and the hobbyist FDM movement overall [63].

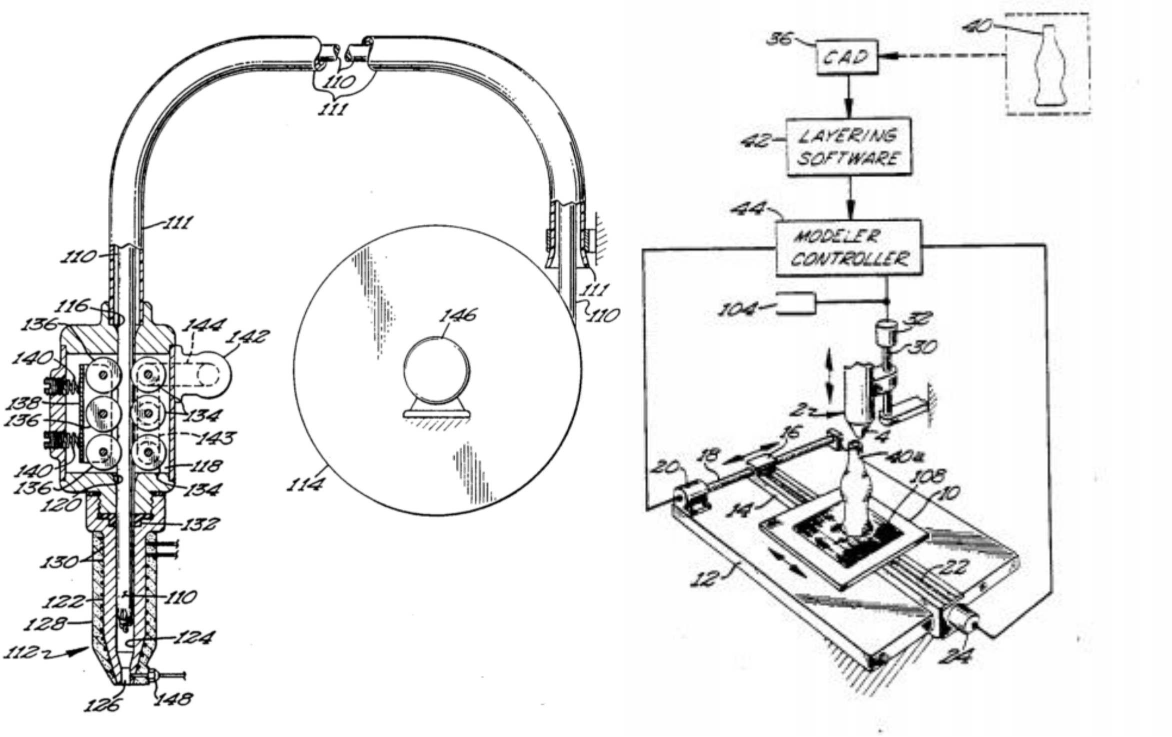

Figure 8 - Patent schematics of the FDM process [80].

In the basic mechanism of FDM, a virtual model is converted into STL (Standard Triangulation Language) format and opportunely oriented. After that, the STL file is loaded into the slicing software or the specific machine-computer interface platform. Subsequently, the sliced file is uploaded into the FDM machine, that starts printing with the required settings. After completion, the part can be removed from the platform and, if necessary, post-processed.

The FDM machine is basically a computer numerically controlled gantry machine, generally carrying two miniature extruder head nozzles, one for the modeling material and the other for the cases an overhanging section has to be produced. Overhanging features can be described as any feature that doesn't have anything under it holding up in the model (Fig. 9). In this cases, a removable support structure has to be created using another nozzle to deposit the support material. After the completion of the part the bits of the support material can be removed from the part manually (in case of simple geometries) or chemically (for deep cavities, or hard to reach places) [82].

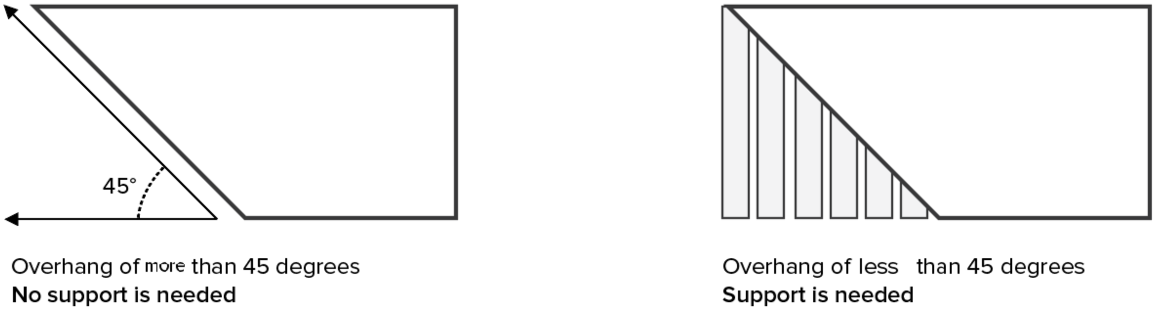

Overhang of more than 45 degrees
No support is needed

Overhang of less than 45 degrees
Support is needed

Figure 9 - Overhanging features. Any feature with tangent angles less than 45º with respect to the build platform needs to be supported while it’s being printed (adapted from [137]).

In the FDM process, parts are fabricated by extruding a molten filament through a heated nozzle, that is temperature controlled, in a prescribed pattern onto a platform (Figure 10). As the material is deposited, it cools, solidifies and bonds with the adjoining material. When one whole layer is deposited, the base plate moves down by an increment equal to the height of the filament and the next layer is deposited [83]. The subsequent layer is deposited on the material previously deposited, and this process continues until a complete part is produced. For thermoplastics, the chamber of the system is maintained at constant temperature (72 ˚C in case of acrylonitrile- butadiene-styrene), above the glass transition temperature in order to relax the thermal stresses and to solidify the deposited material [82].

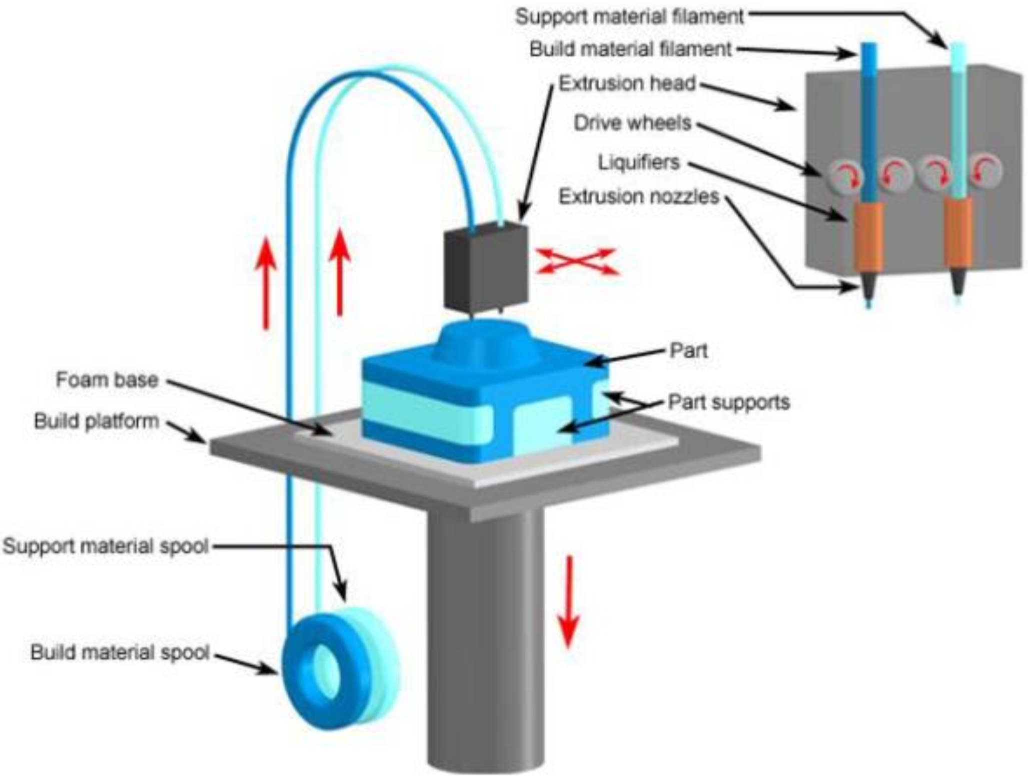

Figure 10 - Schematic of the components in a characteristic FDM machine [136].

FDM machines typically comprise several modules that must cooperate to guarantee the production of high-quality parts. The key modules are labeled in Fig. 11 and include material handling and extrusion, material heating and melting, motion systems and controls, and build platform and environmental controls [63].

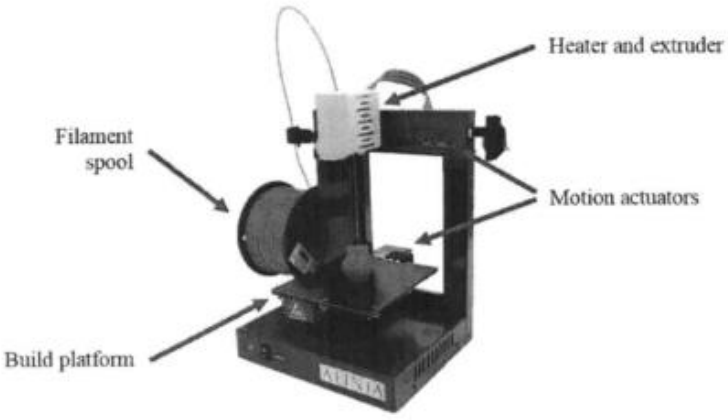

Figure 11 - Basic modules of a FDM machine [64].

The filament (generally 1,75 mm or 3 mm in diameter), initially coiled inside a spool (Fig. 12), rides tangent to the surface of the drive wheel and ideally moves at a velocity equal to that of the drive wheel surface. The drive wheel is often powered direct-drive from a stepper motor for low-speed, high-torque purposes with simple position control. The traction maintained between the drive wheel and the filament side is preserved by the normal force applied by the pinch wheel. To enhance traction, the drive wheel employs knurls shown in Figure 13, which dig into the filament. However, the pressure on the filament between the wheels should be designed so as to avoid crushing of the filament.

Figure 13 - Acrylonitrile Butadiene Styrene (ABS) filament spool [139].

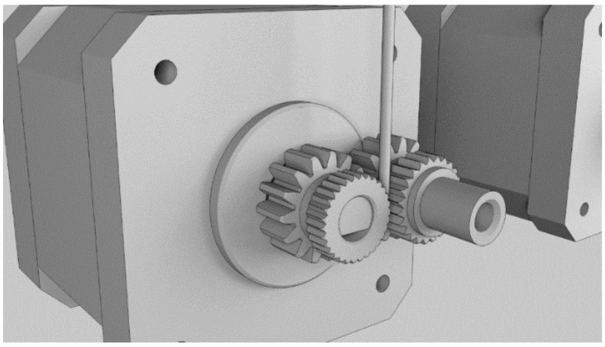

Figure 12 - Representation of driver wheels with knurls [138].

The solid filament body forces the molten material to advance in the liquefier below, which is responsible for the heating and melting of the filament, and is considered the core of the FDM system. The liquefier (Fig. 14) is generally a metal block, placed upstream the extrusion nozzle, with a channel machined for the filament/melt to flow through. The major liquefier elements consist of the liquefier chamber/channel, heater block, heating element, and temperature sensor. The heating element transfers energy to the heater block which stores thermal energy and uniformly conducts it to the liquefier chamber. In Stratasys systems, the channel is connected to a disposable print head which is surrounded by the liquefier. Resistive heating is typically used with either a coiled heating element surrounding the liquefier chamber or one or more cartridge heaters embedded in the liquefier assembly. In either case, the system is designed to maintain a uniform temperature throughout the liquefier. A single thermocouple is used in conjunction with the heating element and a controller to maintain constant temperature [84]. Selection of materials is critical to a well-functioning heater. The heater block and liquefier chamber should be made of a high thermal conductivity material such as aluminum or copper to ensure uniform heating [85].

Heat flux to the feedstock material must be sufficient to bring it to a melted state. The amount of melt in the liquefier will depend on the heat flux and the material feed rate. Conventional liquefiers components are destined to reduce heat flow towards the upper end of the liquefier body. Minimizing that heat flow upwards is necessary to save energy during the printing process, as the more heat is lost from the heat block, the longer must the resistance work keep the objective nozzle temperature at an appropriate level. Secondly, if that temperature fluctuates too much, it could eventually lead the nozzle channel to obstruction and discontinuous flow, with the consequent loss of final quality of the part [86]. Hardware maintenance and durability reasons also justify the need to prevent upstream heat flow. As 3D printed parts are occasionally used to fix the liquefier to the printing gantry, prolonged over temperature at the top of the liquefier could lead those parts to failure or irreversible deformation making them non-functional. In effect, PLA, a material typically used in FDM 3D printers, starts to experience deformation at 35 °C [87].

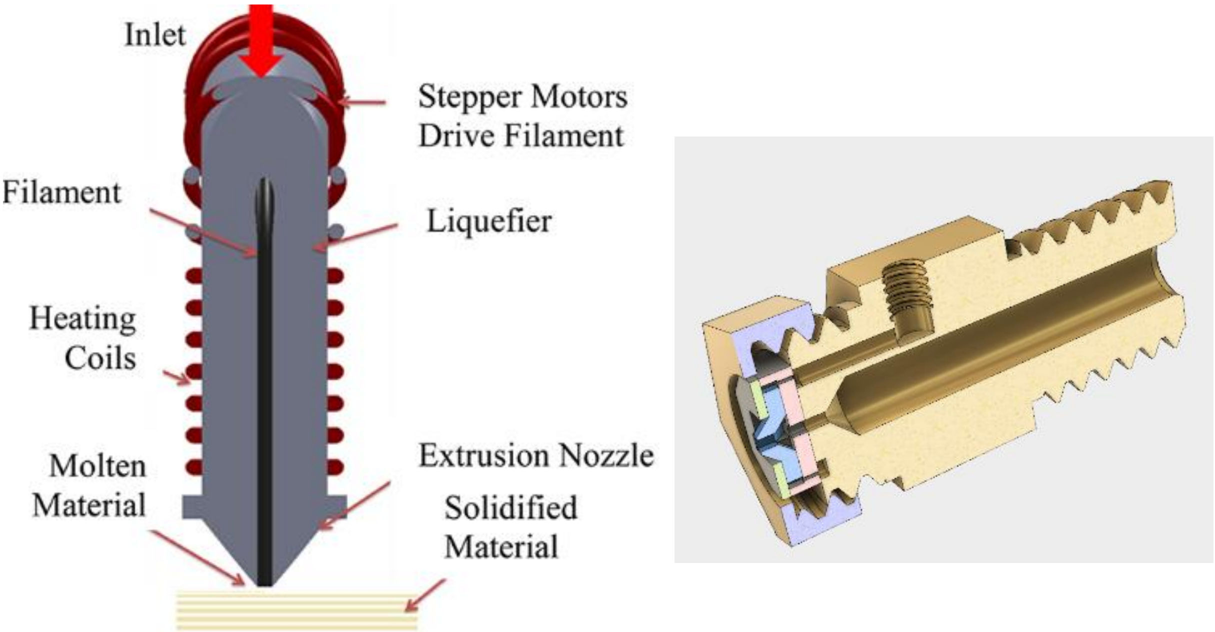

Figure 14 - Schematic of a cross section of a typical liquefier (left, adapted from [140]) and of an extrusion nozzle (right, [141]).

A circular orifice extrusion die referred to as the nozzle sits at the end of the extrusion mechanism. The nozzle is responsible for the diameter constriction of the filament, and its temperature must be kept constant to ensure a correct material flow. These nozzles control the diameter of molten filament flowing from the extruder assembly and typically range between 0.1 and 1 mm in diameter [88]. Internally, the nozzle features an inlet diameter, outer diameter, and conical reduction segment, which is tapered to prevent dead zones as shown in Figure 14 (right). The nozzle is directly connected to the liquefier output and as a result has similar performance requirements such as process temperature, corrosion resistance, and high thermal conductivity [85].

The print head/liquefier assembly is attached to a gantry that enables motion in the x and y directions. The velocity at which the print head/liquefier can move, and ultimately the speed of part fabrication, is primarily limited by the stiffness of the construction of the gantry. The size of parts that can be printed is limited by the dimensions of the gantry [86].

The extruder assembly lays material upon a surface referred to as the build platform. This surface is a critical element of the system design. The purpose of this platform is to provide a flat, level surface with good adhesion properties to ensure the initial layers of the print are fixed to the same location for the duration of the print, but not so immobilized that the part cannot be removed after the completion of the print process.

Temperature control is another critical component to ensuring geometric quality of FDM printed parts. If temperature is not controlled, thermal gradients develop within the part through the cross section and the height, resulting in warping of the part during the build process [89], [90] as can be seen in Figure 15. The typical solution is to maintain the build platform at an elevated temperature of approximately 70-90 °C for ABS [91]. If a heated build platform is not used, the machine will often instead feature temperature control of the entire print chamber [91]. In this option, the build volume is encased in an enclosure and thermally sealed to maintain an internal temperature.

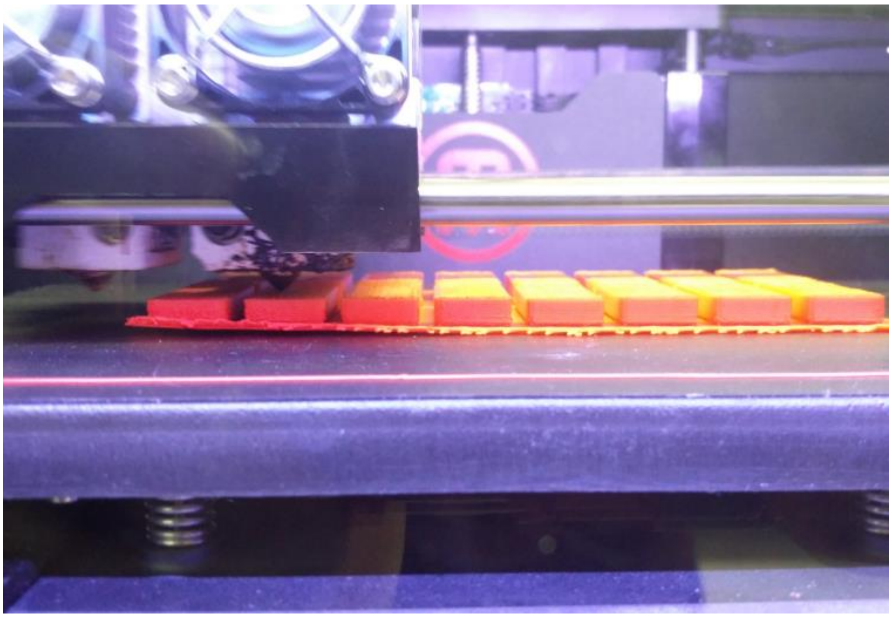

Figure 15 - Warping caused by a thermal gradient developed within the part [142].

2.3 Print macro- and micro-structure

Having done an overall description of the FDM process and its components, a microstructure analysis will be made in order to have a better understanding of the quality of the parts made by this technique. But before, it is necessary to contextualize and introduce some definitions:

- Perimeter: Outer surfaces of the part in the XY plane. The perimeter is an outline of the current cross section, laid as a continuous bead of polymer. Perimeter thicknesses may vary among printers and slicing software/algorithms.
- Infill: The structure composing the density of the part. Part infill may vary between 100%, which means fully dense, and 0%, which means shell or perimeter only. Hollow parts are allowed different infill patterns such as rectilinear patches or honeycomb which will affect the part's mechanical performance.
- Base: The top and bottom infill surfaces of the part. These surfaces are distinguished by normal infill by always being fully dense and may also differ from the perimeter by having different thicknesses.

An example of a typical cross-section of an FDM printed part is shown below in Figure 16.

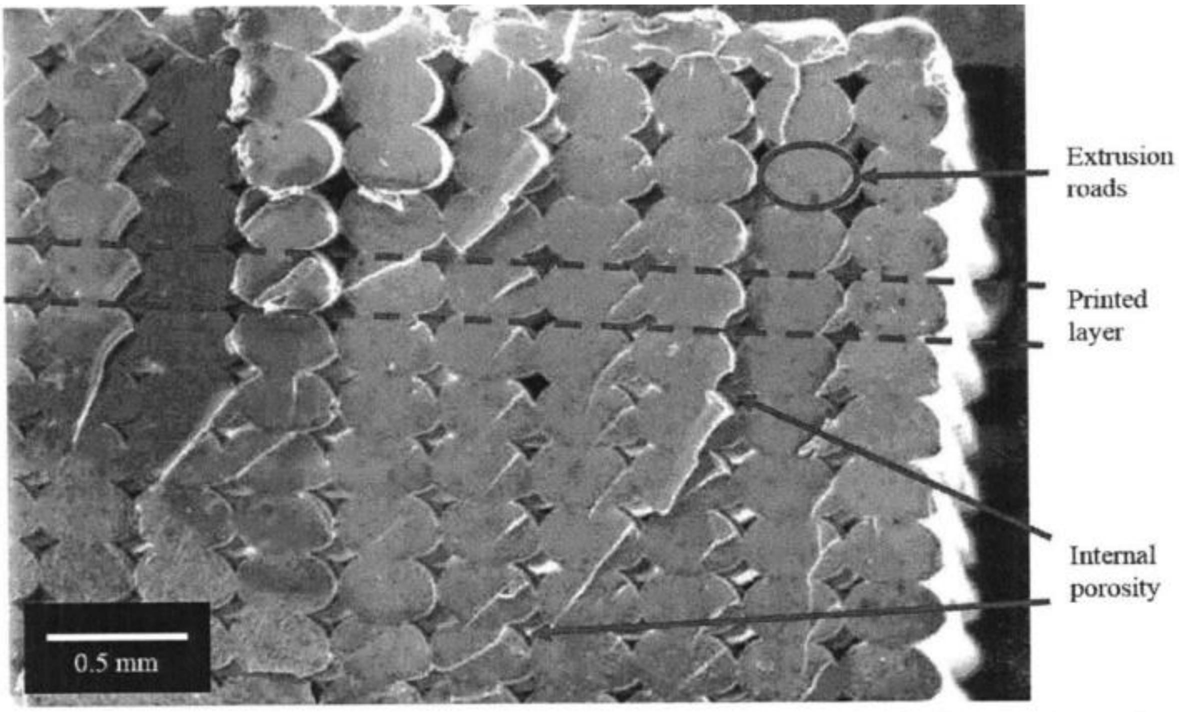

Figure 16 - Scanning Electron Microscope (SEM) picture of FDM part fracture surface reveal porosity and non-circular road profiles [93].

It can be noted that the cross section of individual roads as deposited are non-circular despite a circular nozzle orifice. This is because the nozzle is used to spread the bead as it extrudes, reducing road distortion and maintaining flatness (Fig. 17). This technique is also used to achieve specific layer heights smaller than that of the extruded filament diameter.

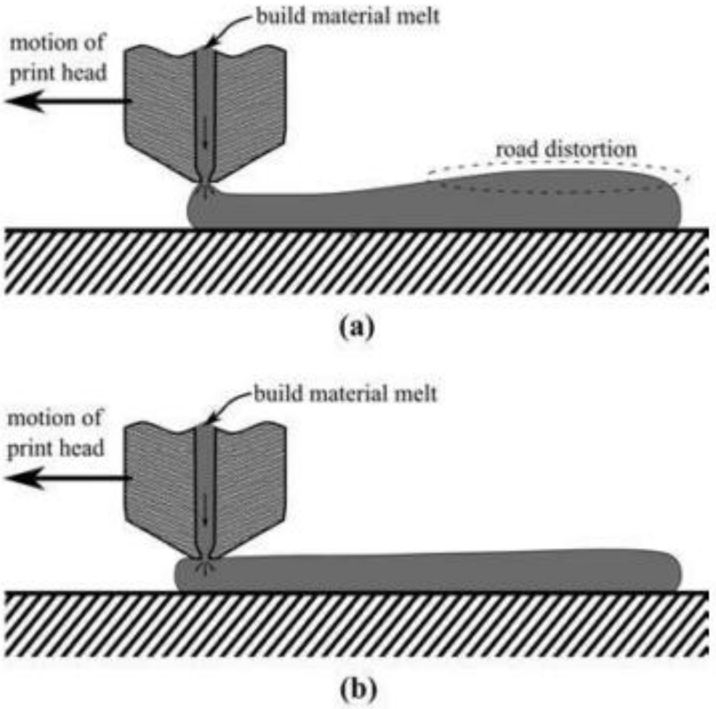

Figure 17 - Interaction of the print head with an extruded road. In (a) the road shape is distorted because the print head is above the deposited road. When the print head is in contact with the road, it helps to ensure a flat top road surface like in (b) [87].

The interaction of the tip of the print head with the bead may further influence the evolution of the shape of the printed road. As it spreads, the bead is cooling, and the viscosity increases until a solid state is reached. The final width of the road is one of the main factors that determines the resolution that can be achieved in the print process, as well as the contact area between neighboring beads. The rounded, oblong shape of the bead inevitably leads to small voids (porosities) in the printed part. The observed bulk porosity is a result of road geometries and infill strategies. The road cross section may not be circular but it is far from rectangular as observed in Figure 16.

Even for a software defined fully dense part, the printer is unable to fully remove the natural corner fillets of the molten material roads. This limitation manifests itself as porosity between beads and layers in the XZ and YZ planes. Porosity can also exist in the XY plane as a defect between infill and perimeter roads shown in Figure 18. Although the cross section may be rectangular, the extrusion orifice is still circular and so some amount of road overlap is required to achieve fully dense XY cross sections. Unfortunately overlapping roads often leads to material overflow and geometric inaccuracies. This clash can thus be thought of as two schemes for laying roads, optimization for accuracy or strength, where the first leaves internal voids [63], [84].

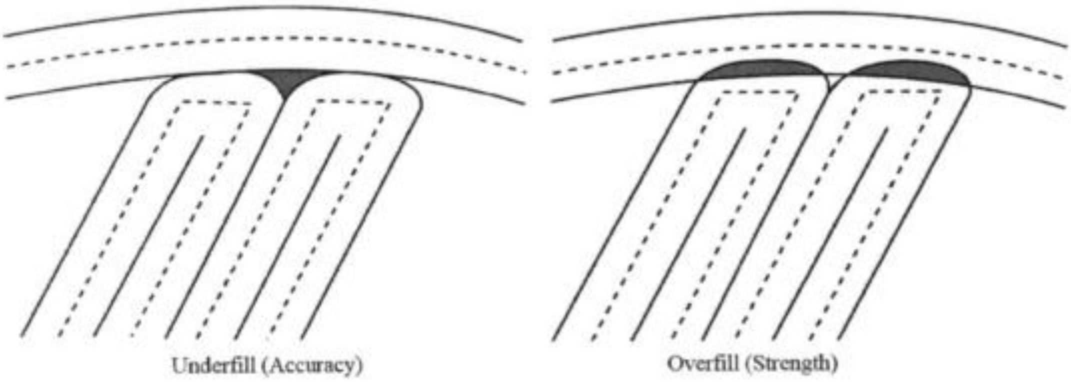

Figure 18 - Types of infill strategies may leave voids near the perimeter/infill boundary [64].

In addition to internal voids, there are other defects common to FDM parts. A bulk non-ideality derived from the road-by-road, layer-by-layer construction methods is part anisotropy [84]. Ideally, parts should exhibit consistent properties for all directions of loading. FDM parts however exhibit different mechanical properties when loaded in their Z direction (building direction) when compared to their X or Y directions. With the mechanical properties in the building direction often being the weakest and most critical. This is because the X and Y directions have continuous lengths of material which will be inherently stronger than interlayer bonding [92]. Thus, it can be realized that the microstructure of FDM printed parts, is a product of manufacturing parameters (including width of road, layer thickness, deposition orientation and gap sizes between filaments) and has an impact in their mechanical properties.

FDM parts also contain a number of geometric defects and non-idealities as a result of the process and process control. Surface roughness, which is a result of the layer construction process and the corner fillets on road cross sections, is minimal on vertical faces, the error increases with shallow angles or curved surfaces (Figure 19). A strategy that attempts to minimize this defect is to print in increasingly smaller layer heights or introduce a smoothing operation during post-processing [63]. However, there exists an inherent tradeoff in AM between layer resolution and the build time. While a higher layer resolution (smaller layer thickness) provides a better surface finish, it increases the build time as more layers are necessary to build the part.

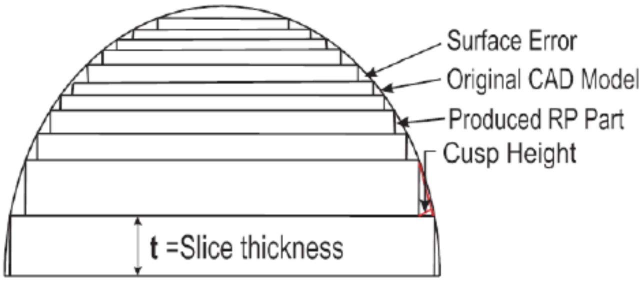

Figure 19 - Effect of decreasing layer height of a FDM printed part on its surface roughness [64]. Similar to conducting an integral, a larger layer thickness results in a poorly approximated curvature of the part. This build error is also called as the "stair-stepping" effect [143].

FDM printers have a different resolution along different orthogonal axes. The minimum feature resolution is dictated not only by the nozzle diameter, but also by the positioning of the build mechanism and the positioning of the nozzle mechanism, which normally involves the use of gearboxes and motors.

Although layer height can be controlled with intelligent spreading using the nozzle, no such technique is available for controlling road width because material still leaves the nozzle at its diameter. It is observed that many slicing algorithms will opt to ignore features below the printer resolution threshold. Unfortunately, the only solution currently is to print with a smaller diameter nozzle. Still, this motivates the necessity to design around fine nozzle diameters in order to print high-resolution features.

Another problematic occurrence in FDM printing is material overflow that can occur on high acceleration moves such as cornering or layer changes as seen in Figure 20.

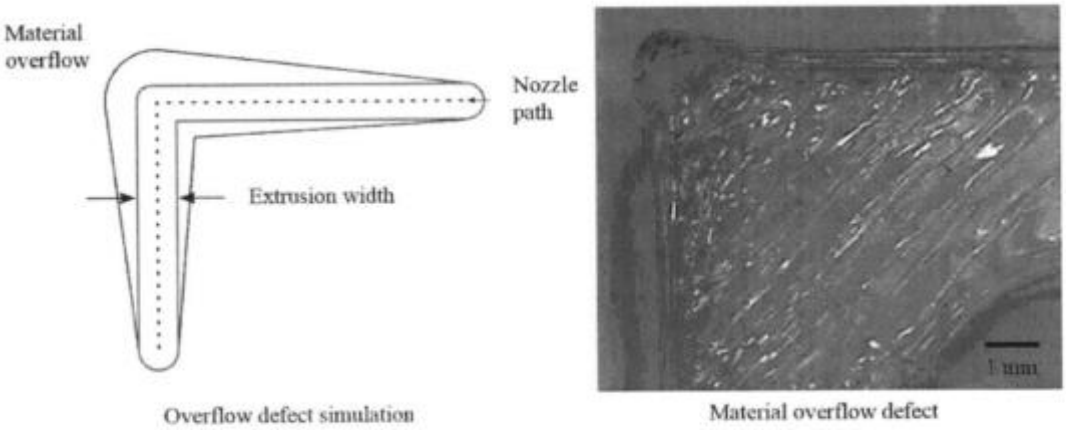

Figure 20 - Example of a material overflow defect on part corner (adapted from [64]).

In these instances, the motion axis will slow or pause without stopping material extrusion and as a result material pools in a single location, which overflows the target dimension of the part. A common arrangement to lessen material overflow is to pause material extrusion by retracting filament while cornering or changing layers. Another way to avoid the occurrence of material overflow is to minimize acceleration and deceleration stages. This can be achieved by avoiding sharp corners in the designing stages of the part and replacing them with curves for example [93]. In any case, well-tuned coupling between motion axis and extrusion are key to producing high-quality parts.

Another key way of optimizing the FDM printing process and respective products quality is to follow some guidelines [94] for designing and orienting parts with supported features that can minimize the use of support material, or even eradicate it, such as:

- The volume of required support material depends on the orientation of the parts. For example, ensuring that the part is oriented such that a flat surface is printed directly on the print bed can help minimize the amount of support material needed, which can increase the surface quality and the success rate of the part (Fig. 21a; Fig. 21b).
- Creating parts where all of the overhanging features are at angles greater than 45 degrees with respect to the build platform will eliminate the need for supports. Using teardrop shapes with chamfered tops for holes is recommended (Fig. 21c).

- Printing chamfers at appropriate angles instead of fillets, will eliminate the need for supports and will make for better printing overall. Fillets, as any curved surface, have non-constant angles and will therefore require supports on the bottom half of the curve, resulting not only, in a higher chance of print failure but also in a poor surface quality if the part does succeed (Fig. 21d).

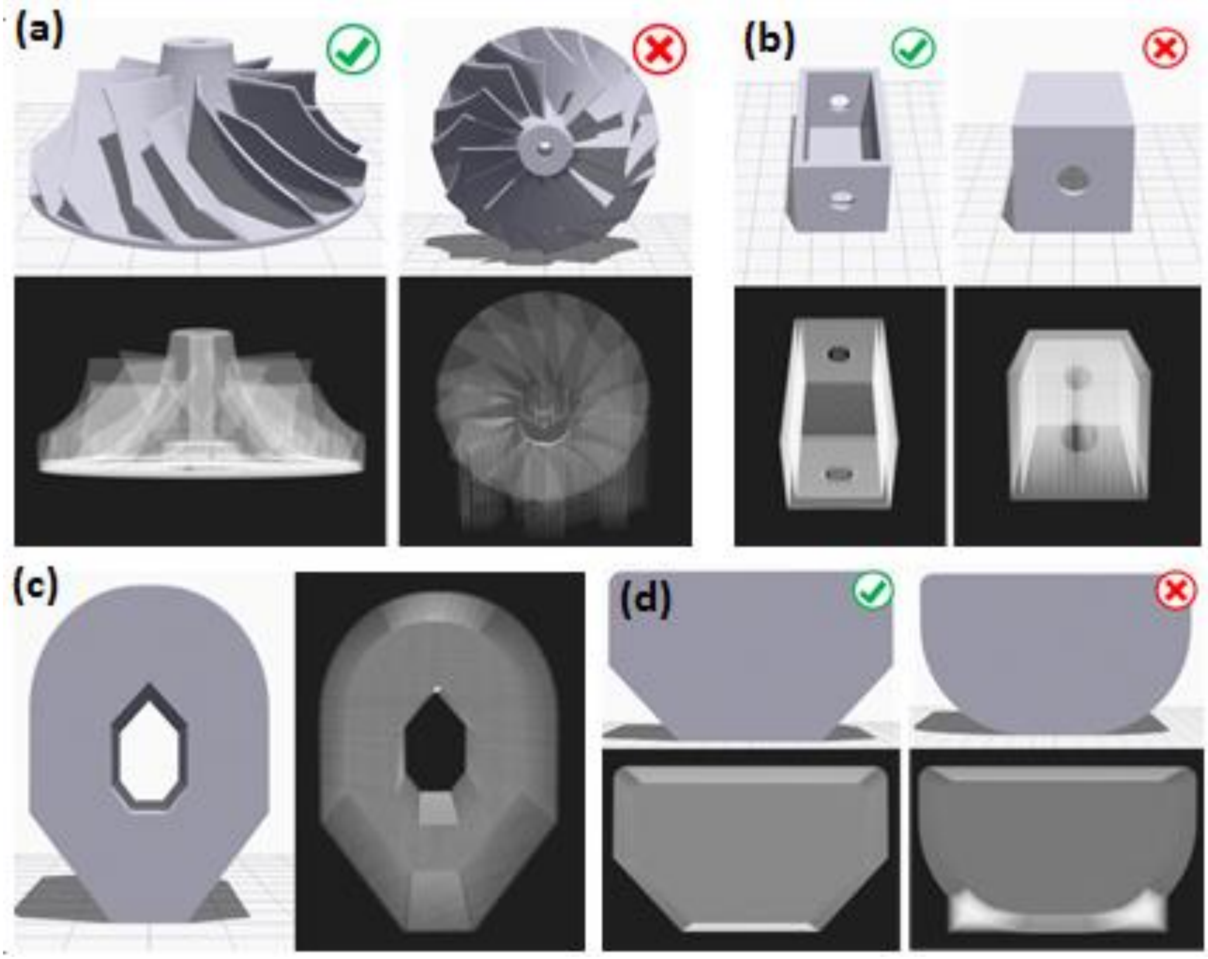

Figure 21 - Some examples of the guidelines mentioned above [94].

Designing for FDM manufacturing takes just as much effort as designing for any other manufacturing process. In fact, when it comes to designing FDM printed parts, one has to consider all aspects inherently connected to the process in order to select the manufacturing parameters that give the intended characteristics to the part, in the most efficient way.

2.4 Material range in FDM

The majority of materials used in FDM systems are based around an amorphous thermoplastic polymer that is delivered to the machine as either pellets or filament feedstock as shown in Figure 22.

Figure 22 - In FDM systems, the material is usually delivered in pellet form (up, [144]) or filament form (down, [145]).

Normally pellets are cheaper than filament because filament is made out of pellets and the final step in the production process of filament is skipped. However, pellet fed systems require the use of a screw extruder, in which molten pellet polymer slurry is advanced through the barrel by a screw auger and forced through an extrusion die at the end. Screw extruders are large, heavy and increase complexity and, therefore, they are typically not found in commercial FDM systems, making filament feedstock the standard material medium for this AM method [63].

FDM printed parts are usually fabricated from thermoplastic polymers that have rubbery, viscous phase above the glass transition temperature and facilitate fusion between subsequent layers. Currently, the amount of thermoplastics compatible with FDM platforms is somewhat narrow due to the particular properties needed for a successful print such as a relatively low glass transition temperature (Tg), melting point (Tm), and a low tendency to shrink upon solidification. The Tg will have an effect on how easily the material will be extruded, how the parts will shrink during the cooling process (therefore, affecting the warping) and the thermostability of the final part [95]. Additionally, most modern commercial systems are closed, preventing the use of any materials other than those of the manufacturer [96].

The material most commonly used in FDM is acrylonitrile butadiene styrene (ABS), followed by polycarbonate (PC), polylactic acid (PLA), polyphenylsulfone (PPSF), polyetherimide (ULTEM) and blends of these materials.

Polylactic acid (PLA) is a favorite in hobbyist printers due to its ease of use, good geometric stability, variety of colors, and biocompatibility. However, its brittle mechanical properties and low softening temperature constrain its use to hobbyist and aesthetic purposes. [63]

Acrylonitrile butadiene styrene (ABS) is a thermoplastic used by both hobbyist and professional systems. It is more difficult to work with than PLA but offers greater mechanical strength and stability which are in more cases suitable for end use parts. Production grade systems such as the Fortus series by Stratasys have the capability of printing high-temperature, high-performance thermoplastics such as ULTEM or PPSF [97]. These are of greatest interest for automotive and aerospace applications and have been certified for use in aircraft duct components among other applications [63]. ULTEM, PPSF or even PC are high-performance thermoplastics, but the use of such materials presents some limitations, as these materials require higher extrusion temperatures and, therefore, only a relatively small amount of FDM systems have the capacity of printing these. The most common material choices that exist for FDM machines and corresponding properties are listed in Table 4.

Table 4 - Properties of frequently used thermoplastics in FDM systems [97].

Description	Grade	Ultimate Tensile Strength [MPa]	Tensile Modulus [MPa]	T_g [˚C]	T_m [˚C]
Acrylonitrile butadiene styrene	ABS plus	33	2200	108	NA
Acrylonitrile butadiene styrene	ABS-M30	32	2230	108	NA
Acrylonitrile butadiene styrene	ABS-M30i	36	2400	108	NA
Acrylonitrile butadiene styrene	ABSi	37	1920	116	NA
Polyamide 6	Nylon 6	67,6	2232	-	NA
Polyamide 12	Nylon 12	53 (yield)	1310	178	NA
Polycarbonate	PC	57	1944	161	NA
Polycarbonate - acrylonitrile butadiene styrene	PC-ABS	41	1900	125	NA
Polycarbonate	PC-ISO	57	2000	161	NA
Polylactic acid	PLA	26	2539	63	NA
Polyphenylsulfone	PPSF/PPSU	55	2100	230	NA
Polyetherimide	ULTEM 9085	69	2150	186	NA

Since the number of usable polymer types is limited, the number of applications that can benefit from FDM is as well limited. A strategy for increasing the applicability of FDM is the development of new material systems with a wider range of physical properties. A logical path to engineering the physical properties of materials used in FDM is the development of composites where the matrix material is a printable thermoplastic. Not only to maintain compatibility with the process but also due to the ease of material blending and compounding, combined, generally, with low prices of the matrix materials (less than a 20 dollars per kilogram of ABS).

The augmenting of polymeric materials can be done in many ways, one being the compounding of particulate or fiber-reinforcing additives in the creation of thermoplastic matrix composites, or through the compounding with other polymeric materials in the creation of polymer blends [95]. Moreover, the ability to make a composite monofilament compatible with material extrusion 3D printers through conventional screw extrusion equipment offers rapid data turns in novel materials development.

There are multiple examples of successful implementation of such material modifications for use in FDM [33], [98]–[100]. In effect, rapid growth in the availability of blended and composite filaments is being witnessed for both hobby and industrial applications. New materials further highlight the versatility of the FDM process by increasing the breadth of its material landscape and demonstrating their viability as functional end use parts.

An important aspect to keep in mind with composite materials development is the characterization of the influence of reinforcing agents on the mechanical properties (in comparison with the material alone) and their relation with the fracture morphology of the failed components, namely, the characterization of the effect of reinforcing agents on the mechanical properties (compared with the matrix material alone) and a correlation of changes to the fracture morphology of the failed components are important aspects to consider [95].

2.5 Improvements in FDM technology

In the previous section some aspects and or limitations of the FDM process were discussed. Essentially, FDM is a developing process and as such there are still some aspects that should be improved (preferentially in a cost-effective way) in order for FDM to get established in production, such as:

The variety of materials available for use in this technology should increase in order to broaden its application as discussed previously.

Greater dimensional control should be achieved in order to print parts with tighter geometric tolerances. Much of the error in accuracy observed in the final part arises from shrinkage during cooling and solidification or warping as uneven heat distribution creates internal stresses within a part. As FDM equipment becomes larger and physically bigger parts are produced, these thermal gradients and their impact on dimensional tolerances will become increasingly important. Therefore, it is important to develop ways to prevent or diminish these problems [101].

Surface finish of printed parts should be upgraded in order to minimize roughness and avoid time-consuming post-processing techniques. This can be achieved, for example, with an improvement in the resolution of the FDM process [101]. The maximum feature resolution that is typically achievable on extrusion AM systems is on the order of 100 µm.

Mechanical properties of the produced parts should be enhanced so they can maintain their integrity during service.

Of all this research areas, mechanical performance is one of the most challenging ones and the focus of this work is towards it. In fact, the final mechanical properties of parts obtained by means of the FDM process, are, often, uncertain, since they are influenced by a large amount of production parameters, which are really difficult to combine, in order to increase the strength and the stiffness of the built parts. As a consequence, the practical application of components processed by the FDM (and in general by AM techniques), is limited to relatively low-loaded products and to those whose failures do not lead to severe effects [102].

Principally there are two ways to overcome the limitation of lower mechanical properties in FDM built parts:

One way is to control and optimize the operating parameters so that higher mechanical properties and fully dense structure of built parts can be obtained. Thus, increasing applications of FDM requires developing functional relationship between process parameters and mechanical properties in order to gain good understanding on how the variation in operating parameters will determine the variation in the mechanical properties of the fabricated part.

Another promising way is to develop new materials having unique properties and excellent performance.

Mechanical properties of FDM parts are governed by their microstructures, which are determined by manufacturing parameters including width of filaments, layer thickness, deposition orientation (raster angle), and gap sizes between filaments. These parameters are illustrated in Figure 23. The main production parameters affecting the mechanical behavior of FDM processed components (in particular strength and stiffness) are summarized in Table 5. By selecting manufacturing parameters, FDM processes can potentially produce parts with desired properties. However, this is not an easy task since the FDM technology involves conflicting process variables making it difficult to understand effectively how these parameters are affecting together the mechanical properties [103], [104]. Thus, to fully exploit this potential, subjects concerning the fabrication process and the mechanical properties of FDM parts should be extensively investigated. Actually, for the optimization of any manufacturing process, a deep knowledge of the process itself is required. Such knowledge could be gained either by experimentation or by analyzing the physical mechanisms of the process.

Table 5 - FDM manufacturing parameters that affect mechanical properties and respective definitions [102].

Parameter	Definition
Part Building Direction	It is the direction along which a specimen is grown up, while it is being generated. It is perpendicular to the surface of each deposited layer and therefore strictly related to the part orientation in the build platform.
Bead width	Width of the filament deposited by the FDM nozzle. Bead width can’t be smaller than 1.2-1.5 times the size of the nozzle diameter [105]. The most common values range from 0.3 mm to 1 mm [106].
Raster Angle	Inclination of the deposited beads with respect to a reference direction (usually, load direction). A typical setting consists in +45°/-45° alternate layers.
Air Gap	Distance between two adjacent deposited filaments of the same layer. The default value is usually zero, meaning that the beads touch each other [106]. A possible alternative is a positive gap, meaning that a gap is present between adjacent rasters, or a negative gap, implying that the bead tracks are overlapped.
Layer Thickness	Thickness of the deposited bead and therefore of any single layer. It is usually one half of the bead width.
Number of Contours	The building procedure is usually arranged, so that the filament is initially deposited along the component edge. Upon the completion of the full edge, another filament is deposited at the inner side of the previously deposited contour. This procedure is followed until the specified number of contours has been deposited. The inner part of the component is finally filled by inclined rasters until the completion of the first layer. The method is repeated for the generation of all the other layers.

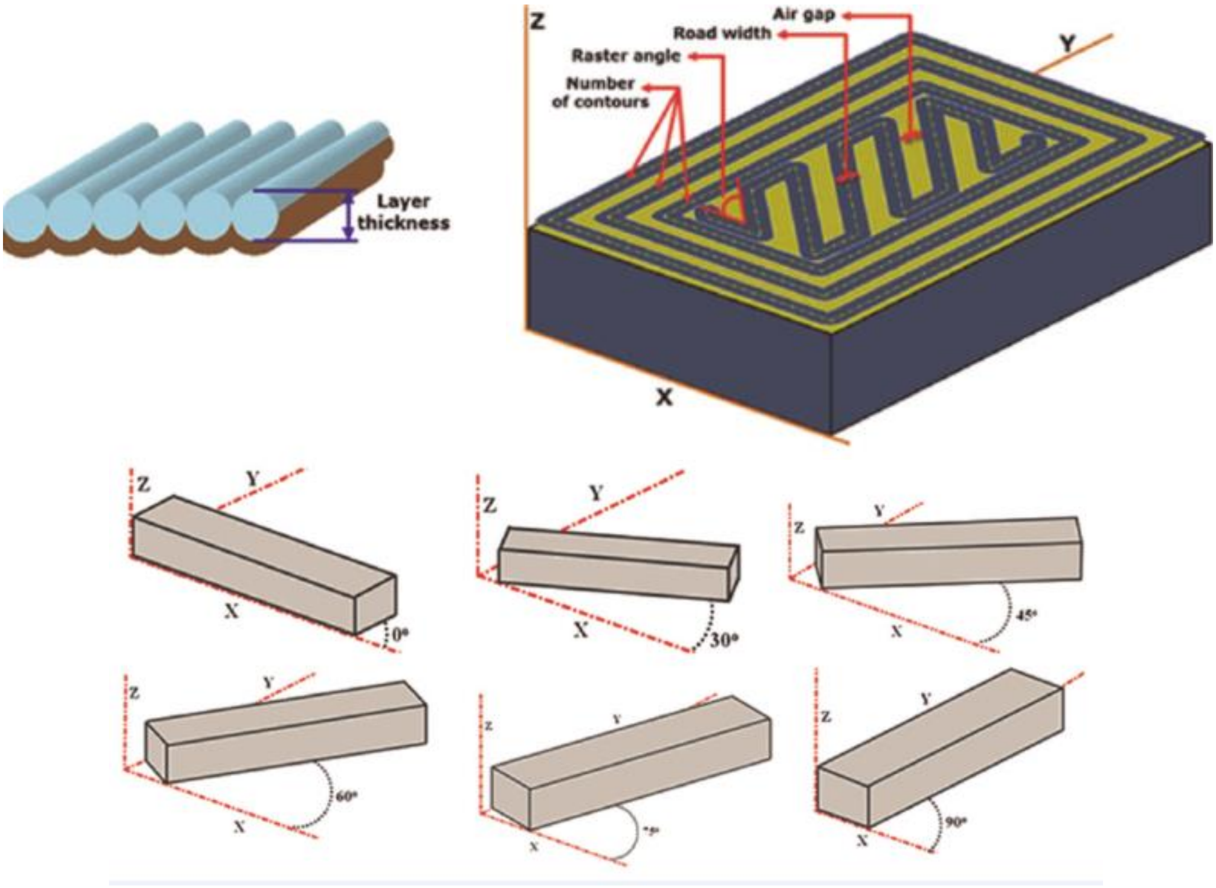

Figure 23 - Visual representation of the indicated FDM parameters. The build orientation of the part can rotate along axes X, Y and Z [146].

The real system is simulated by the models that aim to predict its performance. A model is the abstract representation of a process that establishes a relation between input and output quantities. Understanding the relationships between process parameters (inputs) and final part properties (outputs) will be critical in enabling design of parts for manufacturing, in developing methods of qualifying parts for industrial use and in facilitating more intelligent materials development strategies.

Models encountered in literature can be divided into three major categories, namely analytical, numerical and empirical ones, depending on the development approach:

The analytical models are the output of the process's mathematical analysis, taking into consideration the physical laws and the relevant physical processes. The main advantage of such models is that the derived results can be easily transferred to other pertinent processes. The limits of the analytical modelling are determined by the underlying assumptions, decreasing the complexity of reality and, therefore, often lead to imprecise results;

The empirical models, on the other hand, are the outcome of a number of experiments, whose results are evaluated. Once the model is developed, the coefficients are determined, and then the empirical model can be verified by further testing. The quality of the models' results is limited in the special conditions of the specific process. Their major advantage, compared with that of the analytical models, is that they require minimum effort;

Numerical models are somewhere in the middle of analytical and empirical models. In essence, they take into account the physics of the process but a numerical step-by-step method is employed over time in order for useful results to be produced.

Physical phenomena associated with the FDM process are complex and diverse, including melting/ solidification and heat transfer and many others. In the literature several models can be encountered to mimic the processes involved in FDM including heat transfer [107]–[111] and material deposition [112]. Indeed, most of the modeling conducted in FDM processes has been related to understanding the process itself rather than modeling the mechanical properties of the resulting parts [113].

However, there are some attempts made that can be found in literature to investigate the effects of some manufacturing parameters on the mechanical properties of FDM printed parts.

For instance, Sood et. al [114] performed an extensive study to understand the effect of five important parameters such as layer thickness, part build orientation, raster angle, raster width and air gap on the compressive stress of test specimens made of ABS P400. The study not only provides insight into complex dependency of compressive stress on process parameters but also develops a statistically validated predictive equation. Also, a parameter optimization was made, i.e., optimum values of process parameters were combined to achieve the maximum compressive stress.

Sood et. Al [104] evaluated the influence of the same manufacturing parameters but this time on other mechanical properties such as tensile, flexural and impact strength of ABS P400 test samples. Experiments were conducted based on central composite design (CCD) in order to reduce experimental runs. Empirical models relating response and process parameters were developed. The validity of the models was tested using analysis of variance (ANOVA) and optimal parameter setting for each mechanical property was determined.

Croccolo et. al [102] also conducted a study of the effects generated by the FDM production parameters on the tensile strength and on the stiffness of the generated ABS-M30 components, tackling the question from both the experimental and the numerical points of view. For this purpose, an analytical model was developed, which is able to predict the strength and the stiffness properties, based on the number of contours deposited around the component edge and on the setting of the other main parameters of the deposition process. The fundamental result of the work consists in the possibility of predicting the mechanical behavior of the FDM parts, once the raster pattern (dimensions, number of contours, raster angle) has been stated. The effectiveness of the theoretical model has been verified by comparison to a significant number of experimental results, with mean errors of about 4%.

Previously it was mentioned that one way of improving the mechanical properties of FDM printed parts was through the development of new materials. These new promising materials can be achieved, for example, via the reinforcement of the widely used thermoplastics, with fibers. However, a common and major drawback of producing composite parts via FDM is the need to produce a reinforced polymer filament compatible with existing FDM equipment, which is not a trivial task [115]. The composite materials to be used in the FDM should have appropriate flow, stiffness, flexibility and conductivity properties. The other critical properties required for high quality composite feedstock filaments for FDM include desired viscosity, strength and modulus. For instance, if the filament exhibits a low stiffness or high viscosity, buckling will occur just before the entrance to the liquefier, thus making FDM processing impossible. Filaments require a high stiffness and lower melt viscosity to a useable level [98].

Work has been done to develop new thermoplastic composites with improved mechanical properties, relatively to the existing thermoplastics for the FDM process. Recently, Weng et. al [116] tested the tensile strength of ABS/OMMT (organic modified montmorillonite) nanocomposites prepared by FDM. Results showed that the addition of 5 wt% OMMT improved the tensile strength and the elastic modulus of 3D printed ABS samples by 43% (from 27 MPa to over 39 MPa) and 200% (from 1,2 MPa to 3,6 MPa) respectively.

Gray et al. [117] developed composite filaments of thermotropic liquid crystalline polymers (TLCP) in polypropylene (PP) matrix for the FDM process with the aim of enhancing the tensile properties and the functionality of the FDM made prototypes. They produced a TLCP/PP (20/80 wt%) composite monofilament investigated the effects of various factors on the tensile properties and morphology of the prototypes. The elastic modulus of the composite monofilament TLCP/PP (20/80 wt%) was increased by 93% relatively to neat PP monofilament (from 0,98 GPa to 1,9 GPa) while tensile strength values remained similar.

In 2014, Tekinalp et al. [118] investigated the development of short carbon fiber (CF) reinforced ABS composites to improve the strength of the ABS filament for FDM processing. FDM composite specimens were manufactured with different fiber contents: 10, 20, 30 and 40 wt%. With the latest demonstrating nozzle clogging during the printing process. Therefore, the results obtained from the 40 wt% fiber content specimens were rejected. The obtained results showed an increase in both the elastic modulus and tensile strength of the CF/ABS parts when compared to the unreinforced specimens. As the fiber content increased, so did the mechanical properties. Compared with the unreinforced ABS parts, CF/ABS (30/70 wt%) specimens' tensile strength and elastic modulus were enhanced by 81% and 600%, respectively. Additionally, the authors compared composites fabricated by both compress molding and FDM and although high porosity was observed in FDM fabricated composite parts, they still exhibited comparable tensile strength and elastic modulus compared to those produced by compress molding, which reinforces the potential of the use of FDM to build functional parts. Actually, in 2014, Love et al. presented that carbon fiber reinforced ABS composites developed using FDM process could exhibit specific strength approaching aerospace-quality aluminum [67].

Most of the past research work is directed to the development of new materials with short fibers mixed for reinforcement [119]. The printing of fiber reinforced thermoplastic materials through FDM with continuous reinforcement fibers is more challenging but has also been achieved already. One example being Matsuzaki et al. [120] , which utilized a unique dual extrusion method. This study, in which a print head was custom built, yielded continuous carbon fiber PLA composites with strengths of up to 190 MPa in tensile, and 133 MPa in flexure. Their values were 435% and 316% higher respectively, compared with the PLA only specimens.

Additionally, a company called Markforged released a commercial FDM printer, which is capable of fabricating continuous fiber reinforced thermoplastic composite parts using a variety of materials called the Mark One (shown below in Figure 24). The materials include carbon fiber (CF), glass fiber and Kevlar fiber along with a nylon filament material (matrix).

Figure 24 - Mark One Printer: The world's first 3D printer designed to print continuous carbon fiber [137]

Since its release, research work has been developed in order to evaluate and mechanically characterize the parts produced by this 3D printer.

A study by Klift et al. [121], in 2016, assessed carbon fiber reinforced specimen produced by the Markforged Mark One printer in order to obtain the mechanical properties of FDM printed carbon reinforced thermoplastic composites. Three varieties of tensile specimens were produced and were 10-layer thick. The varieties of specimens were: 100% Nylon parts and continuous carbon fiber reinforced specimens having either 2 or 6 layers containing carbon fiber reinforcement. The three types of specimens were tested and a value of 35,7 GPa of elastic modulus was obtained for the 2-layer carbon reinforced specimens, which is massive when compared with the results obtained with the Nylon specimens of only 900 MPa. A factor that may have affected the results in this study however is that the test specimens were cut post-printing in order to remove 'discontinuities' and excess matrix material which may influence the strength results. These authors observed large deviations between individual test results, with standard deviations in tensile strength as high as 22%, obtained from the specimens containing 6 layers of CF reinforcement. A test was performed to evaluate the accuracy of the predicted elastic modulus of the composites using the rule of mixtures. However, the tensile test specimen's results did not live up to the rule of mixing for composites due to the delamination of the layers and void formation. The obtained results shown that a specimen deviates more from the rule of mixture when it has more carbon reinforced layers, and, therefore, more void spaces. The authors also found that specimens with six layers of carbon fiber reinforcement exhibited larger tensile strength than those with two layers of fiber reinforcement.

In the paper of Dickson et. al [122], a more detailed evaluation of the performance of 3D printed composites with continuous carbon fiber reinforcement was carried out. This study also involved the fabrication of nylon composites with Kevlar® and glass fibers and the mechanical performance of all three composite types were compared both in tension and flexure. The influence of fiber orientation, fiber type and volume fraction on mechanical properties were also investigated. The results were compared with that of both non-reinforced nylon control specimens, and known material property values from literature. It was demonstrated that of the fibers investigated, those fabricated using carbon fiber yielded the largest increase in mechanical strength. Its tensile strength values were up to 6.3 times that obtained with the non-reinforced nylon polymer. In fact, the tensile testing of the fabricated FDM composite parts generated strengths of up to 368 MPa with a fiber volume fraction of 35%, which is higher than the 310 MPa reported for Aluminum 6061-T6 [123].

Melenka et. Al [2] also used the Mark One printer to produce continuous fiber reinforced thermoplastic composites. However, the aim of the work done differed from the cited above, in the manner that the aim of this research was to, not only evaluate the elastic properties of the continuous fiber reinforced 3D printed structures, but also to provide the designers a methodology for determining their elastic properties using a Volume Average Stiffness (VAS) method. This model calculates an average stiffness of the material, taking into account the properties of all phases of the heterogeneous media and their interaction. Three different volume fractions of the fibers within the 3D printed specimens (4.04, 8.08 and 10.1%) were evaluated in order to study the effect of the fiber reinforcement volume fraction on the mechanical properties of each type of specimen. The experimentally determined elastic modulus was found to be 1767.2, 6920.0 and 9001.2 MPa for fiber volume fractions of 4.04, 8.08 and 10.1% respectively. The predicted elastic moduli were found to be 4155.7, 7380.0 and 8992.1 MPa. The model results differed from experiments by 57.5, 6.2 and 0.1% for the 4.04, 8.08 and 10.1% fiber volume fractions. These results are all summarized in Table 6.

The predictive model gives the capability to calculate the elastic properties of fiber reinforced 3D printed parts and allows for designers to predict the elastic properties of fiber reinforced 3D printed parts to be used for functional components, which require specific mechanical properties.

Table 6 - Comparison of experimentally determined and predicted values of the elastic modulus for fiber reinforced 3D printed specimens with different fiber volume fractions in [2].

Fiber volume fraction [%]	Experimental determined elastic modulus [MPa] (StDev)	VAS model predicted elastic modulus [MPa]	% Difference
4.04	1767.2 (39.3)	4155.7	57.5
8.08	6920.0 (272.3)	7380.0	6.2
10.1	9001.2 (314.2)	8992.1	0.1

A common drawback of models currently available in the literature is that their domain of validity is slightly limited because they are adjusted to specific materials and particular parameter intervals [83]. Therefore, it is important to determine the domain of validity of each model, and to do that, experimental tests need to be carried.

3 Materials and Methods

In this section the experimental and modeling work is developed and explained. The first step is to take a look into the printing process, as well as capabilities and limitations of Mark One Printer in order to better understand the following sub-sections.

3.1 Mark One Printer Introduction

The Mark One Printer, introduced in the previous section, is a FDM printer that is capable of fabricating nylon and continuous fiber reinforced thermoplastic composite parts using an array of fiber materials. There are two key modules that allow the printer "brings parts to life". The first being its mechanical systems and the second one is the cloud-based program known as Eiger [124], which is responsible for the handling of the appropriate files for the printer (MFP file). Eiger acts as the interface software between the computer and the printer. This program is responsible for the creation, storage and changing of files and is available to any device capable of connecting to the internet.

Once a part has been uploaded into Eiger (in STL format), it can be selected for printing. Before the part can be printed, the part must be edited in the Part View page. On this page, the selected part is displayed and a series of options can be chosen to tailor the part and obtain the desired characteristics for the desired application. Alongside these options is the estimated print time for the part as well as the volume of fiber and of nylon required. The first major option is whether the part is exclusively made of nylon, or includes fibers as can be seen in Figure 25.

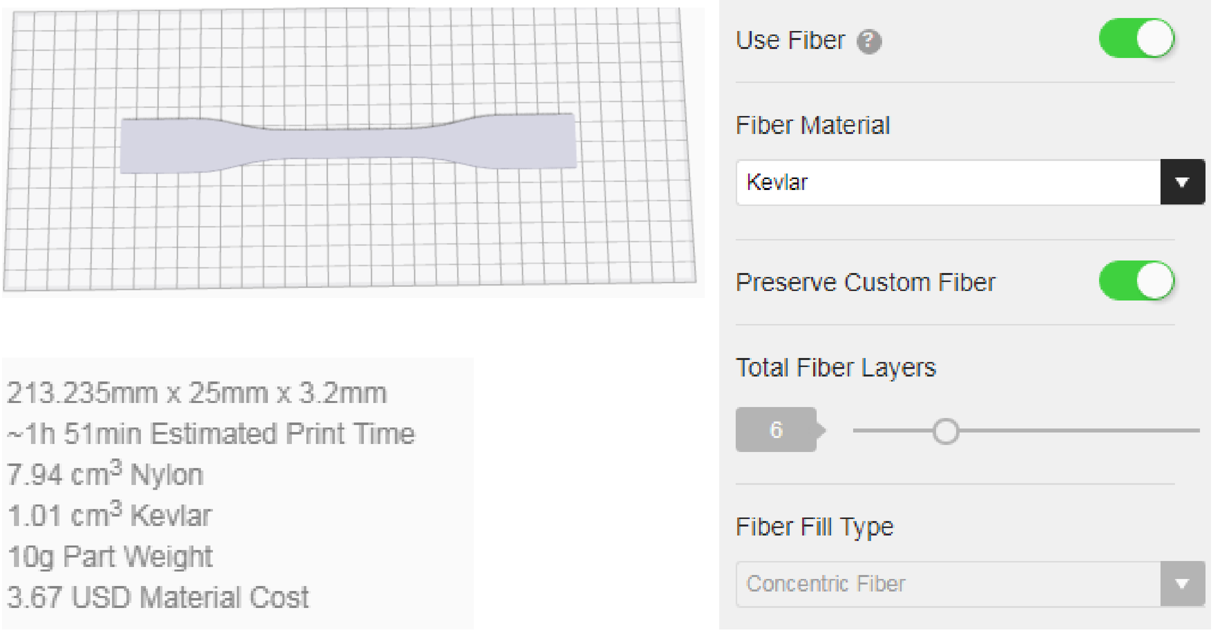

213.235mm x 25mm x 3.2mm
~1h 51min Estimated Print Time
7.94 cm^3 Nylon
1.01 cm^3 Kevlar
10g Part Weight
3.67 USD Material Cost

Use Fiber ☑
Fiber Material: Kevlar
Preserve Custom Fiber ☑
Total Fiber Layers: 6
Fiber Fill Type: Concentric Fiber

Figure 25 - Demonstration of some aspects of the Eiger Part View page. In the left, a view of the part is displayed, alongside some estimations of material used, estimated print time and cost. And in the right a portion of the available option is shown, including the one for including fiber reinforcement.

Presently, there are three available fiber fill types: Concentric, Isotropic (Beta) and Full Fiber (Beta). However, some fiber materials aren't compatible with all fiber fill types. For example, Carbon Fiber only the concentric fiber fill type is accessible.

The concentric fiber fill type produces a series of rings inside the part that follow the outer wall and, in some cases, when possible and wanted, the inner wall. This fiber fill type is ideal for reinforcing the part along the walls of the part but the number of concentric rings (chosen before printing) is restricted by the space within the part. Minimum amount of rings is one concentric ring and the maximum depends on the part. The number of fiber reinforced layers also has to be nominated bearing in mind that the part cannot be made fully out of fiber reinforced layers, since that, if that were the case, there would be no protection for the fibers.

While the concentric fiber fill type is ideal for reinforcing the part along the walls, the Isotropic (Beta) and Full Fiber (Beta) fiber fill styles, are perfect for reinforcing the part in a specific direction or directions. These fill types will create a somewhat rectangular fill within the part and are again restricted by the space within the part. These fiber fill types come with an option to control the fiber angle as well as the number of fiber reinforced layers. An example of each of the fiber fill types is shown below, in Figure 26.

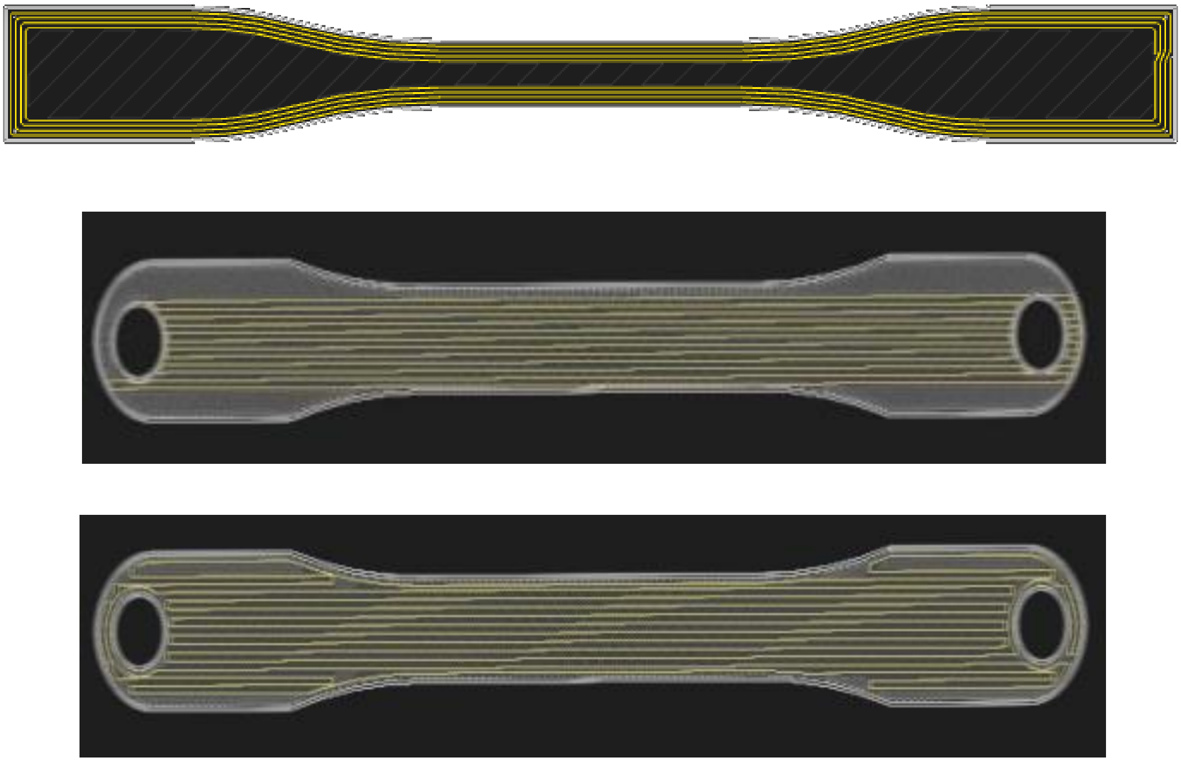

Figure 26 - Fiber fill types available in Eiger: Concentric (top); Isotropic (middle); and Full Fiber (bottom).

The nylon sections of the part can also be edited. For instance, a series of options are available which can make it easier to remove parts from the print bed. After those are a series of options that control the internal structure of the part. These options are the fill pattern and nylon fill density. The nylon fill pattern has three options: Hexagonal, Triangular and Rectangular. The nylon fill density ranges from 0% to 100% and as the density increases, so does the printing time. A density of 50% is recommended by the software.

The final decision to make is the number of ceiling and floor layers as well as the number of wall layers. Both options serve the same purpose of protecting the fibers within from external elements and the minimum number of each of these layers is one.

After the fulfillment of this form, there are two options. To save the part and begin the printing process straightaway or to observe the individual layers of the part and take the next step of the part customization, by going to the Internal View page. In this part, Eiger displays the internal structure of the part and allows further customization to each individual layer. A bar will appear at the bottom of the page, which displays different segments to distinguish the layers throughout the part.

Each layer is can be tailored to a point that the only option mentioned earlier that cannot be altered is the nylon infill density. This could result in parts with all three nylon and fiber fill types [125]. Throughout the customization, Eiger will show the estimated print time along with the volume of fiber and nylon in the part as demonstrated in Figure 27.

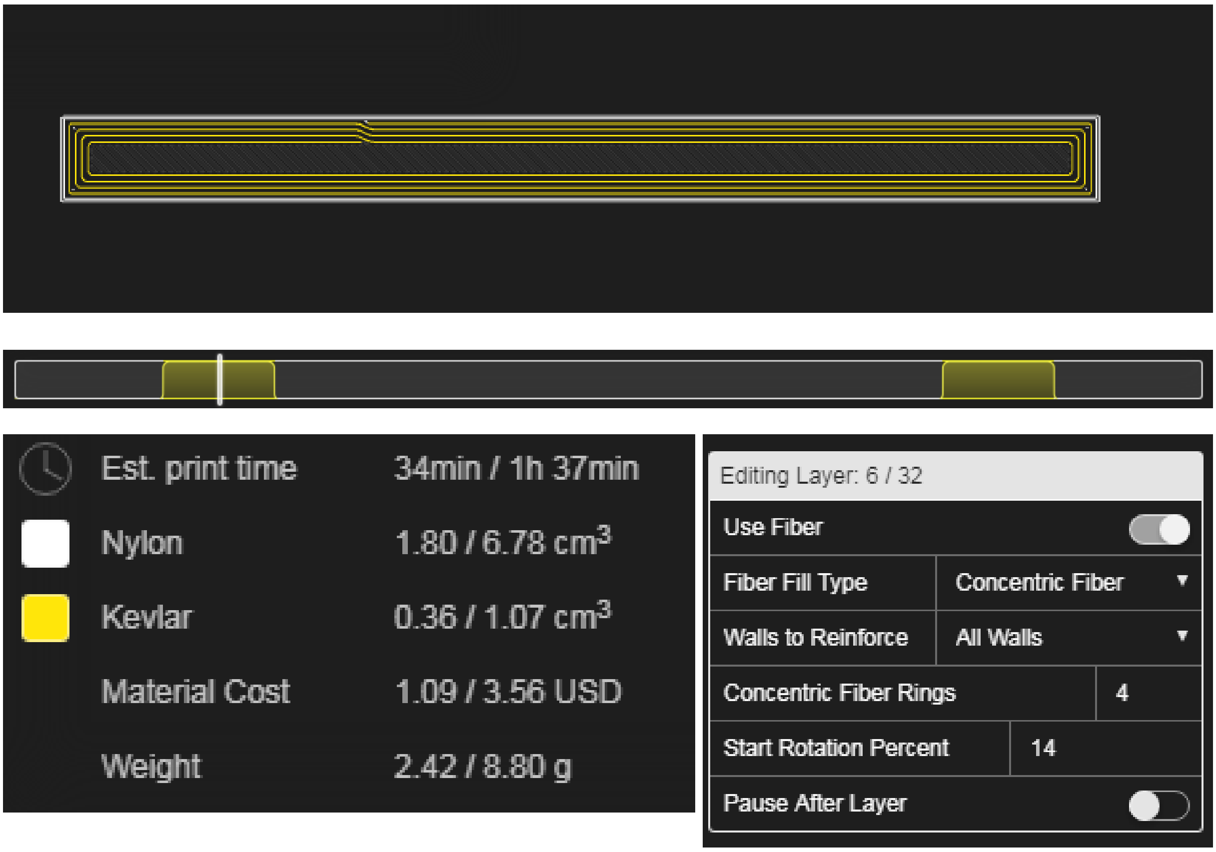

	Est. print time	34min / 1h 37min
⬜	Nylon	1.80 / 6.78 cm^3
🟨	Kevlar	0.36 / 1.07 cm^3
	Material Cost	1.09 / 3.56 USD
	Weight	2.42 / 8.80 g

Editing Layer: 6 / 32

Use Fiber	●
Fiber Fill Type	Concentric Fiber ▾
Walls to Reinforce	All Walls ▾
Concentric Fiber Rings	4
Start Rotation Percent	14
Pause After Layer	○

Figure 27 - Eiger’s Part View layout showing the customization of a simple layer. The part being edited can be seen (top) as well as the relative position of the current customized layer in the bar below the part. The printing time and the required quantities of each material are constantly displayed.

After completing the Internal View step, the last stage is to create the build file (MFP file), which the Mark One will use to print the part(s). This is done by editing the Print page, which shows the print bed with the chosen part placed in the center of the bed. Once the chosen part or parts have been placed onto the print bed, Eiger performs calculations and returns the estimated print time and volume of fiber and nylon inside all the parts in the build.

The build file can then be saved onto Eiger for future use and exported as an MFP file. The final step to the production of the part is to transfer the file to the Mark One printer [125]. After that the part finally starts being printed through the extruder, which contains two nozzles, one for each material. Each nozzle works separately and never at the same time.

3.2 Parts design and production

In order to reproduce the experimental work done by Melenka et. al, cited above, specimens with the same manufacture parameters, materials and geometry were produced. The specimens for mechanical testing were fabricated using a Mark One Printer. The sample geometry was produced according to ASTM D638-14 using a Type I geometry [126]. The test specimen geometry used in this study was created using SolidWorks 2015 SP4.0. The critical dimensions are shown in Figure 28.

The specimen geometry was exported as a STL file and loaded into Eiger. Samples were printed with a nylon filament (matrix) and a Kevlar fiber reinforcement. The material specifications provided by the manufacturer for these materials are displayed in Table 7. The printing parameters used to manufacture the test specimens are summarized in Table 8. Relative to the longitudinal axis, the raster angle of the nylon filament is alternated between +45◦/-45◦. This is the way Mark One Printer produces parts and cannot be arbitrarily changed. For example, if the first layer has the raster angle of 45◦, the next layer will have the opposite raster angle, and so on, throughout the total number of layers, until the part is done. The alternated raster angles have the aim of making the part more resistant in different directions.

A sneak peek of the Eiger's Internal View of the printed specimens is shown in Figure 29. In this figure, illustrations of different types of layers are displayed. The internal structure of the printed specimens will be important in the future sections of this work, including the development of the analytical model.

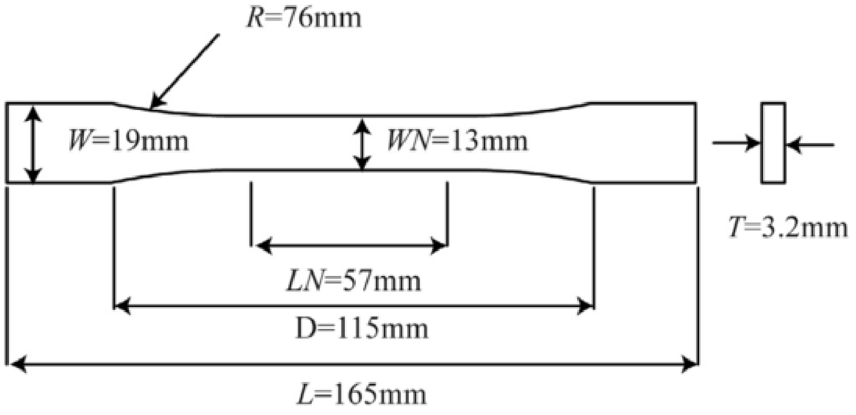

Figure 28 - Dimensions and geometry of the 3D printed specimens for tensile testing. The dimensions shown correspond to those recommended by the ASTM D638-13 standard for a Type I specimen. [2]

Table 7 - Properties given by the manufacturers for the materials (filament) used to produce the specimens [29].

Material Property	Nylon	Kevlar CFF
Tensile strength [MPa]	54	610
Elastic modulus [GPa]	0.94	27
Tensile strain at break [%]	260	2.7
Density [kg/m^3]	1100	1250

Table 8 - Manufacturing parameters of the printed specimens.

Matrix Material	Nylon
Fiber Reinforcement Material	Kevlar
Fiber Fill Type	Concentric
Number of concentric rings	0, 2, 4, 5
Fill pattern of matrix material	Rectangular fill
Layer height [mm]	0,1
Infill density [%]	10
Raster angle [◦]	+45/-45
Number of Roof & Top layers	4
Number of Infill layers	10
Number of shells	2 (one in each side)
Number of fiber reinforced layers	6
Total number of layers	32

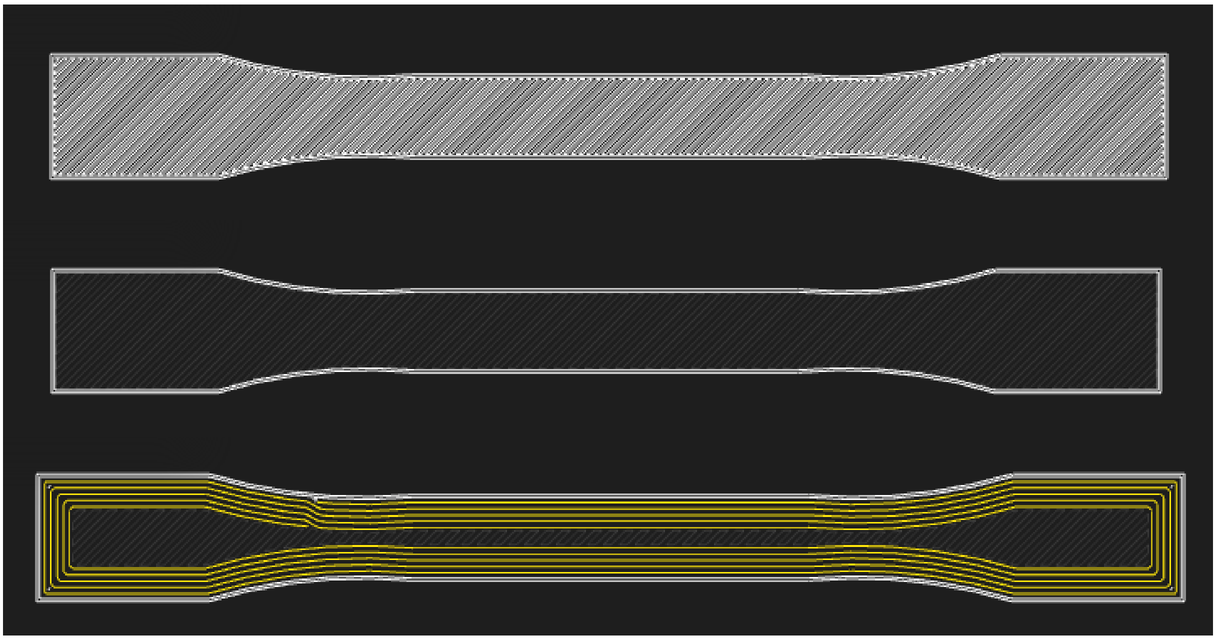

Figure 29 - Eiger's Internal View of the printed specimens. In the image, detailed examples of the solid (up), infill (middle) and fiber reinforced layers (bottom) are shown. In the examples, the 45° angle between the deposition orientation of the nylon filament and the longitudinal axis of the specimen can be examined. This angle is set by default and is not alterable in Eiger's interface. In all layers, it is important to note that a distinctive perimeter made of nylon filament is present.

Three dimensional printed samples were reinforced with concentric fiber rings. The number of possible rings ranges from none (pure polymer) to 5 rings for this geometry, with the limiting factor being the thin 13mm (WN in Figure 28) neck region. The number of concentric fiber rings was varied to quantify the effect of concentric rings on the mechanical properties of the 3D printed test specimen. Specimens were printed with 5 (5R), 4 (4R), 2 (2R) and no concentric fiber rings (0R) and can be seen below in Figure 30. For each type of specimen, 5 specimens were printed (all at once, with the relative position on the build platform accounted for) and tested.

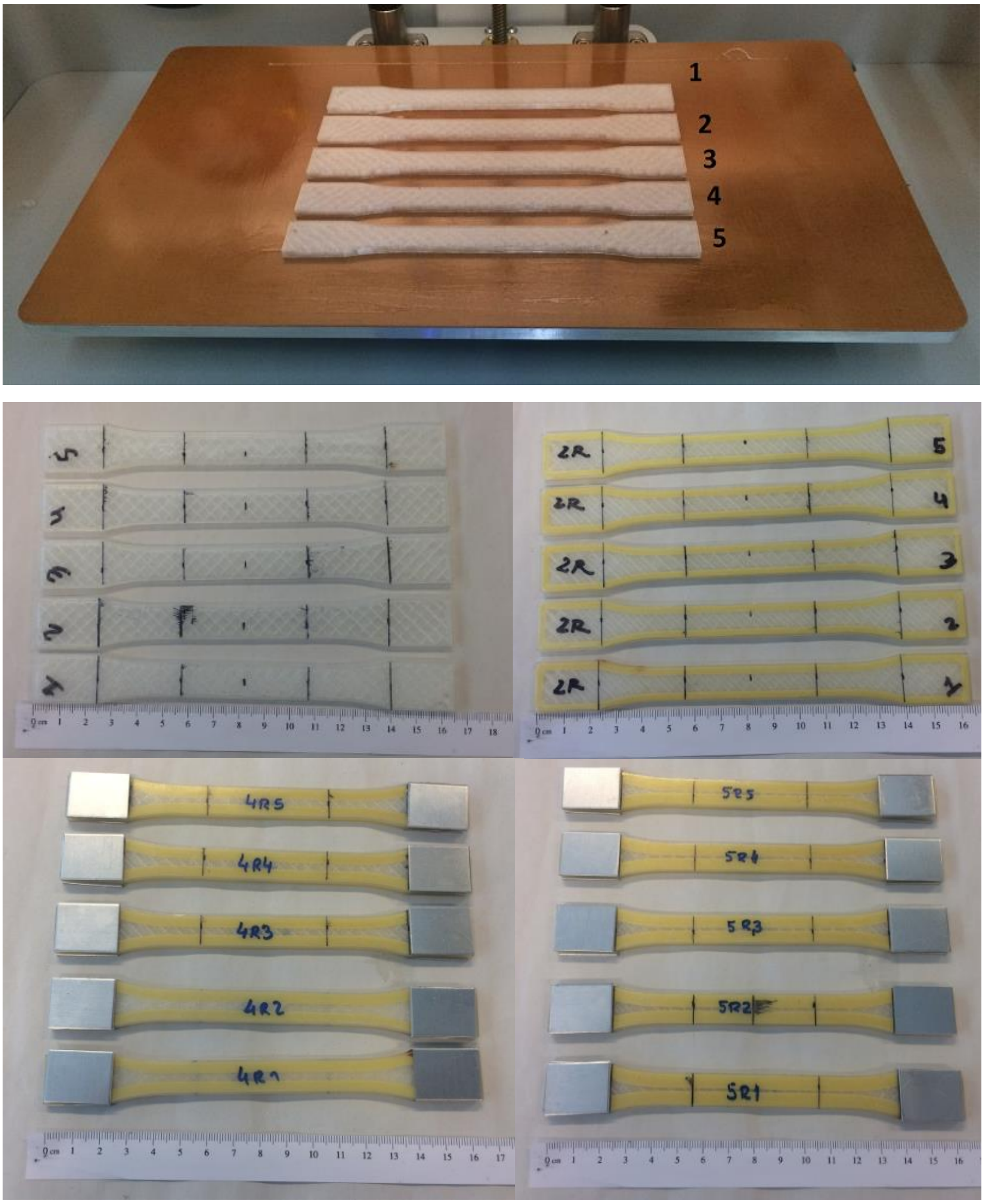

Figure 30 - The relative position of each specimen on the build platform is shown (up). The four types of 3D printed specimens: 0R, 2R, 4R and 5R (down). The names attributed to the specimens is shown. For example, in “2R1”, “2R” means that it is a 2-concentric ring reinforced specimen and the “1” means that it is the specimen printed in the number one location (upper image), and so on. This is to see if the relative position in which each specimen was created has any effect in its mechanical properties. It can also be observed that for the 5R specimens, the narrow section’s width doesn’t have space for any additional concentric ring.

3.3 Mechanical testing

Before performing any mechanical tests, printed samples were measured to evaluate the dimensional accuracy of the Mark One 3D printer. The gauge section width and thickness (T), shown in Figure 28 were measured using a digital caliper (Mitutoyo 0-150 ± 0.01mm) in order to determine the cross sectional area of the printed samples. For each dimension, three measurements were recorded and were found to be inside the appropriate tolerances dictated by the standard (ASTM D638-14) for all printed specimens. The results can be found in Appendix 1. The mass of each specimen was also recorded in order to obtain specific properties (specific stiffness and specific strength) of each specimen configuration. This analysis can be observed in Section 5.2.

Tensile tests were performed to the 3D printed specimens to determine their mechanical properties. The results of these tests are shown in Chapter 4. The test setup used to evaluate the 3D printed samples is shown in Figure 31. An INSTRON 4507 tensile testing equipment with a 200 KN load cell was used to apply loads to the test specimens. Strain of the test samples was measured using a 50 mm gauge length extensometer (INSTRON M20-52665-12). Samples were loaded at a rate of 5 mm/min. The results of these tests are shown in section 4.

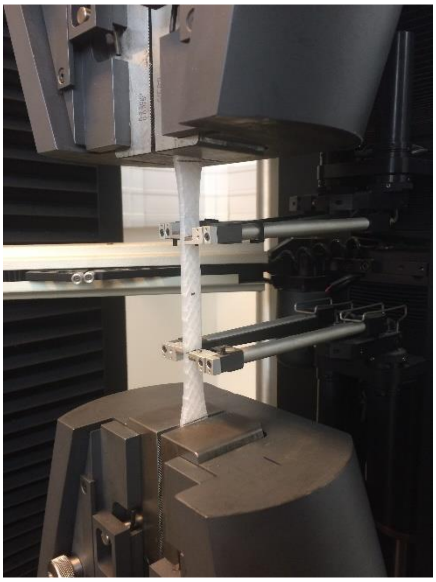

Figure 31 - Mechanical testing setup to evaluate the tensile properties of 3D printed specimens.

3.4 Volume Average Stiffness model

In parallel with the experimental tests, the Volume Average Stiffness (VAS) analytical model was developed, based on [2], in order to obtain a functional tool that predicts the effective elastic constants of the fiber reinforced printed specimens. The fiber reinforced printed parts comprise several different regions (Fig. 32), each with its own elastic constants.

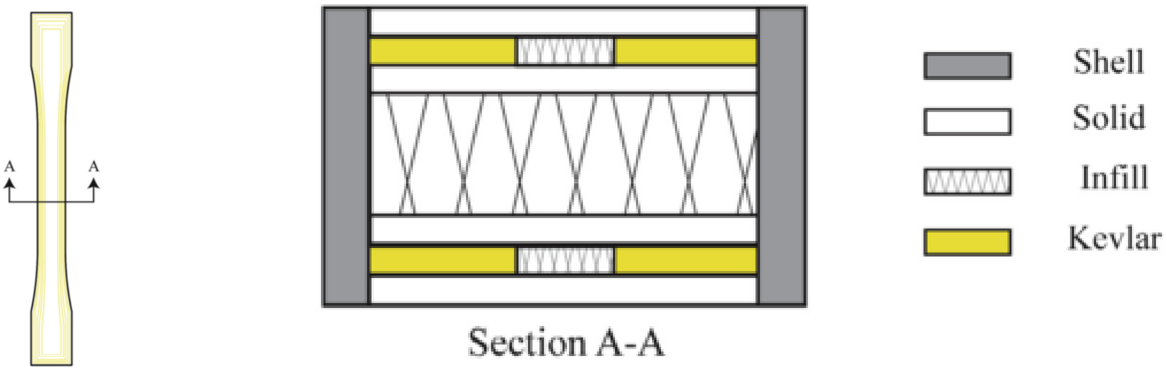

Figure 32 - Schematic of the regions of the fiber reinforced printed test specimens. In the left is the top view of the 3D printed test specimens. In the middle a cross-sectional view (Section A-A) is presented, showing all the constituents included in the cross section of the specimens with their respective names in the right (adapted from [2]).

In Figure 32 it can be seen that four distinct regions exist within the test samples cross section:

- Perimeter/shell layers that form the external structure of the test specimen. In this region the extruded nylon is oriented along the longitudinal axis of the test specimen;

- Solid layers which consist of closed layers of nylon. These layers have a considerably higher quantity of nylon inside them than the infill layers and exhibit alternate orientation between ±45◦ from the longitudinal axis. These layers are also printed before and after the fiber reinforced layers, forming a “sandwich structure”, with the fiber reinforced layer/layers in the middle. The printer does this automatically to improve the bonding between the fiber reinforcement and the nylon (matrix). The floor and ceiling set of layers are generally solid layers.

- Infill layers which consist of sparse layers of nylon. Similar to the solid layers, infill layers alternate orientation between ±45◦ from the longitudinal axis;

- Kevlar layers which consist of concentric rings of Kevlar fibers. The Kevlar fibers are oriented along the longitudinal axis of the test sample (in the neck section). The Kevlar layers also possess infill regions as the Kevlar yarns do not fill the entire cross-section of the test samples (Figure 29).

The analytical model takes into account the contribution of each of these regions and allows to predict the effective elastic modulus of the fiber reinforced 3D printed specimen. The analytical model has been developed as an Excel file to allow for rapid computation of the mechanical properties of a 3D printed structure.

In order to predict the mechanical properties of the Kevlar reinforced 3D printed samples the mechanical properties of the Nylon filament and Kevlar reinforcement were assumed, as some of the required specific mechanical properties were not specified by the manufacturer. For example, as will be shown ahead, it is necessary to know the shear modulus (G) of the Nylon filament for the determination of the micromechanical properties of the Nylon constituted regions (infill, solid and shell). The shear modulus (G) is not provided for the Nylon filament and was calculated based on the relation between elastic modulus (E) and Poisson's ratio of the material using Eq. (1) shown below.

$$G = \frac{E}{2(1+\upsilon)} \tag{1}$$

The assumed mechanical properties for the Nylon filament and Kevlar fibers are the same as the ones in [127] and are summarized in Table 9 and Table 10 respectively.

Table 9 - Assumed elastic constants of Nylon filament [29], [128].

Material property	Value
Elastic Modulus – E [GPa]	0.94
Shear Modulus – G [GPa]	0.35
Poisson's ratio – υ	0.35

Table 10 - Assumed elastic constants of Kevlar reinforcement [129].

Material property	Value
Longitudinal elastic modulus - E_{f1} [GPa]	79.8
Transverse elastic modulus - $E_{f2;}$ E_{f3} [GPa]	2.59
In-plane shear modulus – $G_{f12;}$ G_{f13} [GPa]	2.1
In-plane shear modulus – G_{f23} [GPa]	1.5
Poisson's ratio – υ_{12}; $\upsilon_{13;}$	0.33
Poisson's ratio – υ_{23}	0.1

3.4.1 Volume average stiffness method

As mentioned above, the effective elastic constants of the fiber reinforced 3D printed samples will be determined using a volume average stiffness method [130] that takes into account the contribution of each of these regions (considering the volume occupied by the constituents). The volume averaging method involves three main steps:

- Use of micromechanical models to determine the effective properties of the FDM printed components.
- A coordinate system transformation is applied to the solid and infill layers, to compensate for their misalignment with the longitudinal axis.
- Volume averaging of the stiffness matrices of each of the cross-sectional regions is performed.

To determine the micromechanical properties of the solid, infill and shell regions, the model developed by Rodriguez et al. is used to determine the unidirectional constants for a FDM component [1]. The model of Rodriguez et al. addresses FDM-printed parts as a plastic/void composite. The elastic properties for Nylon shown in Table 9 were used to determine the micromechanical properties of the shell, infill and solid layers. These micromechanical properties can be calculated using Eq. (2)-(7), where ρ1 represents the void density in each component. Void density for the solid, shell and infill sections were assumed to be 10%, 10% and 90%, respectively. The notation 1,2,3 represents the 1, 2 and 3 principal material axes and their orientation can be seen in Figure 33.

$$E_{11} = (1-\rho_1)E \tag{2}$$

$$E_{22} = E_{33} = \left(1-\sqrt{\rho_1}\right)E \tag{3}$$

$$G_{12} = G_{13} = G\frac{(1-\rho_1)\left(1-\sqrt{\rho_1}\right)}{(1-\rho_1)+\left(1-\sqrt{\rho_1}\right)} \tag{4}$$

$$G_{23} = \left(1-\sqrt{\rho_1}\right)G \tag{5}$$

$$\upsilon_{12} = \upsilon_{13} = (1-\rho_1)\upsilon \tag{6}$$

$$\upsilon_{21} = \upsilon_{31} = \upsilon_{32} = \upsilon_{23} = \left(1-\sqrt{\rho_1}\right)\upsilon \tag{7}$$

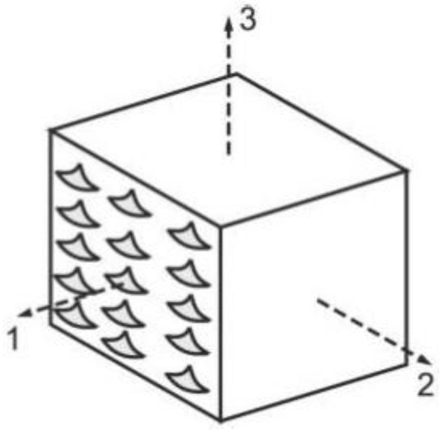

Figure 33 - Orientation of the principle material directions for a FDM printed part. The small areas within the face of the cube whose normal is coincident with axis 1 represent the voids existing in the FDM printed parts. The direction of axis 1 is considered the direction of the deposition of the material [1].

Once these micromechanical properties of the solid, infill and shell regions are determined, the compliance matrix, [S], of each region can be filled in, using the calculations shown in Table 11. These calculations can only be used for a transversely isotropic material, as is the case of the printed regions of the specimens and has 6×6 dimensions.

Table 11 - Elements of the compliance matrix of FDM printed regions. In the notation of this paper, “i” denominates the number of the line and “j” denominates the number of the column [1].

$\boldsymbol{S_{ij}}$	$\boldsymbol{j = 1}$	$\boldsymbol{j = 2}$	$\boldsymbol{j = 3}$	$\boldsymbol{j = 4}$	$\boldsymbol{j = 5}$	$\boldsymbol{j = 6}$
$\boldsymbol{i = 1}$	$\frac{1}{E_{11}}$	$-\frac{\upsilon_{21}}{E_{22}}$	$-\frac{\upsilon_{31}}{E_{33}}$	0	0	0
$\boldsymbol{i = 2}$	$-\frac{\upsilon_{12}}{E_{11}}$	$\frac{1}{E_{22}}$	$-\frac{\upsilon_{32}}{E_{33}}$	0	0	0
$\boldsymbol{i = 3}$	$-\frac{\upsilon_{13}}{E_{11}}$	$-\frac{\upsilon_{23}}{E_{22}}$	$\frac{1}{E_{33}}$	0	0	0
$\boldsymbol{i = 4}$	0	0	0	$\frac{1}{G_{23}}$	0	0
$\boldsymbol{i = 5}$	0	0	0	0	$\frac{1}{G_{13}}$	0
$\boldsymbol{i = 6}$	0	0	0	0	0	$\frac{1}{G_{12}}$

After the determination of the compliance matrixes of all the regions ([Ssolid]; [Sinfill]; [Sshell]; and [Sfiber]), the next step can be taken. A coordinate system transformation is applied to the solid and infill regions due to the fact that these are printed, as mentioned above, in an alternate orientation between ±45° from the longitudinal axis. The solid and infill regions of the test specimen are transformed using the rotation matrix, [T] (Table 12). The new compliance matrix [Sxyz] relative to the global specimen coordinate system (shown in Figure 34) is determined for all solid and infill layers using Eq. (8).

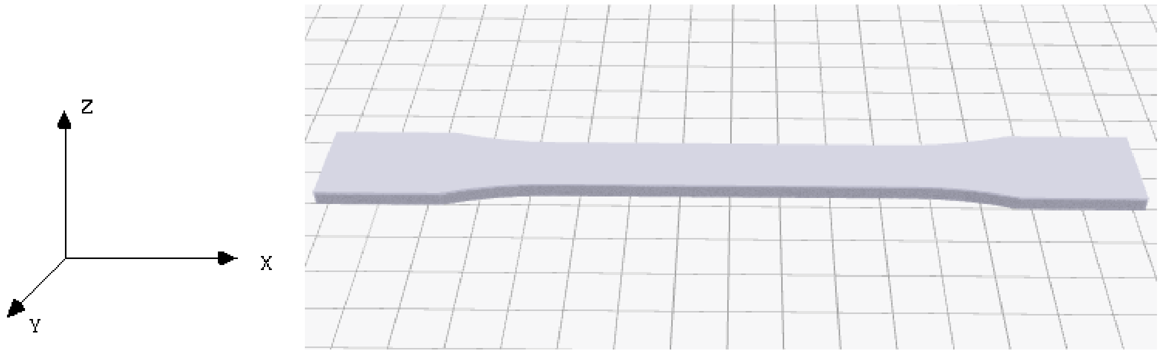

Figure 34 - Global coordinate system (xyz) orientation.

$$[S_{XYZ}] = [T]^T[S][T] \tag{8}$$

Table 12 - Elements of the transformation matrix [T]. In the notation of this paper, "i" denominates the number of the line and "j" denominates the number of the column. The c and s in this table are respectively, the cosine and sine of the angle "θ" (45°) between the deposition orientation of the region considered and the longitudinal axis [2][1][1][1][1].

T_{ij}	$j = 1$	$j = 2$	$j = 3$	$j = 4$	$j = 5$	$j = 6$
$i = 1$	c^2	s^2	0	0	0	$2cs$
$i = 2$	s^2	c^2	0	0	0	$-2cs$
$i = 3$	0	0	1	0	0	0
$i = 4$	0	0	0	c	s	0
$i = 5$	0	0	0	$-s$	c	0
$i = 6$	$-cs$	cs	0	0	0	$c^2 - s^2$

After the compliance matrix (with the orientation factor already addressed) for each component is determined, it can be inverted in order to obtain the respective stiffness matrix, [C]. The stiffness averaging is then performed by determining the volume fraction of each section within the test specimen in order to determine the contribution of each section to the overall mechanical properties.

The volume fraction of each component of the test specimen was determined from the geometry of the sample. The dimensions of the individual components within the test specimen are summarized in Table 13. These variables were used to calculate the volume (in mm^3) of each element using Eq. (9)-(15).

Table 13 - Specimen geometric variables.

Sample geometry variable	**Value**
Length of the narrow section (LN) [mm]	57
Width of the narrow section (W) [mm]	13
Thickness of the narrow section (T) [mm]	3.2
Layer thickness (T_{layer}) [mm]	0.1
Width of each reinforcement fiber (W_{fiber}) [mm]	0.7
Width of each shell (W_{shell}) [mm]	0.8
Number of fiber reinforced layers (N_{fiber}) (half of these layers are distributed right above the floor set of layers and the remaining half is located directly below the ceiling group of layers.	6
Number of fiber concentric rings ($N_{concentric}$)	0; 2; 4; 5
Number of floor layers (N_{floor}) ("solid" layers on the bottom of the specimen)	4
Number of ceiling layers ($N_{ceiling}$) ("solid" layers on the top of the specimen)	4
Number of solid layers ($N_{solid-m}$) (number of solid layers that are in between the floor and ceiling layers, they are usually printed to improve matrix-fiber interface)	8
Number of infill layers ($N_{infill-m}$) (number of infill layers, not including the infill layers located in the fiber reinforced layers)	10 for 2R, 4R and 5R specimens 24 (for pure Nylon specimen)

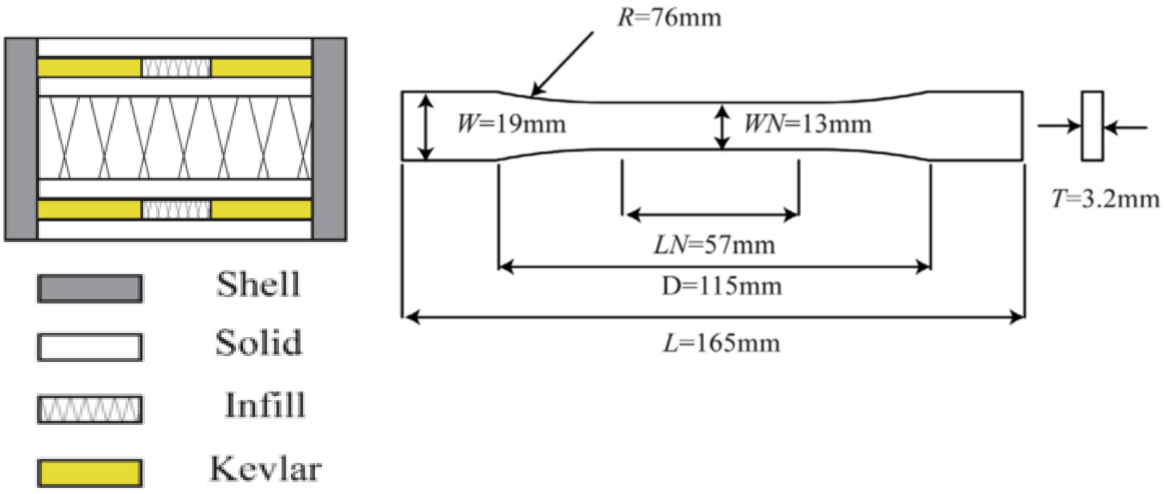

Figure 35 - Internal structure (left) and external dimensions (right) of the printed specimens. These schematics are used to assist the reader in the understanding of the expressions used to calculate the volume of each region (adapted from [2]).

The total volume of the resistant section of the sample ($V_{tensile}$) is calculated from:

$$V_{tensile} = L_N . W . T \tag{9}$$

The floor volume (V_{floor}) is determined from:

$$V_{floor} = [W - (2. W_{shell})]. L_N . T_{layer} . N_{floor} \tag{10}$$

Similarly, the ceiling volume ($V_{ceiling}$) is obtained from:

$$V_{ceiling} = [W - (2. W_{shell})]. L_N . T_{layer} . N_{ceiling} \tag{11}$$

The solid volume ($V_{solid\text{-}m}$) is given by:

$$V_{solid-m} = [W - (2. W_{shell})]. L_N . T_{layer} . N_{solid} \tag{12}$$

The infill volume ($V_{infill\text{-}m}$) is found by:

$$V_{infill-m} = [W - (2. W_{shell})]. L_N . T_{layer} . N_{infill} \tag*{(12)}$$

The fiber volume (V_{fiber}) is given by:

$$V_{fiber} = W_{fiber} . L_N . T_{layer} . 2N_{concentric} . N_{fiber} \tag{13}$$

The infill volume in the fiber reinforced layers ($V_{infill\text{-}fiber}$) is given by:

$$V_{infill-fiber} = \left[W - (2. W_{shell}) - (2. N_{concentric} . W_{fiber}\right]. L_N . T_{layer} . N_{fiber} \tag{14}$$

Finally, the shell region volume (V_{shell}) can be determined by:

$$V_{shell} = 2. W_{shell} . L_N . T \tag{15}$$

The volume fraction (Vf) of each section of the test specimen is calculated by dividing each of these region volumes by the total volume of the resistant section of the sample (Vtensile).

The stiffness averaging equation used to predict the mechanical properties of the test specimens is shown in (16), and calculates the “global” stiffness matrix of the fiber reinforced specimens. This equation shows that the contribution of the infill, shell, solid and Kevlar fiber regions are taken into account in order to determine the effective properties of the fiber reinforced 3D printed test specimen.

$$[C]^G = V_{f-shell}[C_{shell}] + V_{f-infill(+\theta)}[C_{infill+\theta}] + V_{f-infill(-\theta)}[C_{infill-\theta}] \\ + V_{f-solid(+\theta)}[C_{solid+\theta}] + V_{f-solid(-\theta)}[C_{solid-\theta}] + V_{f-fiber}[C_{fiber}] \quad (16)$$

In this equation the +θ and –θ notation refers to the volume fraction of the region that is oriented in the +θ and –θ with respect to the longitudinal axis of the specimen.

It is also important to mention that in Eq. (16):

$$V_{f-infill(+\theta)} = V_{f-infill-m(+\theta)} + V_{f-infill-fiber(+\theta)} \quad (17)$$

$$V_{f-infill(-\theta)} = V_{f-infill-m(-\theta)} + V_{f-infill-fiber(-\theta)} \quad (18)$$

$$V_{f-solid(+\theta)} = V_{f-solid-m(+\theta)} + V_{f-floor(+\theta)} + V_{f-ceiling(+\theta)} \quad (19)$$

$$V_{f-solid(-\theta)} = V_{f-solid-m(-\theta)} + V_{f-floor(-\theta)} + V_{f-ceiling(-\theta)} \quad (20)$$

To determine the effective mechanical properties of the fiber reinforced 3D printed parts the global stiffness matrix $[C]^G$ is inverted and the global compliance matrix $[S]^G$ is obtained. Once the global compliance matrix $[S]^G$ is known the effective elastic constants of the FDM printed carbon reinforced specimens can be calculated with Eq. (21).

$$E_x = \frac{1}{s_{11}^g} \quad E_y = \frac{1}{s_{22}^g} \quad E_z = \frac{1}{s_{33}^g}$$

$$G_{xy} = \frac{1}{s_{66}^g} \quad G_{yz} = \frac{1}{s_{44}^g} \quad G_{xz} = \frac{1}{s_{55}^g} \quad (21)$$

$$\upsilon_{xy} = -\frac{s_{12}^g}{s_{11}^g} \quad \upsilon_{zx} = -\frac{s_{13}^g}{s_{33}^g} \quad \upsilon_{yz} = -\frac{s_{23}^g}{s_{22}^g}$$

4 Results

4.1 Mechanical testing results

Mechanical testing was performed on the four sample configurations (0R, 2R, 4R and 5R) to see the effect of the fiber reinforcement on the mechanical properties of the printed specimens and to obtain comparable results with the results predicted from the model. The resulting stress-strain diagrams for the four sample configurations are shown in Figure 36.

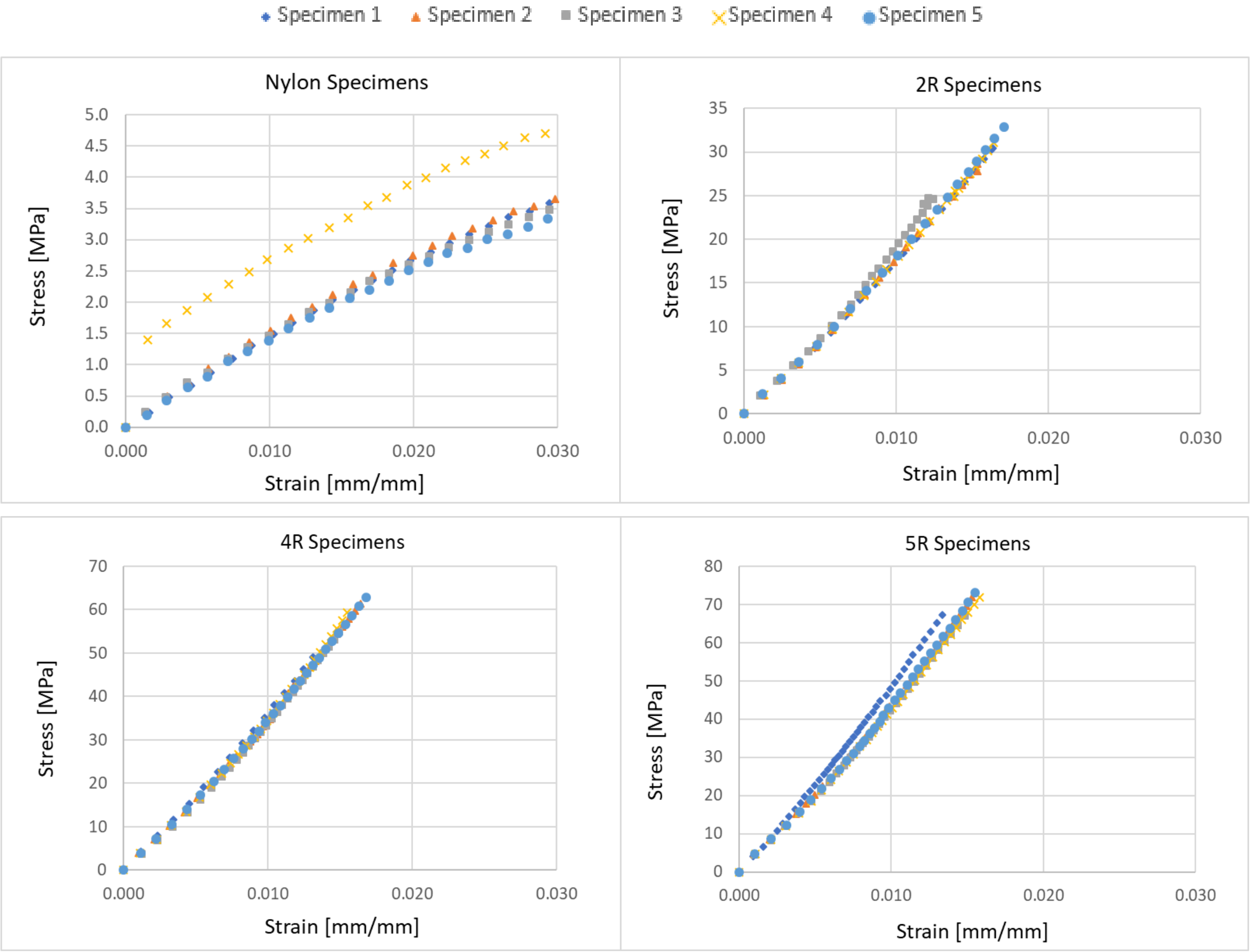

Figure 36 - Stress-strain diagrams for the four tested specimen configurations: 0R, 2R, 4R and 5R specimens.

The elastic modulus of each sample configurations was determined from the test results and were calculated dividing the stress difference between two points with two corresponding strains, according to ASTM D638-14 specifications. The points selected were at 0,0040 mm/mm strain and 0,0070 mm/mm strain, because the initial segment doesn't correctly represent a property of the material. According to ASTM D638-14, it is an artifact caused by a takeup of slack and alignment of the specimen. The ultimate tensile stress and percent elongation were also determined as dictated by ASTM D638-14 and the results are displayed in Table 14. In Figure 37, experimentally determined values for the elastic modulus and ultimate tensile strength are shown for each specimen configuration (with error bars and a 95% confidence interval).

Table 14 - Experimental test mean values of longitudinal elastic modulus, ultimate tensile strength and elongation at break for all specimen configurations with the respective standard deviations in parenthesis.

Properties of specimens (***standard deviation***)	$\boldsymbol{0R}$	$\boldsymbol{2R}$	$\boldsymbol{4R}$	$\boldsymbol{5R}$
$\boldsymbol{E_x}$ [$\boldsymbol{GPa}$]	0.15 (0.006)	1.85 (0.059)	3.56 (0.057)	4.41 (0.248)
Difference relative to nylon only specimen (%)	---	1133.33	2273.33	2840.00
Ultimate tensile strenght [***MPa***]	9.56 (0.663)	30.13 (3.046)	58.80 (5.404)	71.29 (2.733)
Difference relative to nylon only specimen (%)	---	215.17	515.06	645.71
Elongation at break (%)	76.21 (1.407)	1.57 (0.196)	1.56 (0.139)	1.52 (0.097)

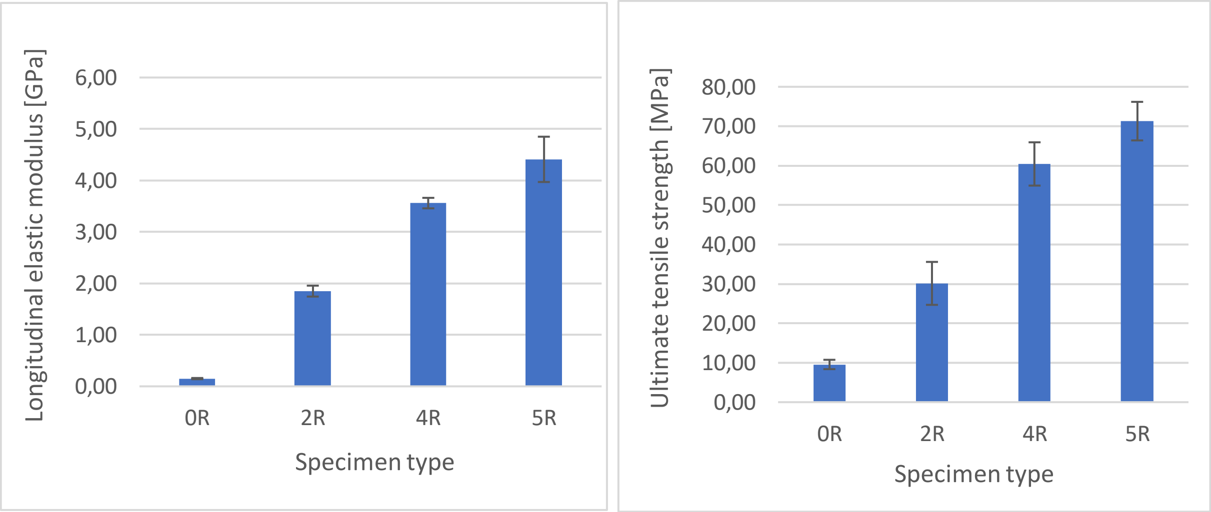

Figure 37 - Experimental values of the longitudinal elastic modulus (left) and ultimate tensile strength (right) for each specimen configuration with respective error bars. A 95% confidence level was used.

These results demonstrate that an increase in fiber reinforcement volume fraction results in increased elastic modulus and ultimate tensile strength of the printed specimens. They also show a great difference between the results of the elastic modulus and ultimate tensile strength for the reinforced specimens, and the same results for the nylon only specimen. Table 14 also shows that with the increase in fiber reinforcement, the elongation at break is greatly reduced when compared with the unreinforced specimens.

The relatively low standard deviation shows that the effect of the relative position of the specimens on the build platform is not significant in the mechanical properties of the produced specimens.

4.2 Volume average stiffness results

In this subsection the method described in subsection 3.4.1, is applied to the printed specimens, the results of the calculations are exposed and some clarifications are added along the process.

The first step of the method is to use the micromechanical model developed by Rodriguez et. al [1] to determine the effective properties of each FDM printed component. Taking into account the elastic properties of exposed in Table 9, and substituting them in Eq. (2)-(7) gives the results shown below, in Table 15, for the regions made of nylon: shell; infill; and solid regions.

The constants used for the fiber reinforcement region are the ones in Table 10 and were not calculated using Eq. (2)-(7), but were instead taken from [129] due to two reasons. The first is the fact that the Poisson's ratio for the fiber reinforcement is not given by the manufacturer and Eq. (1) needs Poisson's ratio to compute the shear modulus (G), which is also not provided by the manufacturer. The second reason is that these were the same values assumed in [2].

Table 15 - Calculated values of the mechanical properties of each constituent of the fiber reinforced 3D printed specimen. Here, the same properties are obtained for the Solid and Shell regions because they are assumed to have same values of void density (10%) and are both made of nylon. The infill region, as mentioned above, is considered to have a void density of 90%.

Property	**Region**		
	Solid/Shell	**Infill**	**Kevlar**
$\boldsymbol{E_{11}}$ $[\boldsymbol{GPa}]$	0.846	0.094	79.8
$\boldsymbol{E_{22} = E_{33}}$ $[\boldsymbol{GPa}]$	0.643	0.048	2.59
$\boldsymbol{G_{12} = G_{13}}$ $[\boldsymbol{GPa}]$	0.135	0.012	2.1
$\boldsymbol{G_{23}}$ $[\boldsymbol{GPa}]$	0.238	0.018	1.5
$\boldsymbol{v_{12} = v_{13}}$	0.315	0.035	0.33
$\boldsymbol{v_{21} = v_{31} = v_{32} = v_{23}}$	0.239	0.018	0.1

When looking at Table 15, it is important to notice that the Kevlar region properties are considerably higher than the rest of the regions, and therefore, a greater contribution in the overall mechanical properties of the 3D printed fiber reinforced specimens is expected from this region than the rest of the regions.

Using the data from Table 15, the compliance matrix of each region can be determined using Table 11, and is shown in Table 16.

Table 16 - Calculated compliance matrixes for the solid, shell, infill and Kevlar regions. The solid and shell regions have the same fill densities, and therefore, the same values in the compliance matrix.

$S_{ij}\ solid/shell$	$j = 1$	$j = 2$	$j = 3$	$j = 4$	$j = 5$	$j = 6$
$i = 1$	1.1820	-0.3723	-0.3723	0.0000	0.0000	0.0000
$i = 2$	-0.3723	1.5558	-0.3723	0.0000	0.0000	0.0000
$i = 3$	-0.3723	-0.3723	1.5558	0.0000	0.0000	0.0000
$i = 4$	0.0000	0.0000	0.0000	4.2007	0.0000	0.0000
$i = 5$	0.0000	0.0000	0.0000	0.0000	7.3922	0.0000
$i = 6$	0.0000	0.0000	0.0000	0.0000	0.0000	7.3922

$S_{ij}\ infill$	$j = 1$	$j = 2$	$j = 3$	$j = 4$	$j = 5$	$j = 6$
$i = 1$	10.6383	-0.3723	-0.3723	0.0000	0.0000	0.0000
$i = 2$	-0.3723	20.7307	-0.3723	0.0000	0.0000	0.0000
$i = 3$	-0.3723	-0.3723	20.7307	0.0000	0.0000	0.0000
$i = 4$	0.0000	0.0000	0.0000	55.9728	0.0000	0.0000
$i = 5$	0.0000	0.0000	0.0000	0.0000	84.6962	0.0000
$i = 6$	0.0000	0.0000	0.0000	0.0000	0.0000	84.6962

$S_{ij}\ fiber$	$j = 1$	$j = 2$	$j = 3$	$j = 4$	$j = 5$	$j = 6$
$i = 1$	0.0125	-0.0041	-0.0041	0.0000	0.0000	0.0000
$i = 2$	-0.0041	0.3861	-0.0386	0.0000	0.0000	0.0000
$i = 3$	-0.0041	-0.0386	0.3861	0.0000	0.0000	0.0000
$i = 4$	0.0000	0.0000	0.0000	0.6667	0.0000	0.0000
$i = 5$	0.0000	0.0000	0.0000	0.0000	0.4762	0.0000
$i = 6$	0.0000	0.0000	0.0000	0.0000	0.0000	0.4762

After this stage, it is necessary to perform the coordinate system transformation on the compliance matrixes of the infill and shell regions. The transformation matrix can be observed below for $\theta = \pm 45^{\circ}$, in Table 17.

Table 17 - Elements of the transformation matrix used for the infill and solid regions for θ = ±45°.

T_{ij} (θ = +45°)	$j = 1$	$j = 2$	$j = 3$	$j = 4$	$j = 5$	$j = 6$
$i = 1$	0.5000	0.5000	0.0000	0.0000	0.0000	1.0000
$i = 2$	0.5000	0.5000	0.0000	0.0000	0.0000	-1.0000
$i = 3$	0.0000	0.0000	1.0000	0.0000	0.0000	0.0000
$i = 4$	0.0000	0.0000	0.0000	0.7071	0.7071	0.0000
$i = 5$	0.0000	0.0000	0.0000	-0.7071	0.7071	0.0000
$i = 6$	-0.5000	0.5000	0.0000	0.0000	0.0000	0.0000

T_{ij} (θ = -45°)	$j = 1$	$j = 2$	$j = 3$	$j = 4$	$j = 5$	$j = 6$
$i = 1$	0.5000	0.5000	0.0000	0.0000	0.0000	-1.0000
$i = 2$	0.5000	0.5000	0.0000	0.0000	0.0000	1.0000
$i = 3$	0.0000	0.0000	1.0000	0.0000	0.0000	0.0000
$i = 4$	0.0000	0.0000	0.0000	0.7071	-0.7071	0.0000
$i = 5$	0.0000	0.0000	0.0000	0.7071	0.7071	0.0000
$i = 6$	0.5000	-0.5000	0.0000	0.0000	0.0000	0.0000

Using Eq. (8), the result of the compliance matrix of the infill and solid layers relative to the global specimen coordinate system is easily obtained and is shown in Table 18.

Table 18 - Solid and infill compliance matrixes relative to the global specimen coordinate system.

θ	45°					
S_{ij} $solid$ $(+\theta)$	$j = 1$	$j = 2$	$j = 3$	$j = 4$	$j = 5$	$j = 6$
$i = 1$	2.3463	-1.3498	-0.3723	0.0000	0.0000	-0.1869
$i = 2$	-1.3498	2.3463	-0.3723	0.0000	0.0000	-0.1869
$i = 3$	-0.3723	-0.3723	1.5558	0.0000	0.0000	0.0000
$i = 4$	0.0000	0.0000	0.0000	5.7965	-1.5957	0.0000
$i = 5$	0.0000	0.0000	0.0000	-1.5957	5.7965	0.0000
$i = 6$	-0.1869	-0.1869	0.0000	0.0000	0.0000	3.4825

θ	45°					
$S_{ij}\ solid\ (-\theta)$	$j = 1$	$j = 2$	$j = 3$	$j = 4$	$j = 5$	$j = 6$
$i = 1$	2.3463	-1.3498	-0.3723	0.0000	0.0000	0.1869
$i = 2$	-1.3498	2.3463	-0.3723	0.0000	0.0000	0.1869
$i = 3$	-0.3723	-0.3723	1.5558	0.0000	0.0000	0.0000
$i = 4$	0.0000	0.0000	0.0000	5.7965	1.5957	0.0000
$i = 5$	0.0000	0.0000	0.0000	1.5957	5.7965	0.0000
$i = 6$	0.1869	0.1869	0.0000	0.0000	0.0000	3.4825

θ	45°					
$S_{ij}\ infill\ (+\theta)$	$j = 1$	$j = 2$	$j = 3$	$j = 4$	$j = 5$	$j = 6$
$i = 1$	28.8301	-13.5180	-0.3723	0.0000	0.0000	-5.0462
$i = 2$	-13.5180	28.8301	-0.3723	0.0000	0.0000	-5.0462
$i = 3$	-0.3723	-0.3723	20.7307	0.0000	0.0000	0.0000
$i = 4$	0.0000	0.0000	0.0000	70.3345	-14.3617	0.0000
$i = 5$	0.0000	0.0000	0.0000	-14.3617	70.3345	0.0000
$i = 6$	-5.0462	-5.0462	0.0000	0.0000	0.0000	32.1137

θ	45°					
$S_{ij}\ infill\ (-\theta)$	$j = 1$	$j = 2$	$j = 3$	$j = 4$	$j = 5$	$j = 6$
$i = 1$	28.8301	-13.5180	-0.3723	0.0000	0.0000	5.0462
$i = 2$	-13.5180	28.8301	-0.3723	0.0000	0.0000	5.0462
$i = 3$	-0.3723	-0.3723	20.7307	0.0000	0.0000	0.0000
$i = 4$	0.0000	0.0000	0.0000	70.3345	14.3617	0.0000
$i = 5$	0.0000	0.0000	0.0000	14.3617	70.3345	0.0000
$i = 6$	5.0462	5.0462	0.0000	0.0000	0.0000	32.1137

It is now possible to obtain the stiffness matrixes of each region relative to the global specimen coordinate system by inverting their respective compliance matrixes. They are displayed in Table 19.

Table 19 - Calculated stiffness matrixes of all the regions of the 3D printed specimen.

$\boldsymbol{C_{ij}\ solid\ (+\theta)}$	$\boldsymbol{j=1}$	$\boldsymbol{j=2}$	$\boldsymbol{j=3}$	$\boldsymbol{j=4}$	$\boldsymbol{j=5}$	$\boldsymbol{j=6}$
$\boldsymbol{i=1}$	0.7616	0.4910	0.2998	0.0000	0.0000	0.0672
$\boldsymbol{i=2}$	0.4910	0.7616	0.2998	0.0000	0.0000	0.0672
$\boldsymbol{i=3}$	0.2998	0.2998	0.7862	0.0000	0.0000	0.0322
$\boldsymbol{i=4}$	0.0000	0.0000	0.0000	0.1867	0.0514	0.0000
$\boldsymbol{i=5}$	0.0000	0.0000	0.0000	0.0514	0.1867	0.0000
$\boldsymbol{i=6}$	0.0672	0.0672	0.0322	0.0000	0.0000	0.2944

$\boldsymbol{C_{ij}\ solid\ (-\theta)}$	$\boldsymbol{j=1}$	$\boldsymbol{j=2}$	$\boldsymbol{j=3}$	$\boldsymbol{j=4}$	$\boldsymbol{j=5}$	$\boldsymbol{j=6}$
$\boldsymbol{i=1}$	0.7616	0.4910	0.2998	0.0000	0.0000	-0.0672
$\boldsymbol{i=2}$	0.4910	0.7616	0.2998	0.0000	0.0000	-0.0672
$\boldsymbol{i=3}$	0.2998	0.2998	0.7862	0.0000	0.0000	-0.0322
$\boldsymbol{i=4}$	0.0000	0.0000	0.0000	0.1867	-0.0514	0.0000
$\boldsymbol{i=5}$	0.0000	0.0000	0.0000	-0.0514	0.1867	0.0000
$\boldsymbol{i=6}$	-0.0672	-0.0672	-0.0322	0.0000	0.0000	0.2944

$\boldsymbol{C_{ij}\ infill\ (+\theta)}$	$\boldsymbol{j=1}$	$\boldsymbol{j=2}$	$\boldsymbol{j=3}$	$\boldsymbol{j=4}$	$\boldsymbol{j=5}$	$\boldsymbol{j=6}$
$\boldsymbol{i=1}$	0.0483	0.0247	0.0013	0.0000	0.0000	0.0115
$\boldsymbol{i=2}$	0.0247	0.0483	0.0013	0.0000	0.0000	0.0115
$\boldsymbol{i=3}$	0.0013	0.0013	0.0483	0.0000	0.0000	0.0004
$\boldsymbol{i=4}$	0.0000	0.0000	0.0000	0.0148	0.0030	0.0000
$\boldsymbol{i=5}$	0.0000	0.0000	0.0000	0.0030	0.0148	0.0000
$\boldsymbol{i=6}$	0.0115	0.0115	0.0004	0.0000	0.0000	0.0347

$\boldsymbol{C_{ij}\ infill\ (-\theta)}$	$\boldsymbol{j=1}$	$\boldsymbol{j=2}$	$\boldsymbol{j=3}$	$\boldsymbol{j=4}$	$\boldsymbol{j=5}$	$\boldsymbol{j=6}$
$\boldsymbol{i=1}$	0.0483	0.0247	0.0013	0.0000	0.0000	-0.0115
$\boldsymbol{i=2}$	0.0247	0.0483	0.0013	0.0000	0.0000	-0.0115
$\boldsymbol{i=3}$	0.0013	0.0013	0.0483	0.0000	0.0000	-0.0004
$\boldsymbol{i=4}$	0.0000	0.0000	0.0000	0.0148	-0.0030	0.0000
$\boldsymbol{i=5}$	0.0000	0.0000	0.0000	-0.0030	0.0148	0.0000
$\boldsymbol{i=6}$	-0.0115	-0.0115	-0.0004	0.0000	0.0000	0.0347

C_{ij} **shell**	$j=1$	$j=2$	$j=3$	$j=4$	$j=5$	$j=6$
$i=1$	1.0551	0.3320	0.3320	0.0000	0.0000	0.0000
$i=2$	0.3320	0.7862	0.2676	0.0000	0.0000	0.0000
$i=3$	0.3320	0.2676	0.7862	0.0000	0.0000	0.0000
$i=4$	0.0000	0.0000	0.0000	0.2381	0.0000	0.0000
$i=5$	0.0000	0.0000	0.0000	0.0000	0.1353	0.0000
$i=6$	0.0000	0.0000	0.0000	0.0000	0.0000	0.1353

C_{ij} **fiber**	$j=1$	$j=2$	$j=3$	$j=4$	$j=5$	$j=6$
$i=1$	80.4317	0.9572	0.9572	0.0000	0.0000	0.0000
$i=2$	0.9572	2.6276	0.2730	0.0000	0.0000	0.0000
$i=3$	0.9572	0.2730	2.6276	0.0000	0.0000	0.0000
$i=4$	0.0000	0.0000	0.0000	1.5000	0.0000	0.0000
$i=5$	0.0000	0.0000	0.0000	0.0000	2.1000	0.0000
$i=6$	0.0000	0.0000	0.0000	0.0000	0.0000	2.1000

To compute Eq. (16), it is necessary to determine the volume fractions of each of the regions for all the various types of specimens produced: Nylon only; 2R; 4R; and 5R. Knowing that the deposition orientation of the infill and solid regions is alternated between ±45°, and that the number of layers that contain these regions is even, it is legitimate to assume that the number of layers deposited with orientation +45° and with orientation -45° is the same, and therefore, for this specimens:

$$\boldsymbol{V}_{\boldsymbol{solid}\,(+\boldsymbol{\theta})} = \boldsymbol{V}_{\boldsymbol{solid}\,(-\boldsymbol{\theta})} \tag{22}$$

$$\boldsymbol{V}_{\boldsymbol{infill}\,(+\boldsymbol{\theta})} = \boldsymbol{V}_{\boldsymbol{infill}\,(-\boldsymbol{\theta})} \tag{23}$$

Which means that

$$\boldsymbol{V}_{\boldsymbol{f-solid}\,(+\boldsymbol{\theta})} = \boldsymbol{V}_{\boldsymbol{f-solid}\,(-\boldsymbol{\theta})} \tag{24}$$

$$\boldsymbol{V}_{\boldsymbol{f-infill}\,(+\boldsymbol{\theta})} = \boldsymbol{V}_{\boldsymbol{f-infill}\,(-\boldsymbol{\theta})} \tag{25}$$

Having this in mind a detailed list of each region’s volume fractions for the various type of printed specimens can be examined below in Table 20.

Table 20 - Calculated values of the necessary volumes for the determination of the global stiffness matrix of all the types of specimens. 0R means nylon only specimens, 2R (2 concentric rings reinforcement), 4R (4 concentric rings of reinforcement) and 5R (5 concentric rings of reinforcement).

$\boldsymbol{Volume}\ [\boldsymbol{mm^3}]$ $(\boldsymbol{volume\ fractions})$	$\boldsymbol{0R}$	$\boldsymbol{2R}$	$\boldsymbol{4R}$	$\boldsymbol{5R}$
$\boldsymbol{V_{tensile}}$	2371.2000 **(1.0000)**	2371.2000 **(1.0000)**	2371.2000 **(1.0000)**	2371.2000 **(1.0000)**
$\boldsymbol{V_{floor(+\theta)}}$	129.9600 **(0.0548)**	129.9600 (0.0548)	129.9600 **(0.0548)**	129.9600 **(0.0548)**
$\boldsymbol{V_{floor(-\theta)}}$	129.9600 **(0.0548)**	129.9600 **(0.0548)**	129.9600 **(0.0548)**	129.9600 **(0.0548)**
$\boldsymbol{V_{ceiling(+\theta)}}$	129.9600 **(0.0548)**	129.9600 **(0.0548)**	129.9600 **(0.0548)**	129.9600 **(0.0548)**
$\boldsymbol{V_{ceiling(-\theta)}}$	129.9600 **(0.0548)**	129.9600 **(0.0548)**	129.9600 **(0.0548)**	129.9600 **(0.0548)**
$\boldsymbol{V_{solid-m(+\theta)}}$	0.0000 **(0.0000)**	259.9200 **(0.1096)**	259.9200 **(0.1096)**	259.9200 **(0.1096)**
$\boldsymbol{V_{solid-m(-\theta)}}$	0.0000 **(0.0000)**	259.9200 **(0.1096)**	259.9200 **(0.1096)**	259.9200 **(0.1096)**
$\boldsymbol{V_{infill-m(+\theta)}}$	779.7600 **(0.3288)**	324.9000 **(0.1370)**	324.9000 **(0.1370)**	324.9000 **(0.1370)**
$\boldsymbol{V_{infill-m(-\theta)}}$	779.7600 **(0.3288)**	324.9000 **(0.1370)**	324.9000 **(0.1370)**	324.9000 **(0.1370)**
$\boldsymbol{V_{infill-fiber(+\theta)}}$	0.0000 **(0.0000)**	147.0600 **(0.0620)**	99.1800 **(0.0418)**	75.2400 **(0.0317)**
$\boldsymbol{V_{infill-fiber(-\theta)}}$	0.0000 **(0.0000)**	147.0600 **(0.0620)**	99.1800 **(0.0418)**	75.2400 **(0.0317)**
$\boldsymbol{V_{shell}}$	291.8400 **(0.1231)**	291.8400 **(0.1231)**	291.8400 **(0.1231)**	291.8400 **(0.1231)**
$\boldsymbol{V_{fiber}}$	0.0000 **(0.0000)**	95.7600 **(0.0404)**	191.5200 **(0.0808)**	239.4000 **(0.1010)**

At this point, Eq. (16) can be computed using Table 19 and Table 20. The results for the global stiffness matrix of all types of specimens are listed in Table 21.

Table 21 - Calculated global stiffness matrix for all printed types of specimens

$\left[C_{ij}\right]_{0R}^{G}$	$j = 1$	$j = 2$	$j = 3$	$j = 4$	$j = 5$	$j = 6$
$i = 1$	0.3286	0.1647	0.1074	0.0000	0.0000	0.0000
$i = 2$	0.1647	0.2955	0.0995	0.0000	0.0000	0.0000
$i = 3$	0.1074	0.0995	0.3009	0.0000	0.0000	0.0000
$i = 4$	0.0000	0.0000	0.0000	0.0800	0.0000	0.0000
$i = 5$	0.0000	0.0000	0.0000	0.0000	0.0673	0.0000
$i = 6$	0.0000	0.0000	0.0000	0.0000	0.0000	0.1040

$\left[C_{ij}\right]_{2R}^{G}$	$j = 1$	$j = 2$	$j = 3$	$j = 4$	$j = 5$	$j = 6$
$i = 1$	3.7312	0.3046	0.2115	0.0000	0.0000	0.0000
$i = 2$	0.3046	0.5560	0.1759	0.0000	0.0000	0.0000
$i = 3$	0.2115	0.1759	0.5668	0.0000	0.0000	0.0000
$i = 4$	0.0000	0.0000	0.0000	0.1776	0.0000	0.0000
$i = 5$	0.0000	0.0000	0.0000	0.0000	0.1892	0.0000
$i = 6$	0.0000	0.0000	0.0000	0.0000	0.0000	0.2444

$\left[C_{ij}\right]_{4R}^{G}$	$j = 1$	$j = 2$	$j = 3$	$j = 4$	$j = 5$	$j = 6$
$i = 1$	6.9775	0.3423	0.2501	0.0000	0.0000	0.0000
$i = 2$	0.3423	0.6602	0.1869	0.0000	0.0000	0.0000
$i = 3$	0.2501	0.1869	0.6710	0.0000	0.0000	0.0000
$i = 4$	0.0000	0.0000	0.0000	0.2376	0.0000	0.0000
$i = 5$	0.0000	0.0000	0.0000	0.0000	0.2734	0.0000
$i = 6$	0.0000	0.0000	0.0000	0.0000	0.0000	0.3278

$\left[C_{ij}\right]_{5R}^{G}$	$j = 1$	$j = 2$	$j = 3$	$j = 4$	$j = 5$	$j = 6$
$i = 1$	8.6006	0.3611	0.2694	0.0000	0.0000	0.0000
$i = 2$	0.3611	0.7123	0.1924	0.0000	0.0000	0.0000
$i = 3$	0.2694	0.1924	0.7231	0.0000	0.0000	0.0000
$i = 4$	0.0000	0.0000	0.0000	0.2676	0.0000	0.0000
$i = 5$	0.0000	0.0000	0.0000	0.0000	0.3155	0.0000
$i = 6$	0.0000	0.0000	0.0000	0.0000	0.0000	0.3695

Finally, inverting each of these matrixes and performing calculations, Eq. (21) gives the final properties of the specimens (Table 22).

Table 22 - Predicted elastic constants of each of the printed specimens using the Volume Average Stiffness method.

$\boldsymbol{Elastic\ constants}$	$\boldsymbol{0R}$	$\boldsymbol{2R}$	$\boldsymbol{4R}$	$\boldsymbol{5R}$
E_x $[GPa]$	0.2266	3.5384	6.7620	8.3735
E_y $[GPa]$	0.2051	0.4858	0.5973	0.6512
E_z $[GPa]$	0.2560	0.5075	0.6146	0.6676
G_{xy} $[GPa]$	0.1040	0.2444	0.3278	0.3695
G_{yz} $[GPa]$	0.0800	0.1776	0.2376	0.2676
G_{xz} $[GPa]$	0.0673	0.1892	0.2734	0.3155
υ_{xy}	0.4920	0.4766	0.4483	0.4378
υ_{zx}	0.2195	0.0323	0.0225	0.0204
υ_{yz}	0.1718	0.2860	0.2638	0.2534

5 Discussion and analysis

5.1 Mechanical testing

The tensile test results shown in section 4.1, reveal an increase in the stiffness values of fiber reinforced 3D printed components relative to Nylon only samples. This is expected because the Kevlar fibers have a much greater elastic modulus and ultimate tensile strength than Nylon. Therefore, the addition of Kevlar fibers results in an increase in the effective properties (elastic modulus and ultimate tensile strength) of the 3D printed samples, as expected.

The stress-strain curves in Figure 36 also demonstrate non-linear behavior for the fiber reinforced specimens. The non-linear behavior of the fiber reinforced 3D printed specimen is triggered by the Mark One Printer's manufacturing process [2]. In the course of part fabrication, Kevlar fibers are inserted into the test specimen in particular regions of the 3D printed part. During the fiber implanting process, the tension applied to the Kevlar strands is insufficient and as a result, in-plane fiber waviness (in the X-Y plane) occurs in the Kevlar strands, as shown in Figure 38. Another possible cause for the existing fiber waviness are possible thermal stresses developed during manufacture due to the microstructural variations in the coefficient of thermal expansion [131].

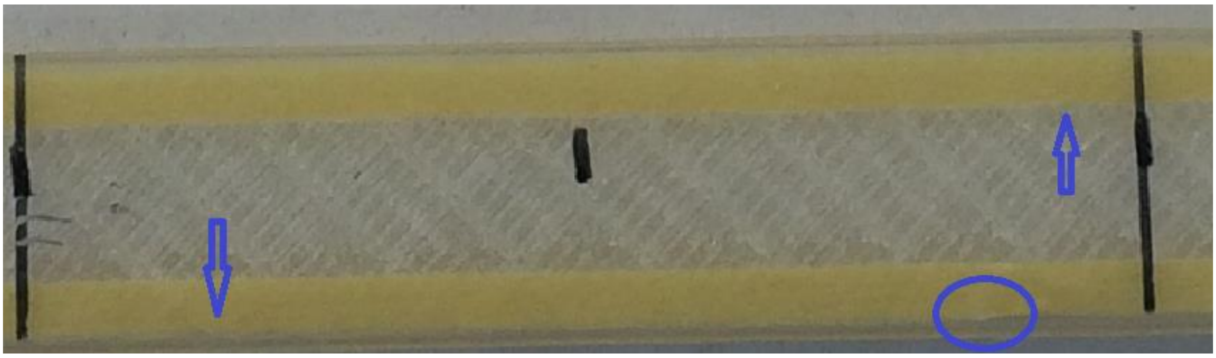

Figure 38 - Fiber waviness in the narrow section of the fiber reinforced 3D-printed specimens. It is visible that fibers are not perfectly aligned with the longitudinal axis of the test sample. These imperfections are present in all specimens but the specimen shown in the image is a 2R specimen.

Fiber waviness affects the mechanical properties of the 3D printed parts as the implanted fibers are not entirely aligned with the loading axis of the test samples. The effect of fiber waviness on the mechanical properties [132] and on nonlinear behaviors [133] of composite laminates has been demonstrated in the literature theoretically and experimentally. As the samples are loaded the embedded fibers begin to straighten due to the applied tensile load. This straightening of the embedded yarns clarifies the non-linear behavior of the samples shown in Figure 36. Additionally, the adhesive used to place the tabs in the specimens might contribute to this non-linear effect.

The sequence of tests was in the following order: first the 0R specimens, then the 2R samples, followed by the 4R and finally the 5R. The tests of the 0R specimens ran as expected, i.e., the specimens elongated until failure (in the narrow section), after reaching high levels of strain. However, in all fiber-reinforced test pieces, failure occurred in the shoulder region of the specimen while the rest of the sample remained intact, as can be seen in Figure 39.

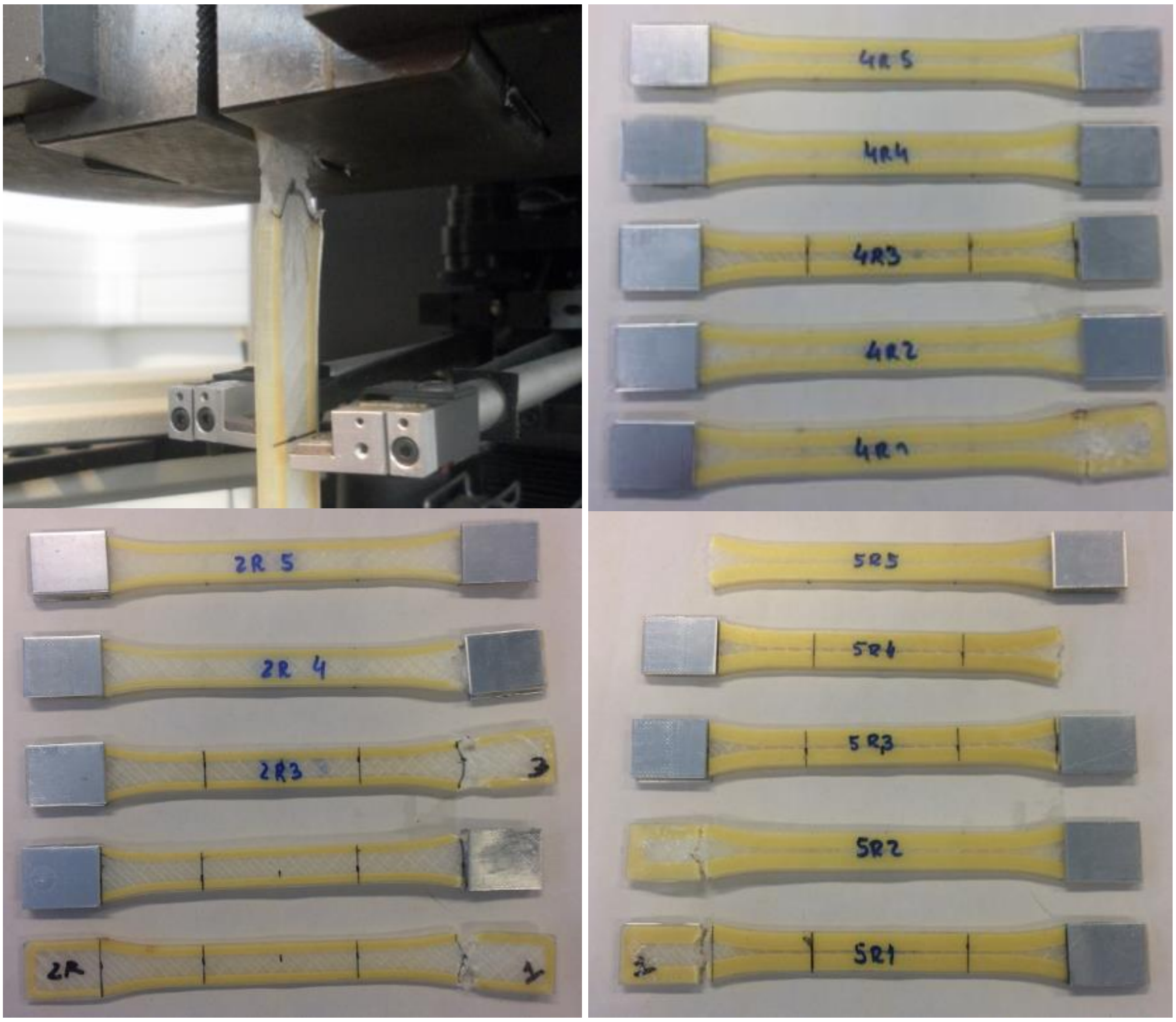

Figure 39 - Specimen failure location for the fiber reinforced specimens. The failure occurs at the shoulder region for all specimens. In the image, aluminum tabs can be seen. These tabs were placed (the adhesive used was cyanoacrylate) in the specimens after the test of the first 2R specimen to prevent failure in this region, as the failure was intended to happen in the narrow section region.

The failure location obtained in these specimens is coherent with the one described in [2] and in Kvalsvig et. al [125].

A suggested reason for the failure of the specimens in the shoulder region is made in [2]. The proposed reason for this problem is inherent (again) to the manufacture process. In Figure 40, the fiber placement path generated using the Eiger 3D printing software is shown. It can be observed that sample failure occurs at the same location where the fiber path begins for the sample. This local discontinuity, or non-uniformity is a great source of stress concentration. All geometries generated using the Mark One 3D printer will have a start (and end) location for the continuous fiber reinforcement. Figure 40 demonstrates that understanding the start location of the fiber reinforcement is critical for manufacturing functional components. When designing the fabrication of components using this method, the start location of the fiber reinforcement should be placed in a location under low loading in order to prevent premature failure due to the great stress concentration triggered by the fiber start location.

An important thing to be noticed is that in the shoulder area of the specimen, the fibers are not perfectly aligned with the loading axis (longitudinal axis of the specimen), and for that reason, not in a pure tension state [92]. This misalignment causes additional stress concentration in that region.

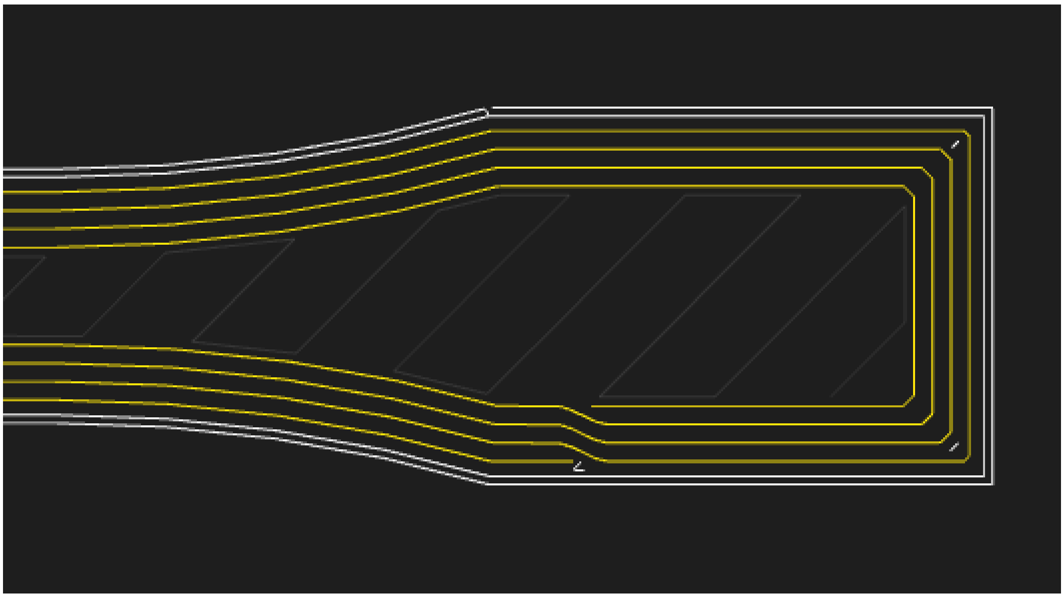

Figure 40 - Internal View of a fiber reinforced layer. In the image it can be seen that the start location of the fiber reinforcement is near the shoulder region of the specimens. This local discontinuity generates stress concentration in the gripping region of the part and is the main responsible for the specimen failure location.

Kvalsvig et. al [125], using the same geometry for the specimens (according to ASTM D638 Type I geometry) as the one in the printed and tested specimens in this work, found that premature failure was initiated by the crushing of the sample in the gripping region. This crushing inhibited the attainment of the true ultimate tensile strength. Specimens failed prematurely in the grippers region, making the results from the tensile test unreliable.

Therefore, adjustments were made to the specimens that did not alter the area being tested but rather the area inside the grippers. The first alteration was to create a hole on both ends of the specimen. These holes would have steel inserts placed inside that would have the same thickness as the specimens. The idea behind the steel inserts addition would be to reduce the chances of specimen’s premature failure due to crushing. A potential problem entailed with this solution, would be that the specimen would fail where the holes are closest to the outer wall. Which would also result in an unreliable tensile test.

A second modification was made to reduce the chance of specimens failing prematurely. Reduction of the number of right angles present in the specimen geometry. To reduce the number of right angles experienced by the continuous fiber placed in the specimen, the ends of the specimens were rounded. This aimed to reduce the stress concentration experienced in the corners of the specimen. Figure 41 shows the improved specimen design.

Figure 41 - Tensile test specimen design proposed in [125]. The geometry and dimensions of this test specimen are equal to the dimensions of the specimens produced in this work except the rounding in the ends of the specimen, and the holes for the steel inserts. This design aims to prevent failure in regions other than the narrow section, where pure tension conditions exist.

These modifications prevented specimens from failing prematurely due to crushing. However, the stress concentration caused by the steel inserts within the specimen's holes, led to premature failure as well. Specimens performed better without the steel inserts but still failed due to the crushing force of the grippers. The authors also suggested a thickening of the sections within the gripping region to alleviate this problem [125].

As can be seen, an effective design for tensile testing of 3D-printed fiber reinforced specimens is yet to be reached but, in summary, there are some guidelines:

- The discontinuities provoked by the start and end of the fiber reinforcement deposition paths are inherent to the process and cannot be removed. But they should be placed in the ends of the specimen, in a distributed manner along the XY plane for the different fiber reinforced layers, to avoid accumulation of stress concentrations in a single point in the XY plane. An example is shown below in Figure 42.

- The fiber in the shoulder region should be as aligned as possible with the loading axis (longitudinal axis) to avoid premature failures caused by multi-state stress.

- Crushing of the specimen in the gripping region should be avoided at all costs. However, if holes with steel inserts should be placed, they should be positioned as far as possible from the outer edges of the specimen in the gripping region as possible, to avoid premature failure due to stress concentrations.

- To reduce the number of right angles experienced by the continuous fiber placed in the specimen, the edges of the specimen should be curved. This aims to reduce the stress concentration existing due to specimen corners.

- The thickness values of the printed parts should be superior to the 3,20 mm (at least in the gripping region) to protect the fibers from the crushing forces of the grippers.

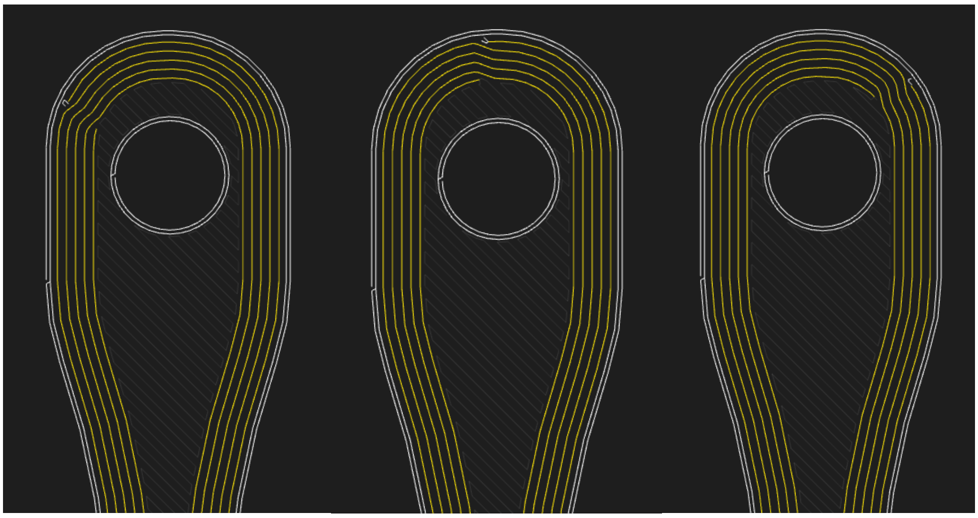

Figure 42 - Evenly spread start locations for the fiber reinforcement deposition paths throughout the fiber reinforced layers. This control can increase the tension the specimen resists and decrease chances of premature failure.

An example geometry that follows the former guidelines can be observed below in Figure 43.

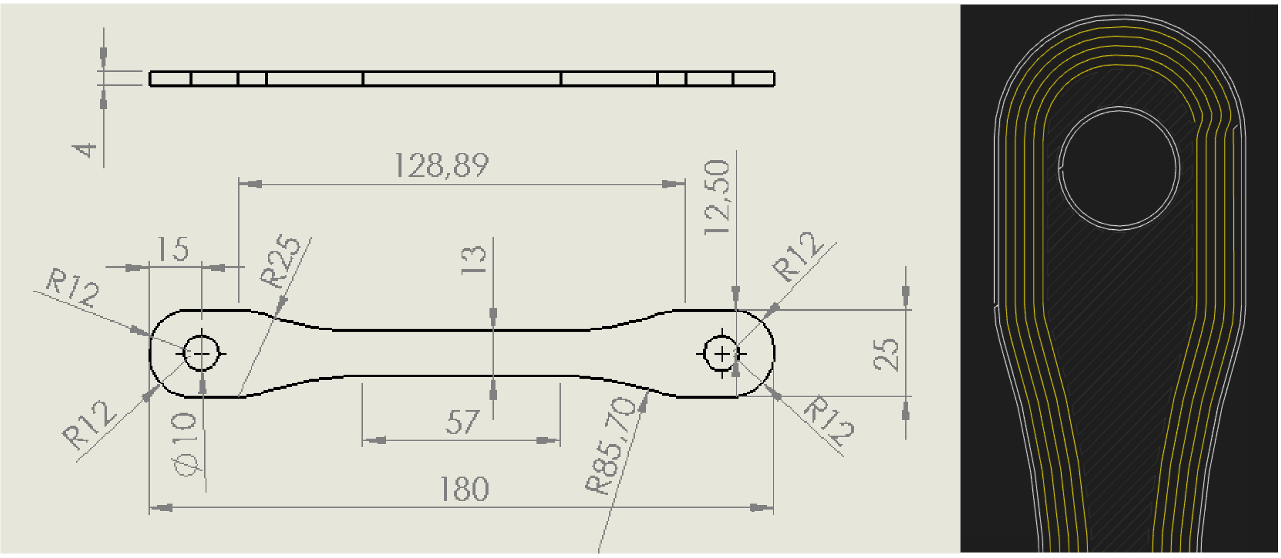

Figure 43 - Suggested geometry for the fiber reinforced 3D-printed tensile test specimens. This geometry and dimensions follow the guidelines listed above and the respective dimensions can be seen on the left. In the right, an Internal View of the specimen is presented.

In this geometry the radius of the curve that forms the shoulder region and total length of the specimen are increased relative to the printed specimen's geometry to make the fiber reinforcement more aligned with the loading axis in the shoulder region. And also to make the variation of width along this region smoother. Moreover, the right (or sharp) angles present in the printed specimens were removed to avoid unnecessary stress concentrations.

The thickness of the specimen was slightly increased to protect the fibers from the crushing forces present in the surface of the specimen in the gripping region.

For the 5R specimen, which is the maximum number of rings allowed for this geometry, the fiber reinforcement short distance to the hole can be problematic, however, this is in the worst case scenario.

The example shown is a suggestion, and as such, different locations and diameters for the holes can be tested and optimized. Removal of the holes can be tested as well, because although they prevent the premature failure of the specimen (supported by the steel inserts) due to crushing forces, they also cause stress concentration in the extremity region that can lead to failure in this zone.

5.2 Determination of the specific stiffness and specific strength of the 3D-printed fiber reinforced specimens

To evaluate the specific properties of the fiber reinforced specimens, and to compare them with other materials, the weight of the 3D-printed specimens was measured with a digital scale (2.5-300 ± 0.005 g) as shown in Figure 44. Three measurements were made to each specimen and average values were calculated for each fiber reinforced specimen. The results of these measurements are listed in Table 23.

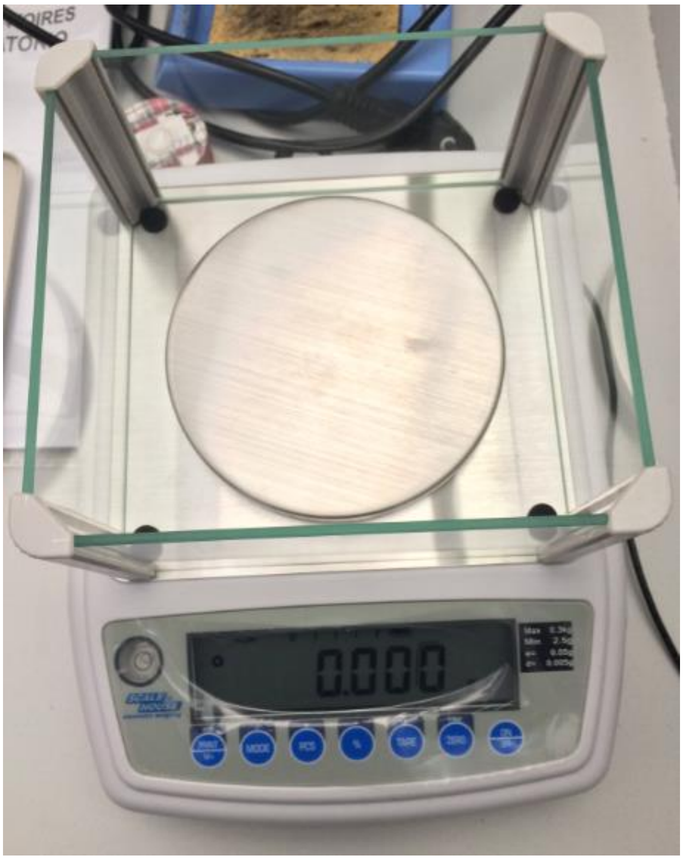

Figure 44 - Electronic scale used for the weighting of printed specimens. Three measurements were conducted for each specimen.

Table 23 - 3D-printed fiber reinforced specimen's weight measurement results. Three measurements were performed for each specimen and the mean values calculated.

5R Specimen	Measured Weight [g]			
	Measurement 1	Measurement 2	Measurement 3	Mean value
1	5.735	5.735	5.735	5.735
2	5.705	5.705	5.705	5.705
3	5.755	5.750	5.750	5.752
4	5.725	5.725	5.730	5.727
5	5.710	5.710	5.710	5.710

4R Specimen	Measured Weight [g]			
	Measurement 1	Measurement 2	Measurement 3	Mean value
1	5.625	5.625	5.625	5.625
2	5.535	5.530	5.530	5.532
3	5.590	5.585	5.590	5.588
4	5.565	5.565	5.565	5.565
5	5.590	5.565	5.590	5.582

2R Specimen	Measured Weight [g]			
	Measurement 1	Measurement 2	Measurement 3	Mean value
1	5.330	5.330	5.330	5.330
2	5.365	5.365	5.360	5.363
3	5.265	5.265	5.265	5.265
4	5.280	5.280	5.285	5.282
5	5.300	5.305	5.300	5.302

The results of the specimens' weight for each fiber reinforced sample configuration are better pictured in Table 24.

Table 24 – Summarized results of the measurements done for the fiber reinforced specimens. The mean measured weight of each fiber reinforced specimen is shown. The mean calculated values of the weight of each specimen configuration is shown as well as the standard deviation.

Measured Weight [g]	Specimen number						
Sample configuration	1	2	3	4	5	Mean value	Standard Deviation
2R	5.330	5.363	5.265	5.282	5.302	5.308	0.0391
4R	5.625	5.532	5.588	5.565	5.582	5.578	0.0341
5R	5.735	5.705	5.752	5.727	5.710	5.726	0.0190

As expected, with the increase of fiber reinforcement, the weight of the specimen also increases due to the higher density of the Kevlar fiber when compared to the Nylon filament.

With the weight of each fiber reinforced sample determined, the specific properties can be easily determined. First, it is necessary to determine the density of each specimen configuration. It is important to note that the volume occupied is constant for all specimen configurations. The only changes are occurring inside the specimen and therefore the density of the specimen is expected to increase as the quantity of fiber reinforcement increases.

After the density is determined, one only has to divide the elastic modulus and ultimate tensile strength obtained in the tensile test for the density to find the specific modulus and specific strength of the fiber reinforced 3D-printed samples. These results can be found in Table 25.

Table 25 - Results of the specific modulus and specific strength of the fiber reinforced 3D-printed specimens.

$\boldsymbol{Sample\ type}$	$\boldsymbol{Fiber\ volume\ fraction}$ [%]	$\boldsymbol{Mass}$ $[g]$	$\boldsymbol{Volume}$ $[mm^3]$	$\boldsymbol{Density}$ $\left[\frac{kg}{m^3}\right]$	$\boldsymbol{Specific\ modulus}$ $\left[\frac{MN.m}{kg}\right]$	$\boldsymbol{Specific\ strength}$ $\left[\frac{kN.m}{kg}\right]$
$\boldsymbol{2R}$	4.038	5.308	8029.088	661.138	2.798	45.573
$\boldsymbol{4R}$	8.077	5.578	8029.088	694.765	5.124	84.633
$\boldsymbol{5R}$	10.096	5.726	8029.088	713.115	6.184	99.970

Looking at Figure 45, it can be seen that the 3D-printed fiber reinforced samples, with relatively low fiber volume fractions, can exhibit similar specific properties than the ones of some metals and alloys. Additionally, one has to consider that the samples failed prematurely, which means that the specific strength of these specimens can reach even higher values.

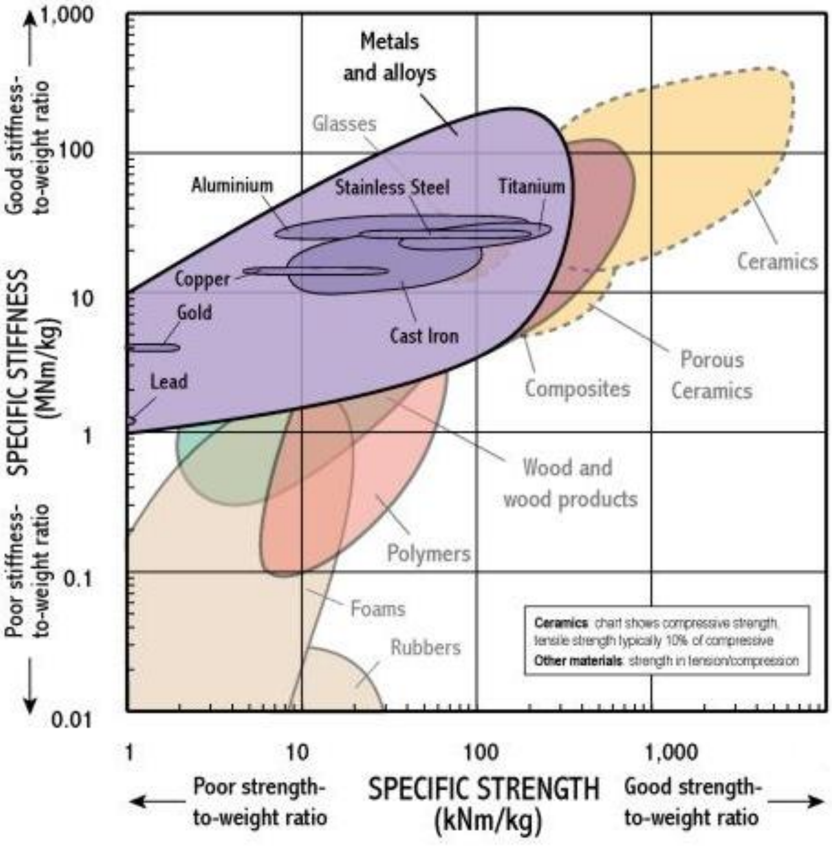

Figure 45 - Specific stiffness vs specific strength chart for different classes of materials [147].

5.3 Comparison of mechanical model results with experiments

As can be seen in section 4, the results of the experimental tests diverged from the predicted ones. A more detailed analysis of this difference can be seen in Table 26.

Table 26 - Comparison between experimental and analytically determined results obtained in this work.

Elastic Modulus [GPa]	Experimental results	Predicted results	Difference (%)	Fiber reinforcement volume (%)
0R	0.15	0.23	51.10	0.00
2R	1.85	0.35	91.27	4.04
4R	3.56	6.76	89.95	8.08
5R	4.41	8.37	89.88	10.10

It can be seen that the difference between the predicted and experimentally determined results is similar throughout the fiber reinforced specimen types and circles 90%. This over-estimation of predicted elastic modulus when compared to experimentally determined elastic modulus existed even in the non-reinforced specimen configuration and the possible cause for it might be excessively high assumed mechanical properties of nylon filament in the first steps of the model (Table 9).

For the fiber reinforced specimen configurations, there are several causes for the great difference in the calculated and experimental elastic modulus:

- In-plane fiber waviness. The volume averaging method assumes that the Kevlar yarns are straight and no waviness in the yarns exists. In fact, neglecting fiber waviness by assuming straight fibers is a source of error in structural analysis. Most significantly, models based on straight fiber materials over predict axial properties [144].

- The lower experimental modulus could be due to the misalignment of the Kevlar yarns with respect to the longitudinal axis in the shoulder region. The misalignment of the fiber yarns results in a reduction in the elastic modulus of the test samples.

- Over-estimation of Kevlar volume. One assumption for the calculation of Kevlar region volume in the model is that the fiber yarns are in perfect contact with each other throughout the Z axis, i.e., there are no gaps (porosity) between them (which is not true). This is because the region was assumed to have a rectangular cross section, when in reality, the fibers have a circular shape as a result of the FDM process.

When thinking about possible reasons for this over-estimation, the most probable responsible (as can be noted when reading the listed causes above) is one that has its root in the fiber reinforcement region. As the fiber material possess much higher mechanical properties than the nylon filament, it has a more important impact in the overall prediction of the printed specimen’s elastic modulus.

As such, the starting point for reaching more accurate predictions was the reduction of the fiber width parameter, which was previously assumed as 0.7 mm (Table 13) and maintaining everything else constant. This will reduce the fiber volume and therefore the predicted elastic constants.

Doing a sensitive analysis in Excel (Figure 46), the fiber width that returned better predictions for all reinforced specimens was approximately 0.352 mm (exact value 0.3523 mm). The predicted values for the elastic modulus using this fiber width are listed in Table 27.

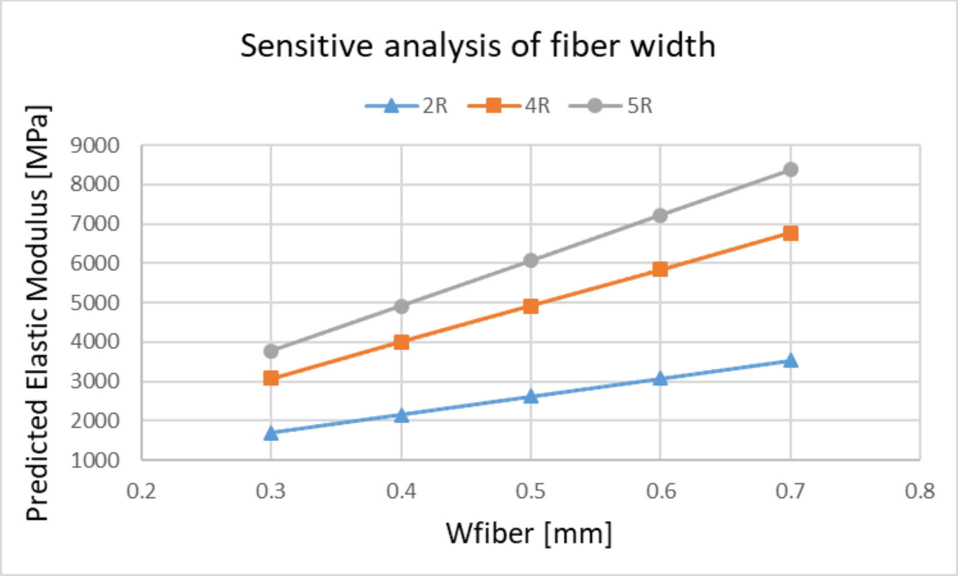

Figure 46 - Predicted elastic modulus values of each fiber reinforced specimen configuration (using the Volume Average Stiffness model) for different values of fiber width (in mm).

It can be seen that the predicted values of the elastic modulus increase linearly with increasing fiber width. This makes sense, as when the fiber width increases, the volume increases in a linearly manner, which makes the contribution of the fiber region greater to the overall mechanical properties of the specimen.

Table 27 - Predicted values using a fiber width of 0.352 mm and the difference (in percentage) between these values and the experimentally determined ones for each fiber reinforced specimen configuration. It can also be seen the calculated fiber volume fraction for each specimen configuration with this fiber width.

Specimen configuration	Predicted Elastic Modulus [MPa] $W_{fiber} = 0.352$ mm	Experimentally Determined Elastic Modulus [MPa]	Difference (%)	Calculated fiber volume fraction (%)
2R	1935	1850	4.61	2.03
4R	3557	3560	-0.09	4.06
5R	4367	4410	-0.96	5.08

Looking at these results, it can be concluded that for a fiber width of 0.352 mm, instead of 0.7 mm (with everything else fixed), the difference (in percentage) between the predicted and experimentally determined values of the elastic modulus, was reduced from approximately 90%, to 4.61 % (larger difference, obtained for the 2R specimen configuration).

The larger difference observed between the model and the experimental results for the 2 concentric ring samples could be explained by poor bonding between the fibers and the nylon matrix. Making the transfer of the load from the matrix to the fibers ineffective. This model assumes that fibers and matrix are perfectly bonded. Imperfect fiber-matrix bonds could result in fiber pull-out or slipping which would result in a lower elastic modulus than the predicted modulus.

It can be seen from Table 27 that the predicted results are more accurate with greater fiber volume fractions. This means that the Volume Average Stiffness model is more precise with increasing fiber volume fraction. This is consistent with the results obtained in [2]. Therefore, the methodology presented in this document should be used for modeling structures that have fiber volume fractions of 4% and above, with the upper limit of the interval of fiber volume fractions that can lead to valid predictions remaining unknown.

6 Concluding Remarks

6.1 Conclusions

In this study, four combinations of samples were produced using the Mark One Printer. Three types of Kevlar reinforced 3D-printed specimens and a nylon only type of specimen, for control purposes.

A volume averaging stiffness method was developed in order to predict the tensile properties (elastic modulus) of the fiber reinforced 3D printed samples. Additionally, experimental investigations were conducted to not only examine the effect of adding Kevlar fiber reinforcement into nylon, on the tensile properties of the composite specimen (Young's modulus and ultimate tensile strength), but also to compare the experimental results with the projections made using the analytical model (volume average stiffness model).

The results of this study show that greater fiber reinforcement results in an increase in stiffness and ultimate strength, therefore high volume fractions of fibers should be used for stiffness and strength critical applications.

With the determination of the elastic modulus from the experimental results and the weight of each 3D-printed fiber reinforced specimen, the specific properties (specific elastic modulus and specific tensile strength) were obtained and exhibited values that can compete with some materials in the "metals and alloys area" (Figure 45). These properties have the potential to be improved with the design of a geometry that allows the specimens to resist the high stress concentration generated that caused their premature failure in this study. Following some guidelines, a new specimen geometry was designed and proposed for this highly anisotropic materials in Section 5.1.

The volume averaging method described in Section 3.4 has been implemented so that designers can quickly predict the elastic modulus of fiber reinforced 3D printed components and use them for functional applications which require specific tensile properties.

In the first predictions, the model returned results that deviated from the experimental ones by approximately 90%. An alteration was made to the model that adjusts the overestimated Kevlar volume fraction inside the tensile tested cross section, making the model more realistic. The model assumes that the Kevlar region is rectangular, which is not true, since the deposited fibers of Kevlar have an oval shape and are not fully connected throughout the Z axis (inside the same layer). To account for this error, a sensitive analysis was carried to obtain the values of the predicted elastic modulus for different fiber width values. The best predictions for all printed specimens was calculated with a fiber width of 0.352 mm, with differences to experimental results of 4.61 %, -0.09 % and -0.96 % for the 2R, 4R and 5R specimens respectively.

The 4R specimen configuration (4.06 % fiber volume fraction) was the one that showed a better agreement between the predicted and experimentally determined results, with (approximately) a 0.1 % difference.

The 2 concentric ring configuration (2.03 % fiber volume fraction) was the worst prediction of the model, which shows that the model is better suited for higher fiber volume fractions.

The predictive model allows for the tensile properties of fiber reinforced 3D printed parts, in particular for sample configurations with greater fiber volume fractions, to be easily predicted.

6.2 Suggestions for future developments

The versatility of the Mark One Printer allows for countless possibilities of produced parts characteristics, through the variation of the printing parameters. Which makes it easy to test the flexibility of the model. For example, this study examined concentric fiber reinforcement but the Eiger 3D printing software also allows for full layers of fiber reinforcement as clarified in section 3.1. In fact, different fiber reinforcement patterns may be useful to improve the mechanical properties of fiber reinforced 3D printed parts and are worthy tests of the model validity.

The model predictions of the mechanical properties can also be stretched to other fiber reinforcement materials, specifically, Carbon Fiber and Glass Fiber, also compatible with the Mark One Printer.

Another suggestion of work, is the validation of the geometry developed in Section 5.1 with the realization of tensile tests, as a geometry for tensile testing of fiber reinforced 3D-printed specimens is yet to be developed. And to compare the experimental results with the respective predictions of the developed volume average stiffness model.

Additionally, supplementary research is required to fully characterize the mechanical behavior of these structures. Indeed, to fully characterize the mechanical behavior of these fiber reinforced 3D printed structures, it is not enough to experiment the samples with tensile tests. It is of great interest to conduct bending, compression and torsion tests.

To better understand the performance of the composite as a whole, it is also necessary to study the matrix-fiber interface. To do so, detailed studies that analyze the behavior and characteristics of the matrix material are required.

References

[1] J. F. Rodríguez, J. P. Thomas, and J. E. Renaud, “Mechanical behavior of acrylonitrile butadiene styrene fused deposition materials modeling,” *Rapid Prototyp. J.*, vol. 9, no. 4, pp. 219–230, 2003.

[2] G. W. Melenka, B. K. O. Cheung, J. S. Schofield, M. R. Dawson, and J. P. Carey, “Evaluation and prediction of the tensile properties of continuous fiber-reinforced 3D printed structures,” *Compos. Struct.*, 2016.

[3] K. Friedrich and A. A. Almajid, “Manufacturing aspects of advanced polymer composites for automotive applications,” *Appl. Compos. Mater.*, vol. 20, no. 2, pp. 107–128, 2013.

[4] K. Friedrich, “Carbon fiber reinforced thermoplastic composites for future automotive applications,” *AIP Conf. Proc.*, vol. 1736, pp. 1–5, 2016.

[5] K. Jayaraman, “Manufacturing sisal – polypropylene composites with minimum fibre degradation,” vol. 63, pp. 367–374, 2003.

[6] C. Soutis, “Fibre reinforced composites in aircraft construction,” *Prog. Aerosp. Sci.*, vol. 41, no. 2, pp. 143–151, 2005.

[7] K. Van Rijswijk and H. E. N. Bersee, “Reactive processing of textile fiber-reinforced thermoplastic composites – An overview,” vol. 38, pp. 666–681, 2007.

[8] B. Lauke and S. Y. Fu, “Strength anisotropy of misaligned short-fibre-reinforced polymers,” *Compos. Sci. Technol.*, vol. 59, no. 5, pp. 699–708, Apr. 1999.

[9] S.-Y. Fu, X. Hu, and C.-Y. Yue, “Effects of Fiber Length and Orientation Distributions on the Mechanical Properties of Short-Fiber-Reinforced Polymers,” *J. Soc. Mater. Sci. Japan*, vol. 48, no. 6Appendix, pp. 74–83, 1999.

[10] B. R.J. and R. J. Skarlupka, “An overview of long fiber reinforced thermoplastics.” Engineering Society, Southfield, MI (United States), 31-Dec-1997.

[11] P. T. Curtis, M. G. Bader, and J. E. Bailey, “The stiffness and strength of a polyamide thermoplastic reinforced with glass and carbon fibres,” *J. Mater. Sci.*, vol. 13, no. 2, pp. 377–390, 1978.

[12] N. Sato, T. Kurauchi, S. Sato, and O. Kamigaito, “Microfailure behaviour of randomly dispersed short fibre reinforced thermoplastic composites obtained by direct SEM observation,” *J. Mater. Sci.*, vol. 26, no. 14, pp. 3891–3898, 1991.

[13] S. Y. Fu, B. Lauke, E. Mäder, C. Y. Yue, and X. Hu, “Tensile properties of short-glass-fiber- and short-carbon-fiber-reinforced polypropylene composites,” *Compos. Part A Appl. Sci. Manuf.*, vol. 31, no. 10, pp. 1117–1125, 2000.

[14] A. Kelly, “AN INTRODUCTION TO COMPOSITE MATERIALS,” in *Concise Encyclopedia of Composite Materials*, Cambridge University Press, 1994, pp. xvii–xxix.

[15] K. Oksman, M. Skrifvars, and J. Selin, “Natural fibres as reinforcement in polylactic acid (PLA) composites,” vol. 63, pp. 1317–1324, 2003.

[16] O. Faruk, A. K. Bledzki, H.-P. Fink, and M. Sain, “Progress Report on Natural Fiber Reinforced Composites,” *Macromol. Mater. Eng.*, vol. 299, no. 1, pp. 9–26, 2014.

[17] M. Zampaloni *et al.*, “Kenaf natural fiber reinforced polypropylene composites: A discussion on manufacturing problems and solutions,” *Compos. Part A Appl. Sci. Manuf.*, vol. 38, no. 6, pp. 1569–1580, 2007.

[18] F. Rezaei, R. Yunus, N. A. Ibrahim, and E. S. Mahdi, “Development of Short-Carbon-

Fiber-Reinforced Polypropylene Composite for Car Bonnet," *Polym. Plast. Technol. Eng.*, vol. 47, no. 4, pp. 351–357, Mar. 2008.

[19] DOE, "Vehicle Technologies Office | Department of Energy." [Online]. Available: https://energy.gov/eere/vehicles/vehicle-technologies-office. [Accessed: 04-Jul-2017].

[20] J. A. Carpenter, "Challenges and opportunities for automotive composites," *SPE Automot. Compos. Conf. Expo.*, 2008.

[21] M. Musselman, "Automotive composites: a design and manufacturing guide," 2006.

[22] R. Eller, "Future potential and inter-materials competition in lightweight automotive composites," *Automot. Compos. Conf. Expo.*, 2004.

[23] P. Lubrina, S. Giclais, C. Stephan, M. Boeswald, Y. Govers, and N. Botargues, "AIRBUS A350 XWB GVT: State-of-the-Art Techniques to Perform a Faster and Better GVT Campaign," Springer, Cham, 2014, pp. 243–256.

[24] F. Ning, W. Cong, Y. Hu, and H. Wang, "Additive manufacturing of carbon fiber-reinforced plastic composites using fused deposition modeling: Effects of process parameters on tensile properties," *J. Compos. Mater.*, vol. 51, no. 4, pp. 451–462, 2017.

[25] M. Cheng, W. Chen, and T. Weerasooriya, "Mechanical Properties of Kevlar® KM2 Single Fiber," *J. Eng. Mater. Technol.*, vol. 127, no. 2, p. 197, 2005.

[26] K. Naito, Y. Tanaka, Y. Jm, and Y. Kagawa, "Tensile and Flexural Properties of Single Carbon Fibres."

[27] P. Wambua, J. Ivens, P. Wambua, J. Ivens, and I. Verpoest, "Natural fibres : Can they replace glass in fibre reinforced plastics ? Natural fibres : can they replace glass in fibre reinforced plastics ?," vol. 3538, no. December 2014, 2003.

[28] K. Balaji Thattaiparthasarathy, S. Pillay, H. Ning, and U. K. Vaidya, "Process simulation, design and manufacturing of a long fiber thermoplastic composite for mass transit application," *Compos. Part A Appl. Sci. Manuf.*, vol. 39, no. 9, pp. 1512–1521, 2008.

[29] Markforged, "Mechanical properties of continuous fibers."

[30] D. DeWayne Howell; Scott Fukumoto, "Compression Molding of Long Chopped Fiber Thermoplastic Composites." 2014.

[31] F. Perrin, M. N. Bureau, J. Denault, and J. I. Dickson, "Mode I interlaminar crack propagation in continuous glass fiber/polypropylene composites: Temperature and molding condition dependence," *Compos. Sci. Technol.*, vol. 63, no. 5, pp. 597–607, 2003.

[32] K. Fujihara, Z. M. Huang, S. Ramakrishna, and H. Hamada, "Influence of processing conditions on bending property of continuous carbon fiber reinforced PEEK composites," *Compos. Sci. Technol.*, vol. 64, no. 16, pp. 2525–2534, 2004.

[33] C. Yang, X. Tian, T. Liu, Y. Cao, and D. Li, "3D printing for continuous fiber reinforced thermoplastic composites: mechanism and performance," *Rapid Prototyp. J.*, vol. 23, no. 1, pp. 209–215, 2017.

[34] R. von Turkovich and L. Erwin, "Fiber fracture in reinforced thermoplastic processing," *Polym. Eng. Sci.*, vol. 23, no. 13, pp. 743–749, Sep. 1983.

[35] M. L. Shiao, S. V. Nair, P. D. Garrett, and R. E. Pollard, "Effect of glass-fibre reinforcement and annealing on microstructure and mechanical behaviour of nylon 6,6," *J. Mater. Sci.*, vol. 29, no. 7, pp. 1973–1981, 1994.

[36] P. A. Templeton, "Strength Predictions of Injection Molding Compounds," *J. Reinf. Plast. Compos.*, vol. 9, no. 3, pp. 210–225, May 1990.

[37] S.-Y. Fu and B. Lauke, "Fracture resistance of unfilled and calcite-particle-filled ABS composites reinforced by short glass fibers (SGF) under impact load," *Compos. Part A Appl. Sci. Manuf.*, vol. 29, no. 5–6, pp. 631–641, Jan. 1998.

[38] K. Friedrich, "Microstructural efficiency and fracture toughness of short fiber/thermoplastic matrix composites," *Compos. Sci. Technol.*, vol. 22, no. 1, pp. 43–74, Jan. 1985.

[39] C. Rudd, "Resin transfer molding and structural reaction injection molding.," *Mater. Park. OH ASM Int. 2001.*, pp. 492–500, 2001.

[40] K. van Rijswijk, J. J. E. Teuwen, H. E. N. Bersee, and A. Beukers, "Textile fiber-reinforced anionic polyamide-6 composites. Part I: The vacuum infusion process," *Compos. Part A Appl. Sci. Manuf.*, vol. 40, no. 1, pp. 1–10, Jan. 2009.

[41] Z. Quan *et al.*, "Additive manufacturing of multi- directional preforms for composites : opportunities and challenges," *Biochem. Pharmacol.*, vol. 18, no. 9, pp. 503–512, 2015.

[42] "Committee F42 on Additive Manufacturing Technologies." [Online]. Available: https://www.astm.org/COMMITTEE/F42.htm. [Accessed: 18-Jun-2017].

[43] "ASTM F2792 - 12a Standard Terminology for Additive Manufacturing Technologies (Withdrawn 2015)." [Online]. Available: https://www.astm.org/Standards/F2792.htm. [Accessed: 10-Jun-2017].

[44] I. Campbell, D. Bourell, and I. Gibson, "Additive manufacturing: rapid prototyping comes of age," *Rapid Prototyp. J.*, vol. 18, no. 4, pp. 255–258, 2012.

[45] W. Gao *et al.*, "The status, challenges, and future of additive manufacturing in engineering," *Comput. Des.*, vol. 69, pp. 65–89, 2015.

[46] J. J. Adams *et al.*, "Conformal Printing of Electrically Small Antennas on Three-Dimensional Surfaces," *Adv. Mater.*, vol. 23, no. 11, pp. 1335–1340, Mar. 2011.

[47] B. Y. Ahn *et al.*, "Omnidirectional Printing of Flexible, Stretchable, and Spanning Silver Microelectrodes," *Science (80-.).*, vol. 323, no. 5921, 2009.

[48] T. A. Campbell and O. S. Ivanova, "3D printing of multifunctional nanocomposites," *Nano Today*, vol. 8, no. 2, pp. 119–120, Apr. 2013.

[49] X. Zheng *et al.*, "Ultralight, ultrastiff mechanical metamaterials," *Science (80-.).*, vol. 344, no. 6190, 2014.

[50] T. A. Campbell, S. Tibbits, and B. Garrett, "The Programmable World," *Sci. Am.*, vol. 311, no. 5, pp. 60–65, Oct. 2014.

[51] V. Krishna Balla, L. B. Roberson, G. W. O'Connor, S. Trigwell, S. Bose, and A. Bandyopadhyay, "First demonstration on direct laser fabrication of lunar regolith parts," *Rapid Prototyp. J.*, vol. 18, no. 6, pp. 451–457, Sep. 2012.

[52] European Space Agency, "Building a lunar base with 3D printing." 2013.

[53] N. Jones, "Science in three dimensions: the print revolution.," *Nature*, vol. 487, no. 7405, pp. 22–3, Jul. 2012.

[54] C. Barnatt, "3D printing: the next industrial revolution," 2013.

[55] S. E. Moulton and G. G. Wallace, "3-dimensional (3D) fabricated polymer based drug delivery systems," *J. Control. Release*, vol. 193, pp. 27–34, Nov. 2014.

[56] M. S. Mannoor *et al.*, "3D Printed Bionic Ears," *Nano Lett.*, vol. 13, no. 6, pp. 2634–

2639, Jun. 2013.

[57] D. B. Kolesky, R. L. Truby, A. S. Gladman, T. A. Busbee, K. A. Homan, and J. A. Lewis, “3D Bioprinting of Vascularized, Heterogeneous Cell-Laden Tissue Constructs,” *Adv. Mater.*, vol. 26, no. 19, pp. 3124–3130, May 2014.

[58] A. Goyanes *et al.*, “3D Printing of Medicines: Engineering Novel Oral Devices with Unique Design and Drug Release Characteristics,” *Mol. Pharm.*, vol. 12, no. 11, pp. 4077–4084, Nov. 2015.

[59] L. Chen, Y. He, Y. Yang, S. Niu, and H. Ren, “The research status and development trend of additive manufacturing technology,” *Int. J. Adv. Manuf. Technol.*, vol. 89, no. 9–12, pp. 3651–3660, Apr. 2017.

[60] J. P. Kruth, “Material Incress Manufacturing by Rapid Prototyping Techniques,” *CIRP Ann. - Manuf. Technol.*, vol. 40, no. 2, pp. 603–614, 1991.

[61] C. B. Williams, F. Mistree, and D. W. Rosen, “A Functional Classification Framework for the Conceptual Design of Additive Manufacturing Technologies,” *J. Mech. Des.*, vol. 133, no. 12, p. 121002, Dec. 2011.

[62] T. Wohlers, “Caffery T. Wohlers Report 2015: Additive Manufacturing and 3D Printing State of the Industry: Annual Worldwide Progress Report. Fort Collins: Wholers,” 2015.

[63] J. Go, “High-Throughput Extrusion-Based Additive Manufacturing,” pp. 1–172, 2014.

[64] B. Mueller, “Additive Manufacturing Technologies – Rapid Prototyping to Direct Digital Manufacturing,” *Assem. Autom.*, vol. 32, no. 2, p. aa.2012.03332baa.010, Apr. 2012.

[65] C. K. Chua and K. F. Leong, *3D Printing and Additive Manufacturing*. WORLD SCIENTIFIC, 2014.

[66] H. L. Tekinalp *et al.*, “Highly oriented carbon fiber-polymer composites via additive manufacturing,” *Compos. Sci. Technol.*, vol. 105, pp. 144–150, 2014.

[67] L. J. Love *et al.*, “The importance of carbon fiber to polymer additive manufacturing,” *J. Mater. Res.*, vol. 29, no. 17, pp. 1893–1898, Sep. 2014.

[68] W. Zhong, F. Li, Z. Zhang, L. Song, and Z. Li, “Short fiber reinforced composites for fused deposition modeling,” *Mater. Sci. Eng. A301*, vol. 301, pp. 125–130, 2001.

[69] M. L. Shofner, K. Lozano, F. J. Rodríguez-Macías, and E. V. Barrera, “Nanofiber-reinforced polymers prepared by fused deposition modeling,” *J. Appl. Polym. Sci.*, vol. 89, no. 11, pp. 3081–3090, Sep. 2003.

[70] M. . Shofner, F. . Rodríguez-Macías, R. Vaidyanathan, and E. . Barrera, “Single wall nanotube and vapor grown carbon fiber reinforced polymers processed by extrusion freeform fabrication,” *Compos. Part A Appl. Sci. Manuf.*, vol. 34, no. 12, pp. 1207–1217, Dec. 2003.

[71] “3D Printing continuous carbon fiber composites?: CompositesWorld.” [Online]. Available: http://www.compositesworld.com/articles/3d-printing-continuous-carbon-fiber-composites. [Accessed: 13-Jun-2017].

[72] B. G. Compton and J. A. Lewis, “3D-Printing of Lightweight Cellular Composites,” *Adv. Mater.*, vol. 26, no. 34, pp. 5930–5935, Sep. 2014.

[73] D. Lin, C. Richard Liu, and G. J. Cheng, “Single-layer graphene oxide reinforced metal matrix composites by laser sintering: Microstructure and mechanical property enhancement,” *Acta Mater.*, vol. 80, pp. 183–193, Nov. 2014.

[74] R. D. Goodridge *et al.*, “Processing of a Polyamide-12/carbon nanofibre composite by laser sintering,” *Polym. Test.*, vol. 30, no. 1, pp. 94–100, Feb. 2011.

[75] L. R. Holmes and J. C. Riddick, “Research Summary of an Additive Manufacturing Technology for the Fabrication of 3D Composites with Tailored Internal Structure,” *JOM*, vol. 66, no. 2, pp. 270–274, Feb. 2014.

[76] S. Christ, M. Schnabel, E. Vorndran, J. Groll, and U. Gbureck, “Fiber reinforcement during 3D printing,” *Mater. Lett.*, vol. 139, pp. 165–168, 2015.

[77] E. Malone and H. Lipson, “Fab@Home: the personal desktop fabricator kit,” *Rapid Prototyp. J.*, vol. 13, no. 4, pp. 245–255, Aug. 2007.

[78] R. Jones *et al.*, “RepRap – the replicating rapid prototyper,” *Robotica*, vol. 29, no. 1, pp. 177–191, Jan. 2011.

[79] D. . Pham and R. . Gault, “A comparison of rapid prototyping technologies,” *Int. J. Mach. Tools Manuf.*, vol. 38, no. 10–11, pp. 1257–1287, 1998.

[80] S. Scott Crump, “US5121329 A - Apparatus and method for creating three-dimensional objects,” 1992.

[81] B. Pettis, A. K. France, and J. Shergill, *Getting started with MakerBot*. O’Reilly Media, 2013.

[82] R. Singh, S. Singh, I. P. Singh, F. Fabbrocino, and F. Fraternali, “Investigation for surface finish improvement of FDM parts by vapor smoothing process,” *Compos. Part B Eng.*, vol. 111, pp. 228–234, 2017.

[83] Q. Sun, G. M. Rizvi, C. T. Bellehumeur, and P. Gu, “Effect of processing conditions on the bonding quality of FDM polymer filaments,” *Rapid Prototyp. J.*, vol. 14, no. 2, pp. 72–80, 2008.

[84] I. Gibson, D. W. Ronen, and B. Stucker, *Additive Manufacturing Technologies - Rapid Prototyping to Direct Digital Manufacturing*. 2010.

[85] “Thin-wall tube liquifier,” 1998.

[86] D. Espalin *et al.*, “Rapid Prototyping Journal A review of melt extrusion additive manufacturing processes: I. Process design and modeling,” *Rapid Prototyp. J. Rapid Prototyp. J. Rapid Prototyp. J. Iss Rapid Prototyp. J.*, vol. 20, no. 3, pp. 192–204, 2014.

[87] M. Domingo-Espin, S. Borros, N. Agullo, A.-A. Garcia-Granada, and G. Reyes, “Influence of Building Parameters on the Dynamic Mechanical Properties of Polycarbonate Fused Deposition Modeling Parts,” *3D Print. Addit. Manuf.*, vol. 1, no. 2, pp. 70–77, Jun. 2014.

[88] R. Jerez-Mesa, G. Gomez-Gras, J. A. Travieso-Rodriguez, and V. Garcia-Plana, “A comparative study of the thermal behavior of three different 3D printer liquefiers,” *Mechatronics*, vol. 0, pp. 1–9, 2017.

[89] “Additive manufacturing method for printing three-dimensional parts with purge towers,” 2013.

[90] “Design Guidelines: Fused Deposition Modeling (FDM).” [Online]. Available: https://www.stratasysdirect.com/resources/fused-deposition-modeling/. [Accessed: 20-Jun-2017].

[91] “High temperature modeling apparatus,” 2000.

[92] S. Ahn, M. Montero, D. Odell, S. Roundy, and P. K. Wright, “Anisotropic material properties of fused deposition modeling ABS,” *Rapid Prototyp. J.*, vol. 8, no. 4, pp. 248–

257, 2002.

[93] B. Vayre, F. Vignat, and F. Villeneuve, “Designing for Additive Manufacturing,” *Procedia CIRP*, vol. 3, pp. 632–637, 2012.

[94] “Supports and 3D Printing – Markforged.” [Online]. Available: https://support.markforged.com/hc/en-us/articles/115000724710-Supports-and-3D-Printing#design. [Accessed: 06-Jun-2017].

[95] A. R. Torrado, P. David, and R. B. Wicker, “Fracture Surface Analysis of 3D-Printed Tensile Specimens of Novel ABS-Based Materials,” pp. 343–353, 2014.

[96] P. Dudek, “FDM 3D Printing Technology in Manufacturing Composite Elements,” *Arch. Metall. Mater.*, vol. 58, no. 4, pp. 10–13, 2013.

[97] Stratasys, “FDM Thermoplastics Material Overview - Stratasys,” 2014. [Online]. Available: http://www.stratasys.com/materials/fdm. [Accessed: 24-Jun-2017].

[98] M. Nikzad, S. H. Masood, and I. Sbarski, “Thermo-mechanical properties of a highly filled polymeric composites for Fused Deposition Modeling,” *Mater. Des.*, vol. 32, no. 6, pp. 3448–3456, 2011.

[99] F. Ning, W. Cong, J. Qiu, J. Wei, and S. Wang, “Additive manufacturing of carbon fiber reinforced thermoplastic composites using fused deposition modeling,” *Compos. Part B Eng.*, vol. 80, pp. 369–378, 2015.

[100] X. Tian, T. Liu, C. Yang, Q. Wang, and D. Li, “Interface and performance of 3D printed continuous carbon fiber reinforced PLA composites,” *Compos. Part A Appl. Sci. Manuf.*, vol. 88, pp. 198–205, 2016.

[101] B. N. Turner, S. A. Gold, B. N. Turner, and S. A. Gold, “A review of melt extrusion additive manufacturing processes : II . Materials , dimensional accuracy , and surface roughness,” 2015.

[102] D. Croccolo, M. De Agostinis, and G. Olmi, “Experimental characterization and analytical modelling of the mechanical behaviour of fused deposition processed parts made of ABS-M30,” *Comput. Mater. Sci.*, vol. 79, pp. 506–518, 2013.

[103] O. A. Mohamed, S. H. Masood, and J. L. Bhowmik, “Optimization of fused deposition modeling process parameters: a review of current research and future prospects,” *Adv. Manuf.*, vol. 3, no. 1, pp. 42–53, Mar. 2015.

[104] A. K. Sood, R. K. Ohdar, and S. S. Mahapatra, “Parametric appraisal of mechanical property of fused deposition modelling processed parts,” *Mater. Des.*, vol. 31, no. 1, pp. 287–295, 2010.

[105] M. K. Agarwala, V. R. Jamalabad, N. A. Langrana, A. Safari, P. J. Whalen, and S. C. Danforth, “Structural quality of parts processed by fused deposition,” *Rapid Prototyp. J.*, vol. 2, no. 4, pp. 4–19, Dec. 1996.

[106] S. Ahn, M. Montero, D. Odell, S. Roundy, and P. K. Wright, “Anisotropic material properties of fused deposition modeling ABS,” *Rapid Prototyp. J.*, vol. 8, no. 4, pp. 248–257, Oct. 2002.

[107] S. Güçeri and M. Bertoldi, “Liquefier dynamics in fused deposition,” 2004.

[108] M. Yardimci and T. Hattori, “Thermal analysis of fused deposition,” *solid Free. …*, 1997.

[109] H. S. Ramanath, C. K. Chua, K. F. Leong, and K. D. Shah, “Melt flow behaviour of poly-ε-caprolactone in fused deposition modelling,” *J. Mater. Sci. Mater. Med.*, vol. 19, no. 7, pp. 2541–2550, Jul. 2008.

[110] N. Mostafa, H. Syed, S. Igor, and G. Andrew, “A study of melt flow analysis of an ABS-Iron composite in fused deposition modelling process,” *Tsinghua Sci. Technol.*, 2009.

[111] L. Ji and T. Zhou, “Finite element simulation of temperature field in fused deposition modeling,” *Adv. Mater. Res.*, 2010.

[112] Y. Zhang and Y. Chou, “Three-dimensional finite element analysis simulations of the fused deposition modelling process,” *B J. Eng. Manuf.*, 2006.

[113] J. F. Rodríguez, J. P. Thomas, and J. E. Renaud, “Mechanical behavior of acrylonitrile butadiene styrene fused deposition materials modeling,” *Rapid Prototyp. J.*, vol. 9, no. 4, pp. 219–230, 2003.

[114] A. K. Sood, R. K. Ohdar, and S. S. Mahapatra, “Experimental investigation and empirical modelling of FDM process for compressive strength improvement,” *J. Adv. Res.*, vol. 3, no. 1, pp. 81–90, 2012.

[115] J. Cerneels, A. Voet, J. Ivens, and J.-P. Kruth, “Additive manufacturing of thermoplastic composites.” KU Leuven, pp. 1–7, 18-Sep-2013.

[116] Z. Weng, J. Wang, T. Senthil, and L. Wu, “Mechanical and thermal properties of ABS/montmorillonite nanocomposites for fused deposition modeling 3D printing,” *Mater. Des.*, vol. 102, pp. 276–283, 2016.

[117] R. W. Gray, D. G. Baird, and J. Helge Bøhn, “Effects of processing conditions on short TLCP fiber reinforced FDM parts,” *Rapid Prototyp. J.*, vol. 4, no. 1, pp. 14–25, Mar. 1998.

[118] H. L. Tekinalp *et al.*, “Highly oriented carbon fiber-polymer composites via additive manufacturing,” *Compos. Sci. Technol.*, vol. 105, no. 17, pp. 144–150, Dec. 2014.

[119] Y. Zhang, W. De Backer, R. Harik, and A. Bernard, “Build Orientation Determination for Multi-material Deposition Additive Manufacturing with Continuous Fibers,” *Procedia CIRP*, vol. 50, pp. 414–419, 2016.

[120] R. Matsuzaki *et al.*, “Three-dimensional printing of continuous-fiber composites by in-nozzle impregnation.,” *Sci. Rep.*, vol. 6, no. February, p. 23058, 2016.

[121] F. Van Der Klift, Y. Koga, A. Todoroki, M. Ueda, and Y. Hirano, “3D Printing of Continuous Carbon Fibre Reinforced Thermo-Plastic (CFRTP) Tensile Test Specimens,” *Open J. Compos. Mater.*, vol. 6, no. January, pp. 18–27, 2016.

[122] A. N. Dickson, J. N. Barry, K. A. McDonnell, and D. P. Dowling, “Fabrication of continuous carbon, glass and Kevlar fibre reinforced polymer composites using additive manufacturing,” *Addit. Manuf.*, vol. 16, pp. 146–152, 2017.

[123] “Aluminum 6061-T6 ASM Material Data Sheet.” [Online]. Available: http://asm.matweb.com/search/SpecificMaterial.asp?bassnum=ma6061t6. [Accessed: 30-Jun-2017].

[124] “Eiger.” [Online]. Available: https://www.eiger.io/signin. [Accessed: 30-Jun-2017].

[125] A. Kvalsvig, X. Yuan, J. Potgieter, and P. Cao, “3D printing of fibre reinforced honeycomb structured composite materials,” *M2VIP 2016 - Proc. 23rd Int. Conf. Mechatronics Mach. Vis. Pract.*, 2017.

[126] “ASTM D638 - 14 Standard Test Method for Tensile Properties of Plastics.” [Online]. Available: https://www.astm.org/Standards/D638.htm. [Accessed: 30-Jun-2017].

[127] G. W. Melenka, B. K. O. Cheung, J. S. Schofield, M. R. Dawson, and J. P. Carey, “Evaluation and prediction of the tensile properties of continuous fiber-reinforced 3D printed structures,” *Compos. Struct.*, vol. 153, pp. 866–875, 2016.

[128] "Overview of materials for Nylon 6, Extruded." [Online]. Available: http://www.matweb.com/search/DataSheet.aspx?MatGUID=726845c457b94b7cafe31d2e65739e1d&ckck=1. [Accessed: 09-Jul-2017].

[129] S. Kawabata, "Measurement of the Transverse Mechanical Properties of High-performance Fibres," *J. Text. Inst.*, vol. 81, no. 4, pp. 432–447, Jan. 1990.

[130] A. F. Kregers and Y. G. Melbardis, "Determination of the deformability of three-dimensionally reinforced composites by the stiffness averaging method," *Polym. Mech.*, vol. 14, no. 1, pp. 1–5, 1978.

[131] G. Karami and M. Garnich, "Micromechanical study of thermoelastic behavior of composites with periodic fiber waviness," *Compos. Part B Eng.*, vol. 36, no. 3, pp. 241–248, 2005.

[132] H. M. Hsiao and I. M. Daniel, "Effect of fiber waviness on stiffness and strength reduction of unidirectional composites under compressive loading," *Compos. Sci. Technol.*, vol. 56, no. 5, pp. 581–593, Jan. 1996.

[133] H.-J. Chun, J.-Y. Shin, and I. M. Daniel, "Effects of material and geometric nonlinearities on the tensile and compressive behavior of composite materials with fiber waviness," *Compos. Sci. Technol.*, vol. 61, no. 1, pp. 125–134, Jan. 2001.

[134] G. W. Melenka, J. S. Schofield, M. R. Dawson, and J. P. Carey, "Evaluation of dimensional accuracy and material properties of the MakerBot 3D desktop printer," *Rapid Prototyp. J.*, vol. 21, no. 5, pp. 618–627, 2015.

[135] "Tutorial: The compression and transfer molding processes." [Online]. Available: https://www.sinotech.com/resources/tutorials/compression-transfer-molding/. [Accessed: 15-Aug-2017].

[136] "Carabiner development - Composite carabiner: manufacturing methods." [Online]. Available: http://www.crabdev.co.uk/comp manufacturing.htm. [Accessed: 12-May-2017].

[137] "Supports in 3D Printing: A technology overview | 3D Hubs." [Online]. Available: https://www.3dhubs.com/knowledge-base/supports-3d-printing-technology-overview. [Accessed: 15-Aug-2017].

[138] "Double Drive Gear." [Online]. Available: http://www.impresora3dalia.com/blog/comparativa-entre-la-witbox-y-la-witbox-2/double-drive-gear/. [Accessed: 15-Aug-2017].

[139] "Amazon.com: MakerBot ABS Filament, 1.75 mm Diameter, 1 kg Spool, Orange: Industrial & Scientific." [Online]. Available: https://www.amazon.com/MakerBot-Filament-Diameter-Spool-Orange/dp/B00IUHLYFK/ref=pd_sim_328_5?_encoding=UTF8&pd_rd_i=B00IUHLYFK&pd_rd_r=P6NM52AX8GQ7YQY7W3JM&pd_rd_w=0q6fe&pd_rd_wg=JsO15&refRID=P6NM52AX8GQ7YQY7W3JM&th=1. [Accessed: 15-Aug-2017].

[140] J. Mireles *et al.*, "Development of a Fused Deposition Modeling System for Low Melting Temperature Metal Alloys," *J. Electron. Packag.*, vol. 135, no. 1, p. 11008, Feb. 2013.

[141] "3D Printer SmartNozzle :: Create the Future Design Contest." [Online]. Available: https://contest.techbriefs.com/2016/entries/machinery-automation-robotics/7080. [Accessed: 15-Aug-2017].

[142] "Why FDM parts made in Makerbot always tend to warp on the..." [Online]. Available: https://www.researchgate.net/post/Why_FDM_parts_made_in_Makerbot_always_tend_to_warp_on_the_bottom_left_corner_of_the_object_when_seen_from_the_top_view.

[Accessed: 15-Aug-2017].

[143] "Cusp height and staircase effect." [Online]. Available: https://www.researchgate.net/figure/274309852_fig1_Figure-1-Cusp-height-and-staircase-effect-After-finishing-the-slicing-process-the. [Accessed: 15-Aug-2017].

[144] "Pam - Multi-Material FDM 3D Printer Uses Pellets Instead Of Filaments - 3Printr.com." [Online]. Available: https://www.3printr.com/pam-multi-material-fdm-3d-printer-uses-pellets-instead-filaments-2040723/. [Accessed: 15-Aug-2017].

[145] "16 Type of 3D Printer Filament | Buyer's Guide and Review 2017." [Online]. Available: https://www.allthat3d.com/3d-printer-filament/. [Accessed: 15-Aug-2017].

[146] O. A. Mohamed, S. H. Masood, and J. L. Bhowmik, *Optimisation of Dynamic Mechanical Thermal Properties of PC–ABS Parts Manufactured by FDM Process Using IV Optimal Design*, no. December. Elsevier, 2016.

[147] "Specific stiffness - Specific strength." [Online]. Available: http://www-materials.eng.cam.ac.uk/mpsite/interactive_charts/spec-spec/basic.html. [Accessed: 21-Jul-2017].

APPENDIX 1: Dimensional control of the printed specimens

Not only to evaluate the consistency of the Mark One Printer, but also to determine the cross-sectional area of the test specimens, geometrical measurements of the test samples were performed. The geometric measurements of the test samples were compared with the nominal dimensions for the ASTM D638 Type I dogbone sample shown in Figure 1.1. The width of the narrow section (WN) and sample thickness (T) was compared for all samples. At least 3 measurements were made for WN and T of each specimen (Table 1.1). All the measured values were inside ASTM D648 tolerances: ± 0.5 mm for WN and ± 0.4 mm for T.

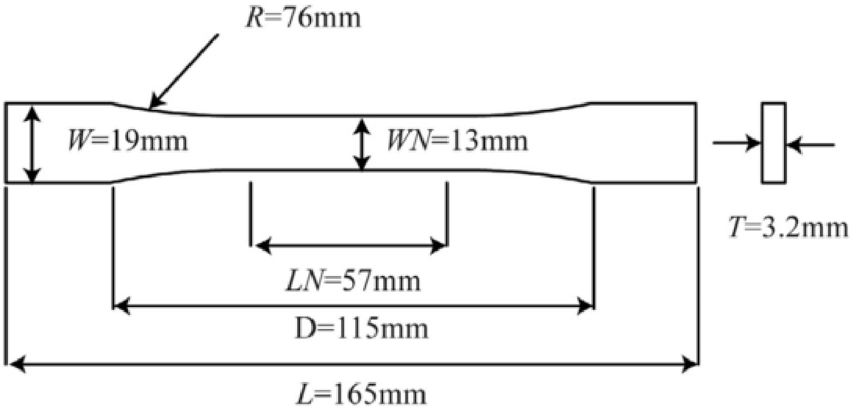

Figure 1.1 – Nominal dimensions of the printed test specimens, according to ASTM D638 Type I geometry. [2]

From Table 1.1 it can be seen that the sample measured dimensions slightly deviated from the nominal dimensions.

Table 1. 1 - Printed specimen's nominal and average measured dimension for the width of the narrow section and thickness.

5R Specimen	Nominal Dimension [mm]		Measured Dimension [mm]							
			WN				T			
	WN	T	WN 1	WN 2	WN3	Mean WN	T1	T2	T3	Mean T
1	13.00	3.20	13,08	13.03	13.02	13.04	3.09	3.11	3.13	3.11
2	13.00	3.20	13.00	13.03	13.04	13.02	3.05	3.11	3.09	3.08
3	13.00	3.20	13.01	13.04	13.00	13.02	3.07	3.12	3.12	3.10
4	13.00	3.20	12.99	13.01	13.05	13.02	3.08	3.11	3.07	3.09
5	13.00	3.20	12.93	12.92	13.02	12.96	3.07	3.12	3.06	3.08

4R Specimen	Nominal Dimension [mm]		Measured Dimension [mm]							
			WN				T			
	WN	T	WN 1	WN 2	WN3	Mean WN	T1	T2	T3	Mean T
1	13.00	3.20	13.06	12.96	12.97	13.00	3.09	3.11	3.09	3.10
2	13.00	3.20	13.03	12.99	12.97	13.00	3.14	3.13	3.07	3.11
3	13.00	3.20	12.95	13.06	13.02	13.01	3.06	3.13	3.08	3.09
4	13.00	3.20	12.99	13.02	12.94	12.98	3.07	3.09	3.05	3.07
5	13.00	3.20	13.00	13.06	13.04	13.03	3.09	3.13	3.05	3.09

2R Specimen	Nominal Dimension [mm]		Measured Dimension [mm]							
			WN				T			
	WN	T	WN 1	WN 2	WN3	Mean WN	T1	T2	T3	Mean T
1	13.00	3.20	13.07	13.06	13.12	13.08	3.11	3.13	3.10	3.11
2	13.00	3.20	13.06	13.14	13.11	13.10	3.06	3.12	3.11	3.10
3	13.00	3.20	13.02	12.96	13.00	12.99	3.08	3.06	3.09	3.08
4	13.00	3.20	12.98	13.00	13.06	13.01	3.10	3.09	3.08	3.09
5	13.00	3.20	12.99	13.03	13.04	13.02	3.08	3.08	3.04	3.07

0R Specimen	Nominal Dimension [mm]		Measured Dimension [mm]							
			WN				T			
	WN	T	WN 1	WN 2	WN3	Mean WN	T1	T2	T3	Mean T
1	13.00	3.20	13.00	13.07	13.08	13.05	3.14	3.18	3.19	3.17
2	13.00	3.20	13.21	13.14	13.10	13.15	3.14	3.19	3.15	3.16
3	13.00	3.20	13.27	13.23	13.15	13.22	3.15	3.14	3.14	3.14
4	13.00	3.20	13.13	13.21	13.17	13.17	3.13	3.14	3.12	3.13
5	13.00	3.20	13.13	13.06	13.07	13.09	3.13	3.16	3.13	3.14

A more detailed comparison between the nominal and measured sample dimensions can be found in Table 1.2.

Table 1. 2 - Comparison between nominal and average measured dimensions of WN and T for all specimen configurations. The values in the table are the mean values of the 5 specimens of each group. Standard deviation is in parenthesis.

Geometry - WN **Sample configuration**	**Nominal dimension [mm]**	**Measured dimension [mm]**	**% Difference**
0R – Average (Standard Deviation)	13.00	13.13 (0.066)	1.04
2R – Average (Standard Deviation)	13.00	13.04 (0.048)	0.33
4R – Average (Standard Deviation)	13.00	13.00 (0.019)	0.03
5R – Average (Standard Deviation)	13.00	13.01 (0.032)	0.09

Geometry - T **Sample configuration**	**Nominal dimension [mm]**	**Measured dimension [mm]**	**% Difference**
0R – Average (Standard Deviation)	3.20	3.15 (0.016)	-1.60
2R – Average (Standard Deviation)	3.20	3.09 (0.018)	-3.48
4R – Average (Standard Deviation)	3.20	3.09 (0.016)	-3.38
5R – Average (Standard Deviation)	3.20	3.09 (0.012)	-3.33

Examining the results shown in Table 1.1 and Table 1.2, it can be understood that dimensions of printed specimens typically show a discrepancy of ± 0.1 mm from the nominal dimensions. This quantity of variation existing in the 3D-printed specimens can also be perceived in [2] and [134].

An assessment to the dimensional accuracy of FDM printers is crucial. In fact, if known, the dimensional accuracy can permit suitable tolerances for functional parts made using this AM method. Therefore, a complete understanding of geometric accuracy can aid the designer in calculating error and even compensate for the inherent limitations of the 3D Printer.